Subsonic Icing Aerodynamics and Supersonic Ice Impact on a Hypersonic Forebody

---

A

Dissertation

Presented to

the faculty of the School of Engineering and Applied Science
University of Virginia

---

in partial fulfillment

of the requirements for the degree

Doctor of Philosophy

by

Spencer Stebbins

May 2023

APPROVAL SHEET

This

Dissertation

is submitted in partial fulfillment of the requirements
for the degree of

Doctor of Philosophy

Author: Spencer Stebbins

This Dissertation has been read and approved by the examining committee:

Advisor: Eric Loth

Advisor:

Committee Member: Haibo Dong

Committee Member: Christopher Goyne

Committee Member: Daniel Quinn

Committee Member: Haydn Wadley

Committee Member:

Committee Member:

Accepted for the School of Engineering and Applied Science:

Jennifer L. West, School of Engineering and Applied Science

May 2023

Abstract

Meteorological particles have been shown impact both subsonic and hypersonic vehicles negatively. It is necessary to continue to develop techniques and methods that will support the analysis of particles, such as ice, that can help mitigate issues and ensure the continued safe operation of air vehicles through hard environments. The first objective of this research is to conduct computational studies that compliment recent work completed at NASA to develop realistic ice shapes for the leading edge of a 65% scale Common Research Model (CRM65) wing. The computational studies leveraged experimental data completed on an 8.9% scaled CRM65 wing to assess the ability of RANS, DES, and IDDES numerical methods to predict the aerodynamic performance parameters and to better the complex three-dimensional flow physics. Initial work utilizing RANS highlighted its capability of capturing the wake downstream and showing that the resolution of the wake was not necessary to accurately capture the integrated aerodynamic coefficients. This allowed for simplification of the numerical domain for analysis for the swept-wing with and without a leading edge ice shape. Further work highlighted that at low angles of attack, lift, drag, and pitching moment are well predicted by RANS, DES, and IDDES. However, the numerical solutions produced by DES and IDDES for both lift and pitching moment did not fare as well at higher angles of attack where the coefficient became non-linear, e.g., near the pitching moment break in the experimental data. In particular, DES and IDDES did not quantitatively capture the spanwise component of the flow over the stalled portions of the swept wing nor did they properly predict the pressure distribution along the upper surface of the wing. In contrast, a conventional RANS approach surprisingly proved superior for predicting this fluid dynamic behavior. As such, the highly complex flow over a swept iced wing at stall conditions requires further development of the DES and IDDES approaches. In particular, it is suggested that the transition between RANS and LES regions for flow separations that have high spanwise velocity components be investigated in terms of turbulent mixing in order to allow improved transition models to properly capture the three-dimensional aerodynamic behavior.

The second objective of this research is to analyze the effect on hypersonic vehicles ice particles may have with regards to impact physics and erosion. Ice particles generally represent the largest particle in the atmosphere, especially at 10 km, which represents a key portion of the flight trajectory. These particles can cause damage and erosion to various components on the vehicle including the surface material and optical radomes. A set of simulations was conducted to support understanding the physics of atmospheric ice particles impacting the forebody of a hypersonic vehicle. These simulations analyzed ice particles as a function of both shape and size. At the flight condition analyzed, results show that nearly all of the incoming particles sized from 75 to 4,000 μm will impact the forebody and experience very little change in velocity. The change in temperature of the particles prior to impact is not sufficient enough to exceed the freezing point and thus a phase change for the particles is not expected. Due to the relatively large mass percentage of clouds containing ice particles sized around 2,000 μm, this bin of particles, especially for column ice, was predicted to contribute the most to the damage and erosion of the vehicle.

Acknowledgements

First, I would like to thank Dr. Eric Loth, Dr. Andy Broeren, Dr. Mark Potapczuk, and Chris Porter for their leadership, guidance, and patience while working with me through my graduate studies. They have all taught me a great number of things regarding the aerospace engineering field, whether it pertained to technical or non-technical skills. Secondly, I would also like to thank my family, friends, and cat who have supported me throughout my time here at University of Virginia. Finally, I would like to acknowledge support by the National Aeronautics and Space Administration under Grant Number NNX16AT17H issued through the NASA Education Minority University Research Education Project (MUREP) through the NASA Harriett G. Jenkins Graduate Fellowship activity. Any opinions, findings, and conclusions or recommendations expressed in this article are those of the author and do not necessarily reflect the views of the National Aeronautics and Space Administration.

Table of Contents

Nomenclature

A_{impact}	=	area of incoming particle cloud that will impact the nose cone
$A_{nose\ cone}$	=	frontal area of the nose cone
A_{surf}*	=	normalized surface area
C_L	=	coefficient of lift
C_D	=	coefficient of drag
C_D*	=	normalized drag coefficient
C_M	=	moment coefficient
C_P	=	pressure coefficient
C_{shape}	=	drag correction for shapes
c	=	chord
D	=	drag force
D_ω	=	cross-diffusion for ω
d_p	=	diameter of particle
E	=	aspect ratio
E_m	=	mass erosion per unit time
F_D	=	drag force
F_x	=	additional forces acting on particle
f	=	Stokes correction factor
G_k	=	generation of k
G_ω	=	generation of ω
g_x	=	gravitational acceleration
H	=	microhardness of target
K_c	=	fracture toughness of target
k	=	turbulence kinetic energy
L	=	lift force
$m\%$	=	mass percentage of cloud
$m_{plate}\%$	=	mass percentage of cloud for plate ice
$m_{column}\%$	=	mass percentage of cloud for column ice
P_0	=	pressure upstream of shock
P_1	=	pressure downstream of shock
$P_{t\infty}$	=	freestream stagnation pressure
P_t	=	stagnation pressure
q	=	mass of incoming particles per unit time for a given bin size and shape
Re_v	=	vehicle Reynolds number
Re_p	=	relative particle Reynolds number
$Re_{p,0}$	=	initial particle Reynolds number
r_{impact}	=	largest upstream radial location of particles that will impact the nose cone
$r_{nose\ cone}$	=	radius of the nose cone
S	=	symmetric component of the velocity tensor

SP	=	complete downstream survey plane
St	=	Stokes number
T_p	=	temperature of particle
U_∞	=	freestream velocity magnitude
u	=	component of velocity in the x-direction
V	=	fluid mean velocity
v	=	component of velocity in the y-direction
v_p	=	velocity of particle
v_f	=	velocity of fluid
W	=	swept-wing wake at survey location
w	=	component of velocity in the z-direction
w_{rel}	=	relative velocity of particle to fluid
x	=	streamwise coordinate
y	=	radial coordinate
Y_k	=	dissipation of k
Y_ω	=	dissipation of ω
α	=	angle of attack
β	=	incident angle of particle impact trajectory relative to surface
Γ	=	non-dimensional erosion of material (mass eroded per mass impacted)
ε	=	rate of turbulence dissipation
η	=	impact fraction
Λ	=	velocity gradient tensor
μ	=	dynamic viscosity
μ_f	=	dynamic viscosity of fluid
μ_t	=	turbulent viscosity
ζ	=	streamwise vorticity
ρ	=	density
ρ_c	=	density of coating
ρ_p	=	density of particle
τ_p	=	aerodynamic response time of particle
Ω	=	anti-symmetric component of the velocity tensor
ω	=	specific rate of turbulence dissipation

Chapter 1

Introduction

Atmospheric ice particles have a long and rich history with its impact on aircraft aerodynamics for subsonic. The influence of ice accretion on subsonic aircraft was initially researched by investigators in the 1920's and later became more important as a significant amount of icing incidents/crashes occurred during Word War II for military aircraft. NASA developed the Lewis Icing Research Tunnel (IRT) to help understand how icing could cause detrimental effects to lifting surfaces. Researchers sought to largely understand two topics: how the ice accretions could impact the aerodynamic performance parameters and how to mitigate the accumulation of ice on key aircraft components (e.g., lifting surfaces). The Space Race unfortunately stalled icing research until an International Workshop in Aircraft held by NASA helped rejuvenate the effort. This event pushed forward studies that focused on analyzing icing via experimental efforts (e.g., wind tunnel and flight tests) and numerical simulations.

However, after the crash of American Eagle Flight 4184 in 1994, it was clear to the organizations that there were still gaps in knowledge on how dangerous icing was to subsonic aircraft. Modern aircraft employ lifting surfaces that were significantly more different that the simple airfoil geometries researched thus far. Listing surfaces now contained more complex profiles with features such as sweep angle and twists that could resulted in more dynamic flow over the wings. Further studies were conducted in order to understand the three-dimensional nature of the flow pre- and post- ice accumulation. Past reviews on experimental and computational studies have shown that flow over a wing has a spanwise component that can't be captured by only a two-dimensional airfoil. The computational portion of these studies looked to utilize both steady state and transient solutions to understand the fluid dynamics over a wing with a leading edge ice accretion. The continued advancement of computational models has allowed for increased accuracy and robustness to resolve more complex geometries of aerodynamic surfaces and ice shapes.

Beyond subsonic vehicles, ice particles can also have an impact on hypersonic vehicles. For both reusable and non-reusable vehicles, their trajectories coincide with altitudes where there are extensive amounts of meteorological particles present. These particles at large flight speeds can cause erosion damage to surface materials including those covering key components like optical radomes. This damage can subsequently affect both controllability and survivability of hypersonic vehicles as they travel through both the initial and final stages of their trajectories. Recent studies have focused on identifying the type of particles that can exist at relevant altitudes as well as understanding the extent of damage various particles can have on certain surface materials.

The first objective of this study is to support filling in the gaps in knowledge regarding the impact of icing on three-dimensional aerodynamics for commercial aircraft. This research will leverage experimental data collected on an iced 8.9% scaled Common Research Model (CRM65) at the Wichita State University's Walter H. Beech Wind Tunnel. The research will first focus on laying the ground work for more in-depth studies by investigating and assessing the ability of a Reynolds-Averaged Navier Stokes (RANS) turbulence model to capture both the fluid flow around a swept wing as well as the wake downstream of the wing. The second focus will compare the ability of a steady state simulations utilizing RANS against the ability of transient simulations utilizing Hybrid RANS-LES models to predict high Reynolds number aerodynamic flows and capture the aerodynamic impact of ice accretion on the leading edge of the aforementioned wing design. This portion of the research is part of an initiative to understand iced wing aerodynamics by a consortium of organizations including NASA, the Federal Aviation Administration (FAA), the Office National d'Etudes et Recherches Aérospatiales (ONERA), Boeing, the University of Illinois, the University of Virginia, and the University of Washington. To the author's knowledge this is the first set of studies to analyze the fidelity and robustness of both RANS and Hybrid RANS-LES models in comparison to experimental data for a swept wing with and without a leading edge ice shape where substantial spanwise flow separation is expected to occur.

The second objective of this study is to understand how icing particles can affect hypersonic vehicle forebodies. There has only been a selected number of studies that look at the impact of ice particles on hypersonic vehicles and this study seeks to supplement the information currently available. This effort will look at understanding the trajectories, changed in characteristic particle properties, and subsequent impacts and erosion of surface materials for a range of ice particles shapes and diameters. To predict the particle trajectory, a particle drag model will be used to the determine the influence of the ice particles' geometrical characteristics on the equation of motion. For each particle injected into the fluid domain, both velocity and temperature will be tracked to analyze and determine the potential damage to a vehicle's forebody as well as any phase change of the ice particle prior to impact. To the author's knowledge, this is the first publicly known study to utilize computational methods to consider and track atmospheric ice particles based on shape and mass distribution, analyze their impact on a hypersonic vehicle at a specified point in the flight trajectory, and determine mass erosion per unit time based on empirical formulas derived from particle impacts on specific materials.

Chapter 2

Computational Analysis of the Wake Structure of a Swept-Wing

1 – Introduction

The advancement in Computational Fluid Dynamics (CFD) has enabled a wide variety of industries to leverage various numerical methods to not only complement and supplement costly experimental tests with more time and cost-efficient computational analysis, but also conduct analysis a lot earlier in the product development cycle. From a research perspective, CFD has allowed the community to examine both steady state and time dependent based information regarding fluid dynamics through the implementation of numerical methods including Reynolds Averaged Navier Stokes (RANS), Large Eddy Simulation (LES), Hybrid RANS-LES, and Direct Numerical Simulation (DNS). One area that has benefited from this advancement is the research field focused on understanding of the impact of icing on modern aircraft.

Recent work completed by a group of organizations consisting of NASA, ONERA, FAA, Boeing University of Washington, University of Illinois, Wichita State University, and University of Virginia, sought to bridge some of the gaps in knowledge present in the research community for icing effects on swept wings that were representative of wings on commercial airliners. As part of the aforementioned effort, Lum *et al.* focused on developing a method to accurately capture the wake of the swept-wing during wind tunnel tests [1]. As seen in Fig. 2.1, the model tested was an 8.9% scale version of the semi-span swept CRM65 wing developed by Vassberg *et al.* [2]. The wake survey method developed consists of utilizing a three five-hole probe system placed 21.8" downstream from the trailing edge of the wing tip (Fig. 2.2). This system is then incrementally swept across the cross section of the wind tunnel to collect time-averaged pressure data. As presented by Lum *et al.*, the resulting data can then be used to both qualitatively understand downstream flow field structures and quantitatively analyze drag and lift by performing a control volume analysis around the wing and making several assumptions [1,3–6]. The wake integrals defining these quantities are below:

$$D = \iint_W (P_{t\infty} - P_t)dydz + \frac{\rho}{2}\iint_{SP}(U_\infty^2 - u^2 + v^2 + w^2)dydz \tag{2.1}$$

$$L = \rho U_\infty \iint_W y\zeta dydz \tag{2.2}$$

(a) (b)

Fig. 2.1 a) Photograph the 8.9% scaled CRM65 installed in WSU Wind Tunnel and b) view of the wake survey system installed in the tunnel behind the model [1]

The work presented herein does not focus on analyzing the impact of ice shapes on the flow-field around a swept-wing, but instead on laying the groundwork in understanding the ability of RANS to predict a relatively complex flow-field when compared to the time-averaged pressure data from a wake survey. This information is necessary to support properly defining the numerical domain of a swept-wing with or without ice shapes in a wind tunnel. As such, the two key objectives for this paper are to:

1) Evaluate and determine the ability of RANS k-ω SST to capture the wake downstream of a swept-wing

2) Understand how the refinement of the wake effects the aerodynamics coefficients

The goal of these objectives is to ultimately understand to what degree capturing the wake of a model in subsonic flow does or does not propagate upstream and influences the pressure distribution along the surface of the model, and thus the integrated aerodynamic coefficients. While work has been done by Skinner *et al.* to understand the wingtip vortex structure downstream of a swept-wing, to the authors' knowledge, this is the first study to both compare the downstream wake of a swept-wing captured experimentally against a wake produced with numerical methods while simultaneously examining the impact of the downstream wake's numerical resolution on the integrated aerodynamic coefficients [7].

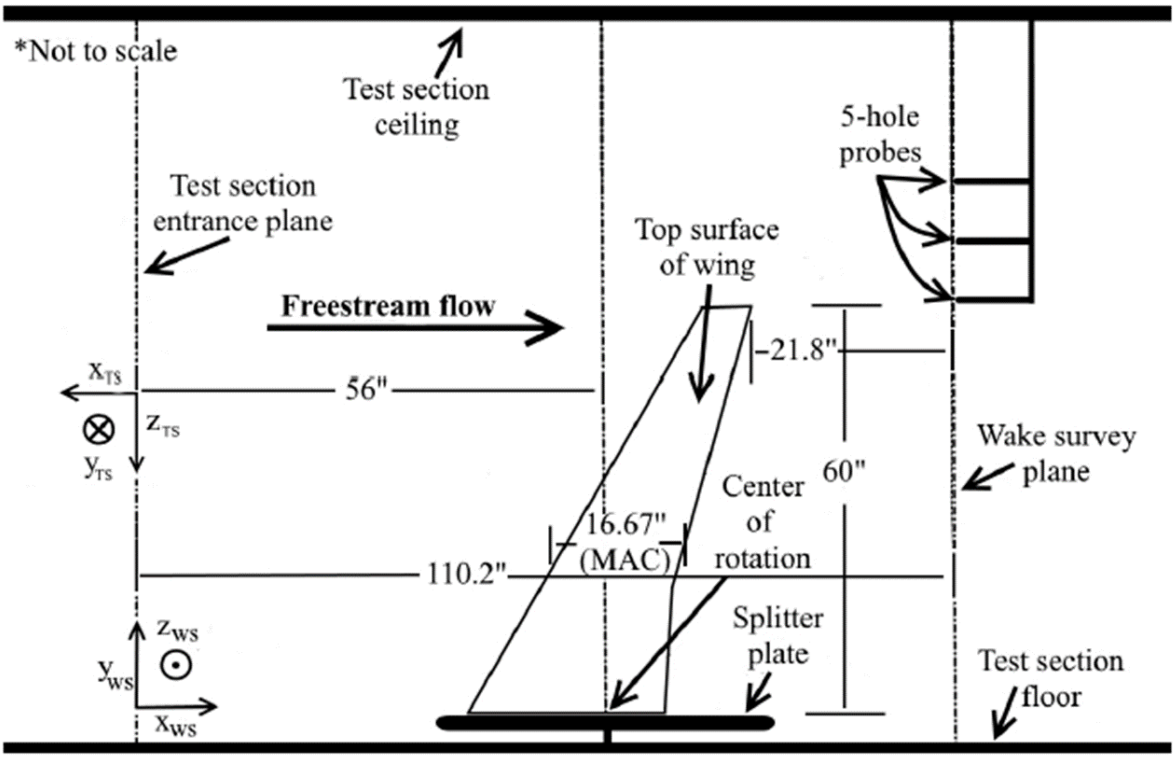

Fig. 2.2 Diagram of the model installed in the WSU Wind Tunnel with relevant dimensions of the systems. The coordinate system used to take the wake survey data is denoted by TS. WS denotes the coordinate system used to carry out the integrals to find lift, induced drag, and profile drag. [1]

2 – Computational Domain and Methodology

2.1 – Problem Description

As noted in the introduction, the work presented herein is based on the configuration studied by Diebold *et al.* and Lum *et al.* in Wichita State University's Walter H. Beech Wind Tunnel [1,8]. The key features of this configuration are a span of 1.524 m, a MAC of 0.4234 m, a taper ratio of 0.23, and a leading-edge sweep angle of 37.2 deg. Other features of this wing were outline in Broeren *et al.*'s paper [9]. The studies discussed in this paper focused on examining the configuration at an angle of attack of 6 deg., a Mach number of 0.18, and a Reynold's number of $1.6 \cdot 10^6$.

Figure 2.3 showcases a sectional cut through the computational domain with respect to the X-Y plane. While the computational domain was developed to represent the experimental tests conducted in the wind tunnel, a couple of simplifications were made in the model. First, the corner chamfers of the wind tunnel that can be seen in Fig. 1, were excluded. Secondly, these simulations did not include the streamline stroud present between the floor of the wind tunnel and the splitter plate at the base of the swept-wing. Finally, the inlet and outlet were placed 10 chords upstream and 30 chords downstream of the model respectively, where a chord is equal to the wing's MAC. These inlet and outlet locations were selected in order to ensure proper flow development upstream of the model and to avoid numerical back pressure from communicating upstream and affecting the results. The final 3D computational domain measured 2.134 m by 3.048 m by 19.68 m.

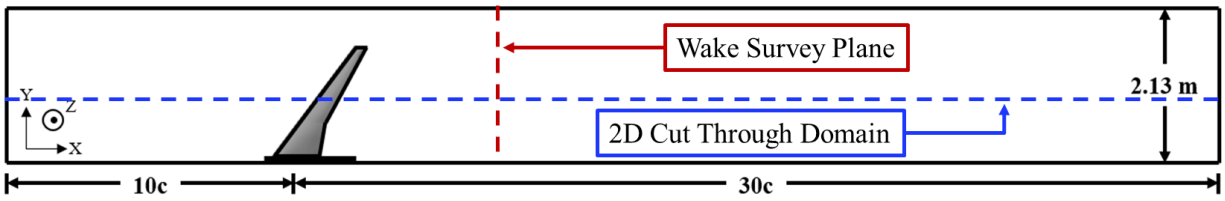

Fig. 2.3 Schematic of the computational domain used, where "c" is the mean aerodynamic chord (MAC = 0.423 m)

During the initial simulations of the system, it was seen that the employed meshing techniques were inadequate in capturing the wake. To resolve this issue and to support the development of a refinement region downstream of the wing, 2D computational studies were conducted. As seen in Fig. 2.3, this cut was taken along the streamwise direction of the computational domain with respect to the X-Z plane. The cut was taken at a location that coincided with a spanwise location of y/b = 0.6, where b = 1.524 m. Further information regarding the 2D mesh study defining the wake refinement will be discussed in the "Meshing Techniques" section.

2.2 – Numerical Methodologies

This study leveraged the Reynolds Averaged Navier Stokes (RANS) numerical method to resolve the problem at hand. RANS is a time averaging of the unsteady Navier Stokes equations that result in a Reynolds stress term that has to be modeled in order to close the equations. While there are a variety of turbulence models available (i.e., Spalart-Allmaras, Baldwin-Lomax, k-ε, and etc.), recent works have shown k-ω SST to be sufficient in resolving complex flow-fields. This turbulence model was initially developed as a way to address the short-comings of both the k-ε and k-ω models [10]. While the former was shown to predict free-shear regions accurately, the latter was better at resolving near wall interactions, and more specifically, providing more numerical stability and resolution in the logarithmic region of the boundary layer. To combine the benefits of both models, Menter proposed the k-ω SST model which utilized a blending function that made sure that the k-ω model was used in near-wall regions and switched to k-ε in the free-shear regions [11]. In this model, k and ω are solved in two transport equations:

$$\frac{\partial(\rho k)}{\partial t} + \frac{\partial(\rho k V_i)}{\partial x_i} = \frac{\partial}{\partial x_j}\left[(\mu + \sigma_k \mu_t)\frac{\partial k}{\partial x_j}\right] + G_k - Y_k \tag{2.3}$$

$$\frac{\partial(\rho \omega)}{\partial t} + \frac{\partial(\rho \omega V)}{\partial x_i} = \frac{\partial}{\partial x_j}\left[(\mu + \sigma_\omega \mu_t)\frac{\partial \omega}{\partial x_j}\right] + G_\omega - Y_\omega + D_\omega \tag{2.4}$$

2.3 – Meshing Technique

All mesh generation for this research was conducted using a commercially available software called Pointwise. To ensure a proper $y+$ value equal to 1 for the grid, an initial grid height, Δs, of 6.452 μm was imposed on the first cells grown from the surface of the model. Using Pointwise's anisotropic tetrahedral extrusion method (T-Rex), the cells were grown from the surface at a growth rate of 1.15, with maximum number of layers set to 50, and a boundary decay of 0.95. A

similar set of parameters were defined for growing the cells away from the walls of the simulated wind tunnel.

While the meshing technique employed was sufficient in satisfying the requirements to properly implement RANS k-ω SST and resolve the boundary layer near the model, the technique did not provide enough refinement for the mesh in the far field to fully resolve the wake of the wing. As will be discussed later, the flow-field predicted by the initial simulations contained a wake that becomes greatly diffused and mixes with the free-stream flow once the computational cells grew too large to maintain the small features defining the flow. To understand what level of mesh refinement is needed to maintain the wake's flow physics, a set of 2D simulations were ran with varying cell sizes. As noted previously, the 2D simulation flow domain was defined in the X-Z plane. The various meshes were generated using two criteria: 1) a constant cell width (z-direction) and 2) a constant ratio of 4 of the length of the cells (x-direction) closest to the airfoil, to the length of the cells furthest from the airfoil in the wake survey region. Table 2.1 outlines the different 2D meshes (herein referred to as Meshes 1-5) studied with their respective cell size spacing, cells in the wake refinement region, and total number of cells in the flow-field domain. As shown in the table, the series of meshes selected were such that each subsequent mesh was refined by nearly a factor of 2. As will be discussed later, the results of this meshing study were then applied to meshing the 3D study to properly capture the wake.

Table 2.1 Mesh Characteristics of 2D Wake Refinement Study

Mesh #	Wake Refinement	Spacing (in.) from Wind Trailing Edge to Wake Survey Region	Cells in Wake Refinement Region	Total Cells
1	No	-	0	92,430
2	Yes	0.1 to 0.4	7,840	108,990
3	Yes	0.05 to 0.2	15,680	118,566
4	Yes	0.025 to 0.1	31,360	138,172
5	Yes	0.0125 to 0.05	62,720	177,220

3 – Results

3.1 – 2D Flow-Field Analysis

For the 2D mesh refinement study, a qualitative analysis of the flow-field was completed by using contours of the total pressure coefficient (ratio of the total pressure to freestream dynamic pressure) and taking a cut through the flow domain at the wake survey location (denoted by the dashed white line in Fig. 2.4) from Lum *et al.*'s work [1]. Figure 2.4 highlights the comparison of Mesh 1, 3, and 5. Mesh 1 utilizes Pointwise's T-Rex method without any wake refinement. Figure 2.4a shows that due to lack of resolution in this area, the wake downstream of the airfoil becomes highly diffused and mixes with the freestream prior to the wake survey location. In contrast to Mesh 1, Mesh 3 shown in Fig. 2.4b, contains mesh refinement in the wake region that captures

more details of the downstream wake. In particular, the structure of the wake, as defined by relatively low total pressure, becomes more defined with less numerical diffusion. The wake is not viewable in Fig. 2.4c due to the high density of the superposed cell resolution for Mesh 5, which has approximately 4 times more cells defining the wake region than Mesh 3.

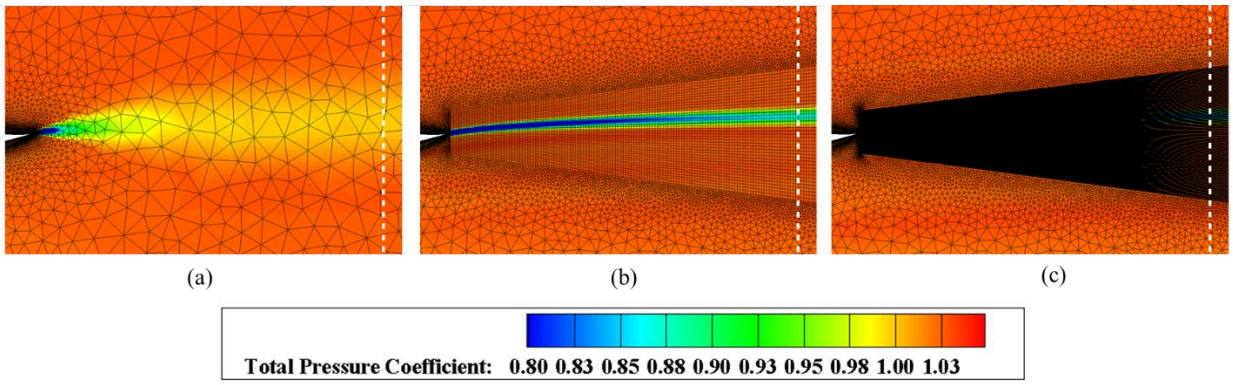

Fig. 2.4 Contour of Total Pressure Coefficient with mesh overlay for a) unrefined wake, b) Mesh 3 wake refinement, and c) Mesh 5 wake refinement.

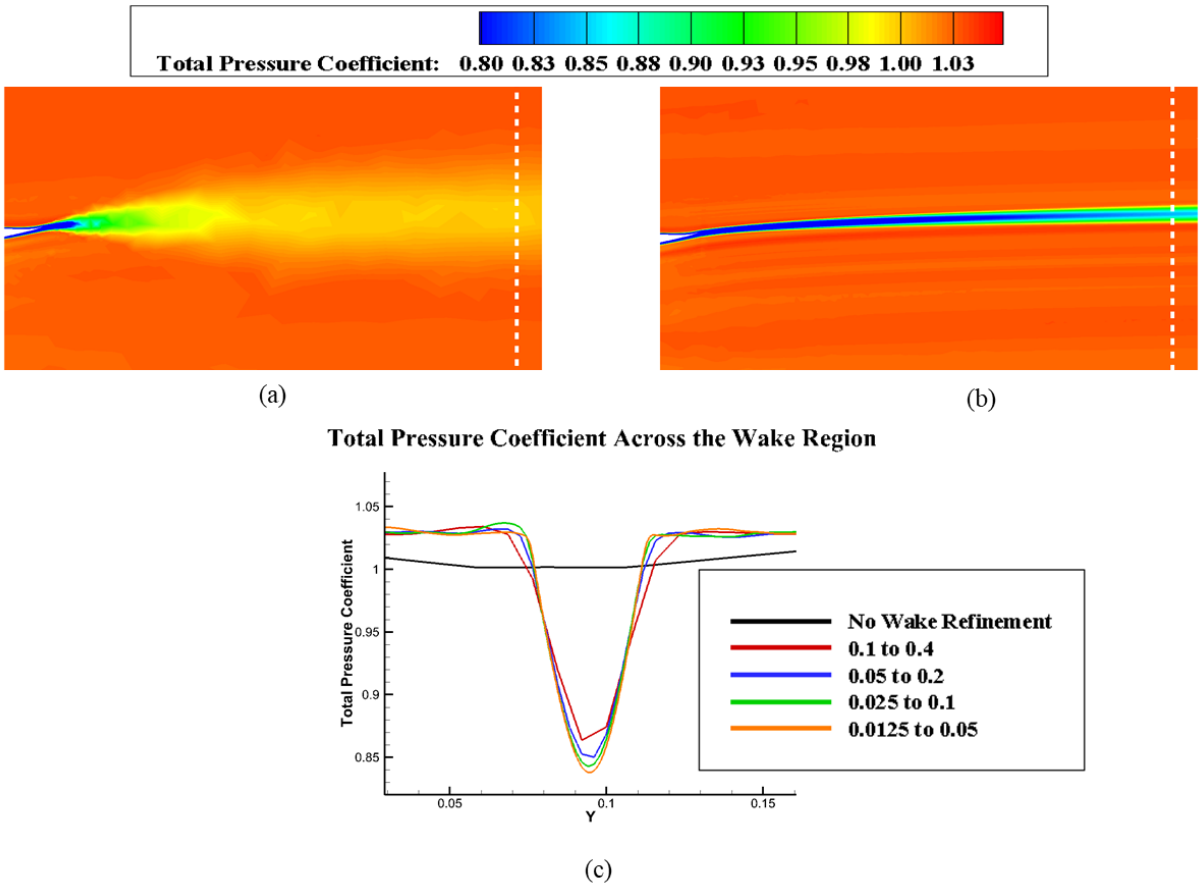

Fig. 2.5 Contour of the total pressure coefficient for a) unrefined wake and b) refined wake aft of 2D airfoil with c) evaluated at the downstream location indicated by the dashed white line for various wake refinements.

Figure 2.5a and b are contour maps of the wake structure downstream of the airfoil without the mesh overlaying the domain. The pressure losses observed in the wake region are associated with the drag of the airfoil/wing [1], and Fig 2.5c provides a relative comparison between the various meshes at the wake survey plane. Again, without the mesh refinement, the pressure losses are highly diffused while the inclusion of the wake refinement shows a sharp and significant dip in the total pressure coefficient. This behavior is independent of the level of refinement used in Mesh 2-5. Based on these results, a cell size spacing of 0.25 inches in the streamwise direction for the 3D simulation was deemed to be sufficient for grid-independent predictions of the wake flow, while also not adding too many cells to the flow domain.

3.2 – 3D Flow-Field Analysis

Based on the 2D mesh refinement trade study results, a new mesh was developed for the 3D simulation accordingly. The size of the mesh without wake refinement was $29.5 \cdot 10^6$ cells, while the mesh with wake refinement was $51.0 \cdot 10^6$ cells. A comparison of the total pressure coefficient for the swept-wing wake captured experimentally and calculated numerically can be seen in Fig. 2.6. Figure 2.6a for the experimental results shows that there are three major features defining the wake: 1) a well-defined wing-tip vortex at the top of the image, 2) a bend in the wake profile representative of the location of the wing's Yehudi break, and 3) the interaction of the wing's wake with the wake of the splitter plate. Similar to the 2D study, Fig. 2.6b shows that the wake in the unrefined simulation is highly diffused and only slightly captures the aforementioned features. In contrast, Fig. 2.6c highlights the ability of the numerical method to capture the swept-wing's wake and wake features when mesh refinement is used and shows high fidelity relative to the experimental results. Figure 7 provides a zoomed in view of the mesh for the unrefined and refined meshes in the region of the wing-tip vortex.

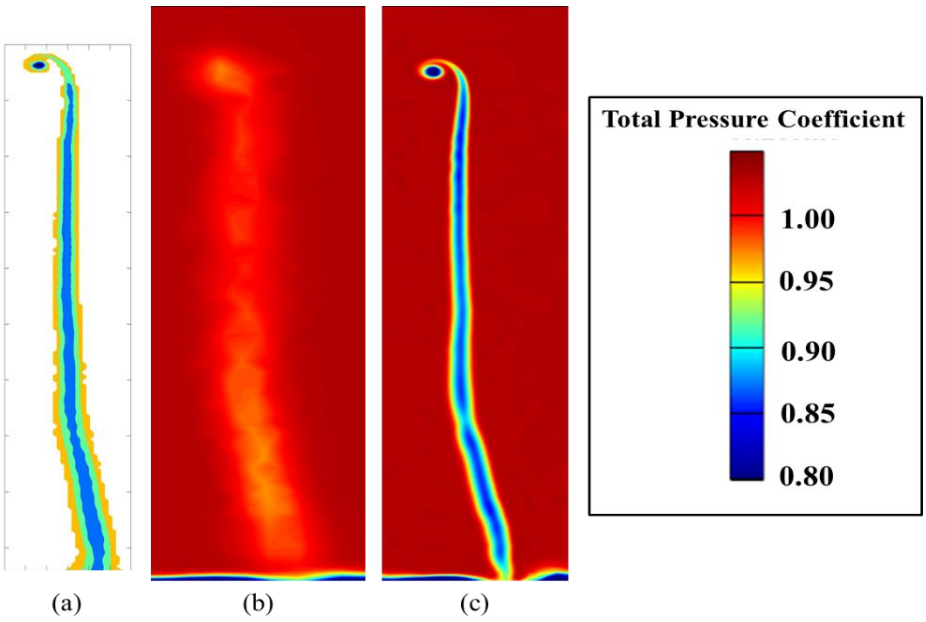

Fig. 2.6 Comparison of wake survey Total Pressure Coefficient contours for (left) wind tunnel, (middle) unrefined wake, and (right) refined wake.

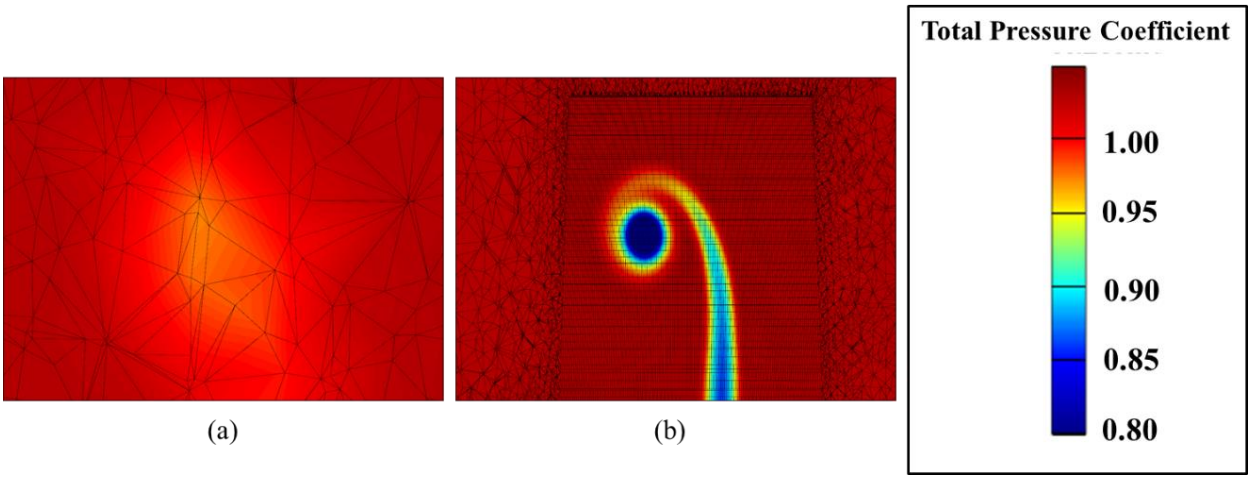

Fig. 2.7 Zoomed-in view comparing of the wing-tip vortex structure for the a) unrefined wake and b) the refined wake.

While Fig. 2.6 and 2.7 show that refining the region downstream of the swept-wing can produce results that are quite comparable to the experimental wake survey data, Fig. 2.8 and 2.9 focus on how the definition of the wake does or does not influence the pressure distribution along the surface of the wing. During the wind tunnel tests, surface pressures were collected at designated chordwise points along the span of the wing. These pressure ports were located at y/b = 0.11, 0.28, 0.44, 0.60, 0.81, 0.90. The main image in the top left of Fig. 2.8 and 2.9 shows the pressure contour along the upper surface of the wing where the images arrayed along its perimeter compare and contrast computational data to experimental data for the pressure distribution. These figures highlight two main points: 1) RANS k-ω SST is able to accurately capture the pressure distribution along the surface of the wing when compared to the experimental data, and 2) there isn't a noticeable effect on the pressure distribution of the wing with or without the wake refinement. The second point is further reinforced by the integrated aerodynamic coefficients in Table 2.2. When compared to the experimental data, there is a coefficient of lift percent error delta of 0.12% between the two meshes, and less than 0.01% error delta for the coefficient of drag.

Table 2.2 Comparison of integrated aerodynamic coefficients for experimental vs. computational data

	C_L	|% Error|	C_D	|% Error|
Experimental Data	0.635	-	0.0255	-
Without Wake Refinement	0.643	1.26	0.0267	4.70
With Wake Refinement	0.644	1.42	0.0267	4.70

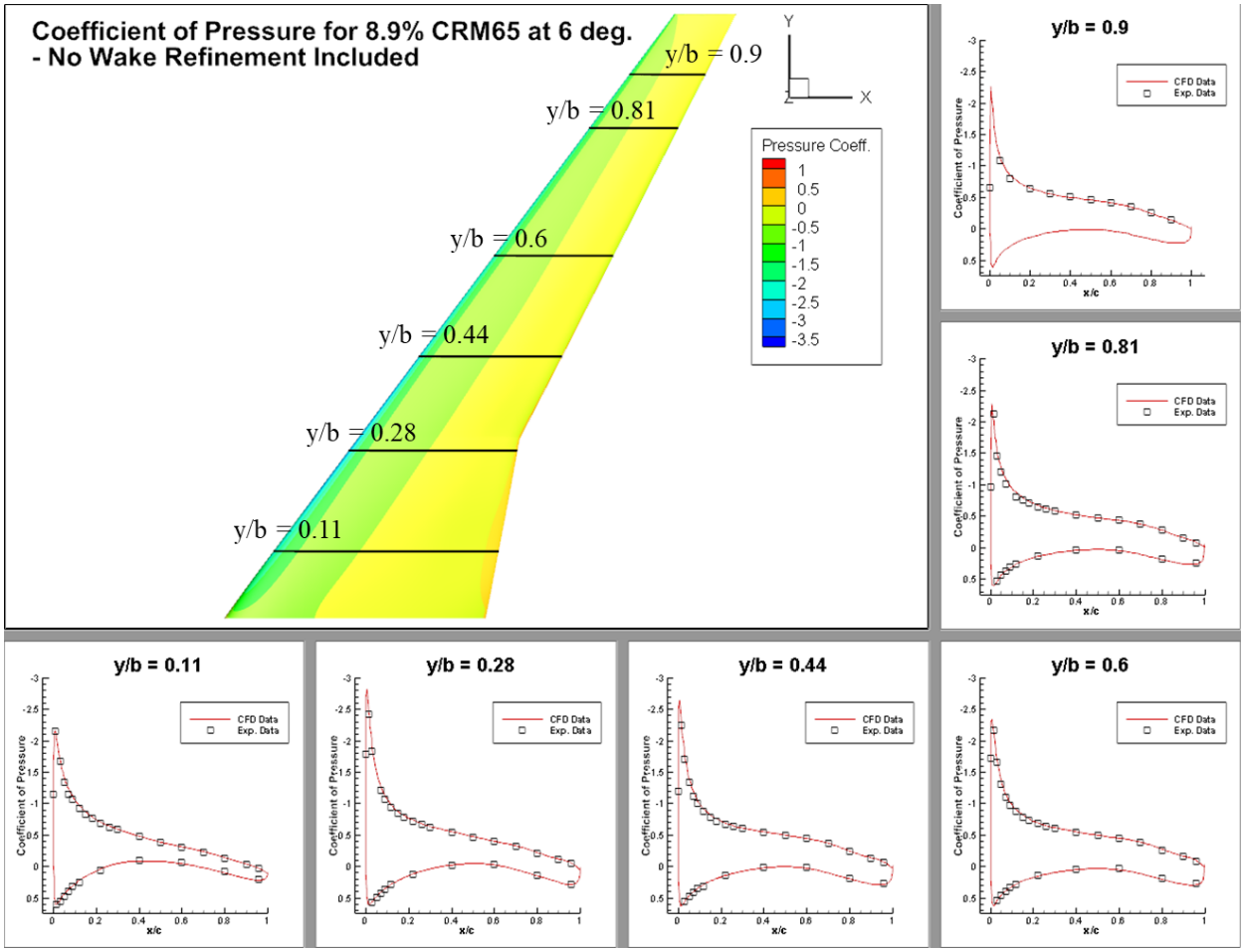

Fig. 2.8 Calculated coefficient of pressure surface contours for upper surface of swept-wing at 6-deg. angle of attack without wake refinement, with chordwise pressure distribution comparisons.

As noted in the Introduction, Lum *et al.* utilized a set of equations derived from Equations 2.1 and 2.2 in order to calculate lift and drag from the downstream wake of the wing [1]. The drag equation is based on the freestream stagnation pressure ($P_{t\infty}$), local stagnation pressure (P_t), freestream velocity magnitude (U_∞), and the components of the local velocity vector (u, v, w). The lift equation, as originally defined by Maskell, is based on integrating the y-location in the survey plane multiplied by the streamwise vorticity (ζ) [6]. Utilizing these equations, aerodynamic coefficients can be derived for both the downstream wake without refinement and with refinement. As seen in Table 2.3, while the refinement of the downstream wake proved to have very little influence on the aerodynamic coefficients integrated via surface pressure and shear stress, there is a considerable effect on the aerodynamic coefficients integrated via the wake capture plane. The errors produced by calculating Equations 2.1 and 2.2 over the refined wake, are an order less than those produced by the unrefined wake.

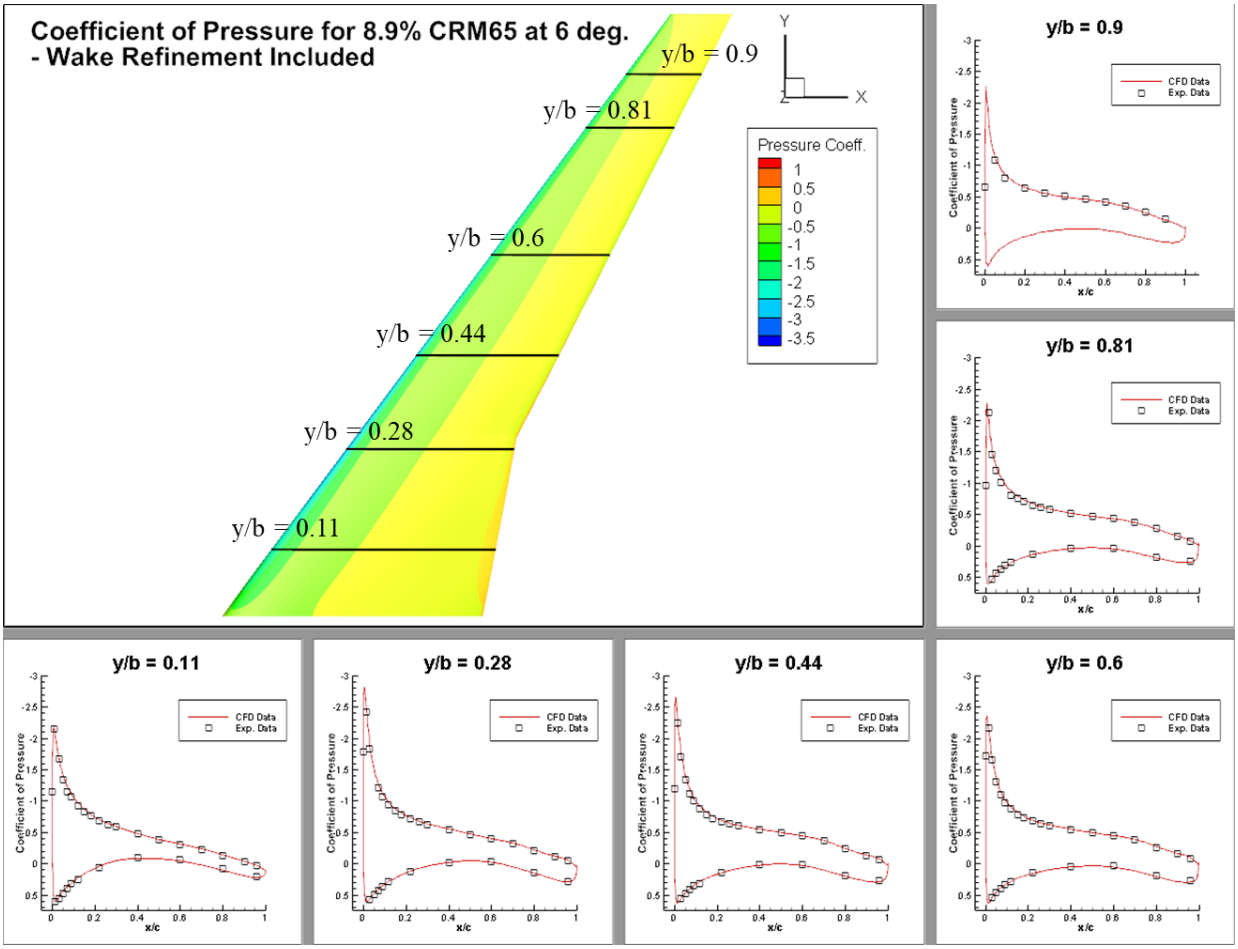

Fig. 2.9 Calculated coefficient of pressure surface contours for upper surface of swept-wing at 6-deg. angle of attack with wake refinement, with chordwise pressure distribution comparisons.

Table 2.3 – Comparison of aerodynamic coefficients for experimental vs. computational data derived from wake survey plane

	C_L	|% Error|	C_D	|% Error|
Experimental Data	0.635	-	0.0255	-
Without Wake Refinement	0.280	55.91	0.0151	40.78
With Wake Refinement	0.597	5.98	0.0264	3.53

4 - Conclusion

Recent experimental work has focused on developing and assessing the ability of a wake survey methodology to not only accurately capture the downstream wake of a model, but also utilizing the captured data to calculate the integrated aerodynamic coefficients of the model. The model used for this work was based on a 65% version of the Common Research Model (CRM).

While the work conducted by Lum *et al.* [1] focused on developing a methodology to capture the wake via an experiment-based approach, the effort outlined in this paper sought to provide a computational compliment. This study sought to complete two objectives by determining RANS *k-ω* SST's ability to capture the downstream wake and the impact the refinement of the wake has on the aerodynamic coefficients. To produce results comparable to the experimental data, the wing was modelled and simulated in a domain similar to the experimental tests.

Due to noticeable diffusion of the wake downstream of the wing during initial simulations, a set of 2D simulations were used to determine the appropriate refinement required to capture the wake structure through the wake survey plane defined by Lum *et al.* [1]. Utilizing the coefficient of total pressure to define the wake structure, the results of the 2D simulations enforced the need for appropriate cell resolution to avoid numerical diffusion of the wake. This trade study fed into the development of meshes that were utilized for the 3D simulations. In general, the results produced from the 3D simulations proved RANS *k-ω* SST's ability be able to accurately capture the integrated aerodynamic coefficients as well as the pressure distribution along the surface.

However, the simulations highlighted two important facts with regards to resolving the wake: 1) wake refinement had no major impact on the integrated aerodynamic coefficients derived from surface pressure and shear force, and 2) wake refinement is a necessity when utilizing the methodology outlined by Lum *et al.* [1]. When assessing the aerodynamic coefficients derived from surface pressure and shear force for both meshes, the error for the coefficient of lift was within 2% of the experimental value, while the error for the coefficient of drag fell within 5%. For aerodynamic coefficients derived from wake surveys (using Equations 2.1 and 2.2), the refined wake survey calculations produced errors of 5.98% and 3.53% for the coefficients of lift and drag respectively. In contrast, the error for the same equations across the survey lane without wake refinement yielded errors in aerodynamic coefficients that were an order higher. Thus, based on the results discussed, while it is unnecessary to the refine the downstream flow field of a swept-wing to capture relatively near model effects, proper definition of the numerical domain is essential to capture the impact of the model on its surrounding environment and to utilize the wake integrals correctly.

Chapter 2 References

[1] Lum, C. W., Sandhu, N., Diebold, J. M., Woodard, B. S., and Bragg, M. B., "The Application of a Five-Hole Probe Wake-Survey Technique to the Study of Swept Wing Icing Aerodynamics," *9th AIAA Atmospheric and Space Environments Conference, 2017,* 2017. https://doi.org/10.2514/6.2017-4374

[2] Vassberg, J., Dehaan, M., Rivers, M., and Wahls, R., "Development of a Common Research Model for Applied CFD Validation Studies," *26th AIAA Applied Aerodynamics Conference,* 2008. https://doi.org/10.2514/6.2008-6919

[3] Brune, G. W., "Quantitative low-speed wake surveys," *Journal of Aircraft,* vol. 31, 1994. https://doi.org/10.2514/3.46481

[4] Kusunose, K., and Kusunose, K., "Development of a universal wake survey data analysis code," 1997. https://doi.org/10.2514/6.1997-2294

[5] Betz, A., "A method for the direct determination of profile drag," *Zeitschrift für Flugtechnik und Motorluftschifffahrt,* vol. 16, 1925.

[6] Maskell, E. C., "Progress towards a method for the measurement of the components of the drag of a wing of finite span," *RAE Technical Report No. 72232,* 1972.

[7 Skinner, S. N., Green, R. B., and Zare-Behtash, H., "Wingtip vortex structure in the near-field of swept-tapered wings," *Physics of Fluids,* vol. 32, 2020. https://doi.org/10.1063/5.0016353

[8] Diebold, J. M., and Bragg, M. B., "Wake-Survey Technique for Iced Swept-Wing Aerodynamics," *AIAA Journal,* vol. 53, 2015, pp. 1712–1719. https://doi.org/10.2514/1.J053774

[9] Broeren, A. P., Woodard, B., Diebold, J. M., and Moens, F., "Low-Reynolds Number Aerodynamics of an 8.9% Scale Semispan Swept Wing for Assessment of Icing Effects," *9th AIAA Atmospheric and Space Environments Conference*, Denver, CO, 2017. https://doi.org/10.2514/6.2017-4372

[10] Wilcox, D. C., *Turbulence Modeling for CFD*, La Canada, CA: DCW Industries, 1994.

[11] Menter, F. R., "Two-Equation Eddy-Viscosity Turbulence Models for Engineering Applications," *AIAA Journal,* vol. 32, 1994. https://doi.org/10.2514/3.12149

Chapter 3

Aerodynamics of a Common Research Model Wing with Leading Edge Ice Shape

1 – Introduction

Ice accretion is a critical part of aircraft design and certification for flight safety, but one which is not well understood in terms of the three-dimensional aerodynamics for commercial aircraft wing geometries. One reason is that experimental data for ice shapes has not been previously publicly available for modern geometry aircraft wings. To determine the ice shapes which can accrete on such wings, experimental data was collected at the NASA Glenn Research Center Icing Research Tunnel's (IRT) during a swept-wing icing project, with details provided by the following references [1, 2]. The objective of that project was to generate a database of ice-accretion geometries that can be used for development and validation of icing simulation tools as well as for aerodynamic testing. For the swept-wing icing project, ice shapes were accreted at the leading edge of a hybrid model that maintained a full-scale leading edge, but a truncated body, of a 65% scale Common Research Model (CRM65). The resulting ice accretions reasonably matched expected geometric complexities based on previous ice accretion testing of swept-wings, such as "scallops" and ice roughness [3]. The results from aerodynamic testing also indicated that significant flow separation occurred even for moderate angles of attack, and that the aerodynamics are generally complex and highly three-dimensional [4]. The potential for unsteady flow features and fluctuating aerodynamic loads associated with a highly three-dimensional flow can theoretically adversely affect flight aerodynamics and thus aircraft operation and safety.

Aircraft design and certification for flight in icing conditions represents a large potential cost due to the combination of wind tunnel tests and flight tests that can be involved. Zeppetelli *et al.* [5] have shown that Computational Fluid Dynamics (CFD) offers a potential solution to this problem due its ability to identify a problem at the beginning or early phases of the design processes for an aircraft. With the advancement of simulation methodologies and development of proper resolution of the flow structures relevant to iced aerodynamics, CFD can be a strong companion to experimental testing and can help save significant costs in the aircraft design and icing certification processes. However, predicting such flows can be challenging since ice accretion causes large regions of highly complex flow separation. There have been many unsteady approaches that attempt to capture these complex flow large eddy features in the separated zones

with varying degrees of success, as shown by Alam *et al.* [6], Zhang *et al.* [7], and Xiao *et al.* [8]. The reader is referred to these studies for further details, but it should be noted that these studies did not directly investigate a swept iced wing as is investigated herein. It will be shown that the current flow has strong spanwise flow effects, which appear to render it more amenable to conventional turbulence modeling.

The wide variety of approaches and methods to predict the flow dynamics of lifting surfaces with ice, differ primarily based on the treatment of the turbulence as discussed in the review by Stebbins *et al.* [9]. The most conventional and common approach is to use Reynolds–Averaged Navier-Stokes (RANS) with a turbulence model for closure to compute the steady mean flow. However, modern swept-wings with leading edge ice represent a highly complex flow that can incur significant flow separation and unsteadiness. As such, another option for aerodynamic flows with separation is to use unsteady computational approaches such as the Detached Eddy Simulations (DES) method by Spalart *et al.* [10]. This methodology is a hybrid coupling of Reynolds–Averaged Navier-Stokes (RANS) and Large Eddy Simulation (LES) techniques. The DES approach was first successfully applied to iced airfoil and wings by Pan *et al.* [11] to capture wake effects. While hybrid RANS-LES (HRL) models have shown results that reasonably predicted aerodynamic flows of iced airfoils with complex substantial flow separation, it was not clear that they improved predictions as compared to RANS, despite the additional computational requirements and complexity of implementing the DES approach [9].

Despite their promise, none of the aforementioned computational techniques have investigated nor evaluated three-dimensional ice shapes on modern swept commercial aircraft wings based on current publicly disseminated work. Furthermore, there has not been a detailed comparison of a RANS technique against experimental data for such flows. The last known study to provide a similar comparison was done by Kwon *et al.* using a Baldwin-Lomax model [12]. As such, the current study tries to address the open question regarding the fidelity of 3D RANS for modern wings with sweep (like the CRM65) coupled with leading edge ice shapes. This computational investigation complements an experimental program to understand iced wing aerodynamics by a consortium of organizations including NASA, the Federal Aviation Administration (FAA), the Office National d'Etudes et Recherches Aérospatiales (ONERA), Boeing, the University of Illinois, the University of Virginia, and the University of Washington. The goal of the present study is to both explore the fidelity and robustness of RANS and use these results combined with experimental data to develop a basic understanding of the flow physics for an 8.9% scale version of the CRM65 wing with and without an ice shape at various angles of attack, including conditions where there is substantial spanwise flow separation. This is the first such study to the authors' knowledge.

2 – Computational Domain & Methodology

2.1 – Problem Description

An 8.9% scale version of the semi-span swept CRM65 wing is studied herein. The CRM65 wing is based upon the Common Research Model (CRM) developed by Vassberg *et al.* [13-14] in order to provide a contemporary experimental database to directly support the validation of specific applications of CFD for modern day commercial airplanes. The CRM65, as described by Broeren *et al.* [1], was selected for their experimental tests due to the necessity to reduce the potential adverse effects associated with modeling Vassberg *et al.*'s full CRM wing in the NASA's

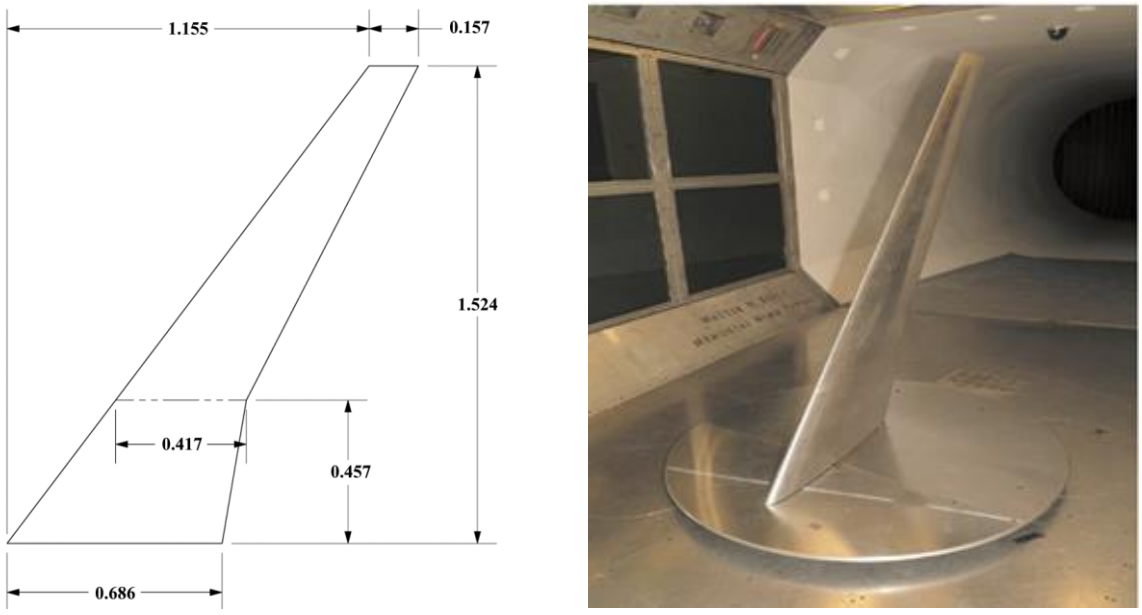

(a) (b)

Fig. 3.1 The 8.9% scaled CRM65 semi-span wing (a) planform with key dimensions labeled in meters and (b) installed in Wichita State Wind Tunnel. [15]

IRT. This intermediate scaled geometry remains comparable to modern day commercial aircraft that are similar in size to a Boeing 757 [1]. The final 8.9% scale was employed to allow for aerodynamic testing in the Wichita State University's Walter H. Beech Wind Tunnel, as seen in Fig. 3.1.

The experimental studies that are used for validating this study's numerical method were performed by Broeren *et al.* [15] and Camello *et al.* [4]. These studies collected data via force balance measurements, surface pressure taps, oil flow visualizations, and mini tufts at a Reynolds number of $1.6 \cdot 10^6$ and a Mach number of 0.18. The overall flow properties were selected to match the experimental setup of Broeren *et al.* [15]. The angles of attack for this study were selected in order to not only determine stall mechanisms (as defined in Ref. [16]) in the flow field, but also determine the ability of RANS to predict the flow field when there is a large amount of separation.

For the present computations, a computational domain with a cross section selected to match the aforementioned WSU's wind tunnel was used in this study. The key features for this wing model include a span of 1.524 m, a mean aerodynamic chord (MAC) of 0.4234 m, a taper ratio of 0.23, and a leading-edge sweep angle of 37.2-deg., where further details are outlined by Broeren *et al.* [15]. The present study modeled all of the walls of the wind tunnel as viscous surfaces in order to utilize the uncorrected aerodynamic data collected during the experimental tests. However, there are a few differences between the experimental wind tunnel and that which is simulated herein. Firstly, though the wind tunnel was only 3.658 m in length, the computational domain included an extended tunnel length, with an outflow pressure-based boundary condition set at a location of 30·MAC downstream and an inflow velocity-based boundary condition located at 10·MAC upstream from the center of rotation. This change was implemented in order to ensure uniform flow upstream of the model and no back pressure effects from the outflow downstream of

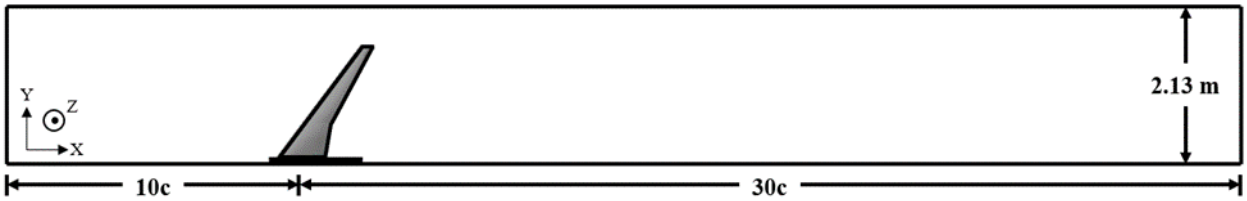

Fig. 3.2 Schematic of the computational domain used for the simulations, where "c" is the mean aerodynamic chord (MAC) which is 0.423 m.

the model. Secondly, the corner chamfers of the wind tunnel, which can be seen in if Fig. 1b, were not included in the computational domain for the sake of simplicity. Lastly, while this study did model the splitter plate at the base of the wing, the experimental streamline shroud separating the tunnel floor from the splitter plate was not modeled. This was done because previous CFD work presented by Broeren *et al.* [15] indicated that the absence of a streamline shroud had negligible effect on the wing aerodynamics. Furthermore, the influence of the boundary layer thickness changes on the splitter plate had a negligible effect on the lift and drag of the model section However, the computational model still included a 6.23 cm gap between the bottom of the wing geometry and the floor. The final computational domain measured 2.134 m high by 3.048 m wide by 19.68 m long and can be seen in Fig. 3.2.

The 8.9% scaled CRM65 wing was studied with and without an ice shape on the leading edge. The latter case allowed for validation of both the gridding method used in this paper and the RANS *k-ω* SST method to capture swept-wing aerodynamics. Though examining the flow-field characteristics of a clean swept-wing does provide a variety of insights into different flow field characteristics, the intent of this study is to understand the flow field features caused by the presence of the ice shape along the leading edge of the upper surface. The ice shape examined by this paper was derived from ice accretions created in NASA's IRT, which can be seen in Fig. 3.3. These shapes were captured via laser scans and then converted into three-dimensional models, as described in Camello *et al.* [17]. As seen in Fig. 3.3c, the specific ice shape used herein was based on a simplification of the spanwise variation of the highly three-dimensional original ice shapes.

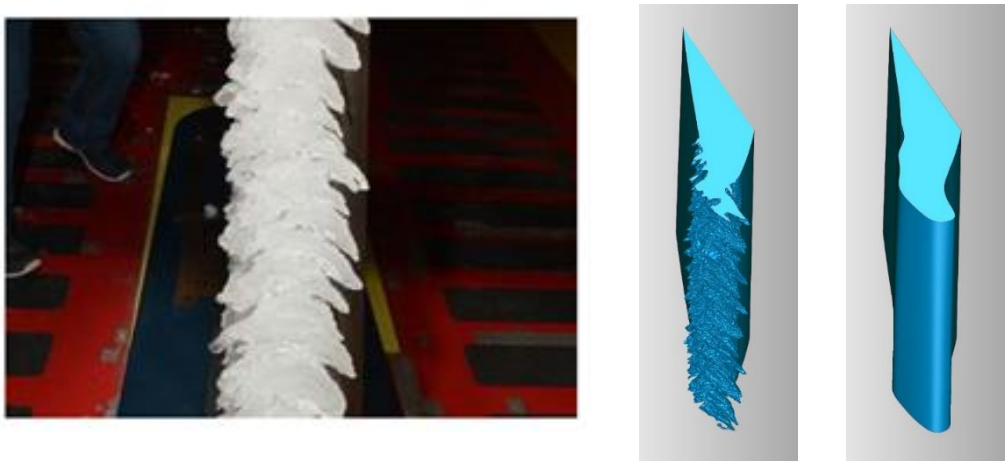

(a) (b) (c)

Fig. 3.3 a) Photograph of ice accretion on the IRT model with b) a high-fidelity model produced via laser scanning, and d) a simplified model as defined by Camello *et al.* [17]

2.2 – Numerical Methodologies

The Reynolds-averaged Navier-Stokes (RANS) equations for turbulent flow are based on a time-averaging of the unsteady Navier-Stokes equation, which results in a Reynolds stress term that must be modeled in order to close the equations. Two-equation eddy-viscosity turbulence models are widely used in many engineering applications because of their lower computational cost than other closure methods, as well as reasonable accuracy, e.g., the standard k-ε model solves two transport equations for the turbulent kinetic energy (k) and its dissipation rate (ε). As the strengths and weaknesses of this standard k-ε model have become known, modifications have been introduced to improve its performance. Wilcox [18] developed the k-ω model to improve the model performance for low-Reynolds number effects, compressibility, and shear flow spreading. The Wilcox k-ω model models the sublayer of the boundary layer, and solves a transport equation for the specific dissipation ratio (ω), which is the ratio of ε to k. Compared to previous two-equation models, the Wilcox k-ω model has better numerical stability and the performance of the k-ω model in the logarithmic region of a boundary layer is generally superior to that of the k-ε model. However, because the k-ω model can have excessive freestream sensitivity, Menter [19] proposed a new two-equation model, called the Shear-Stress Transport (SST) k-ω model, that combine both the k-ω model and the k-ε model. To achieve the desired features in the different regions, Menter utilized a blending function and made sure the standard k-ω model is activated in the near-wall region and the modified k-ε model is switched back in the free-shear region. Furthermore, to improve the performance in the adverse pressure gradient flow as well as the accuracy of prediction of the location of flow separation, Menter [19] modified the turbulent viscosity formulation to account for the transport effects of the principal turbulent shear stress. Due to its great success, the SST model is perhaps the most commonly used RANS two-equation turbulence model employed today.

In the present study, the RANS equations with the SST k-ω model is chosen, and the simulations were implemented in ANSYS Fluent, a commercially available CFD code [20]. In this model, k and ω are solved in two transport equations:

$$\frac{\partial(\rho k)}{\partial t} + \frac{\partial(\rho k V_i)}{\partial x_i} = \frac{\partial}{\partial x_j}\left[(\mu + \sigma_k \mu_t)\frac{\partial k}{\partial x_j}\right] + G_k - Y_k \tag{3.1}$$

$$\frac{\partial(\rho \omega)}{\partial t} + \frac{\partial(\rho \omega V_i)}{\partial x_i} = \frac{\partial}{\partial x_j}\left[(\mu + \sigma_\omega \mu_t)\frac{\partial \omega}{\partial x_j}\right] + G_\omega - Y_\omega + D_\omega \tag{3.2}$$

where ρ is density, V refers to the fluid mean velocity, while the turbulent kinetic energy generation terms (G_k, G_ω), the dissipation terms (Y_k, Y_ω), and the cross-diffusion term (D_ω) are described in Ref. [19]. Each constant in this model is a blend of two constants by using a blending equation, and the blending function was designed to be unity in the sublayer and logarithmic region of the boundary layer and to gradually switch to zero in the wake region.

2.3 – Meshing Technique

All mesh generation in the present study was performed using a commercial gridding software called Pointwise. The meshes utilized Pointwise's anisotropic tetrahedral extrusion method (T-

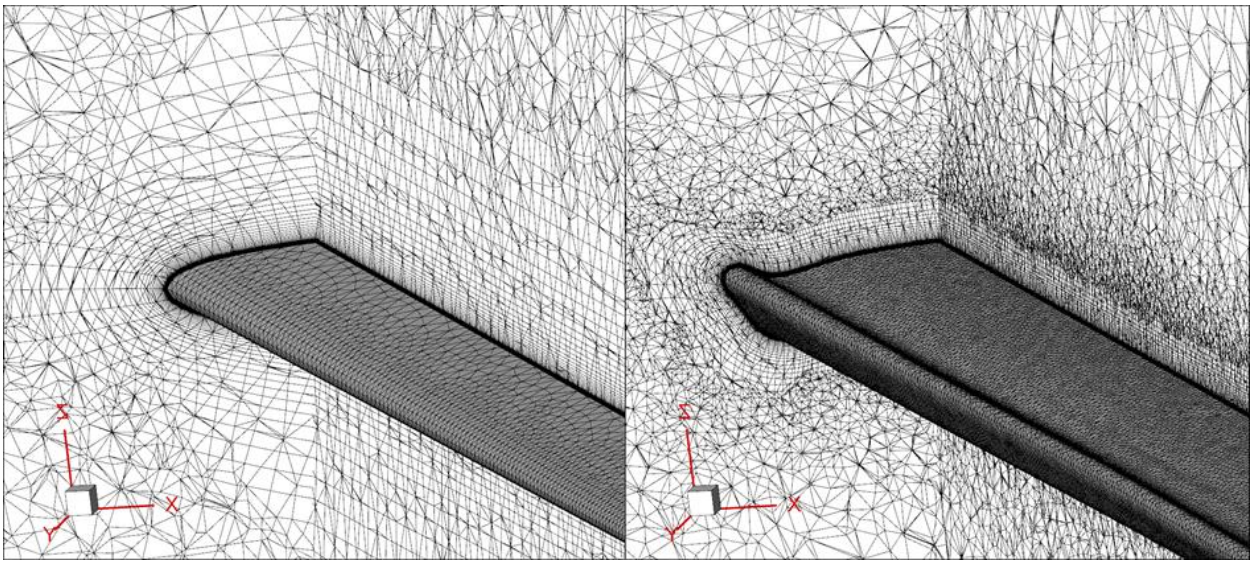

(a) (b)

Fig. 3.4 Example of orthogonal cross-sectional view of the mesh generated for both the a) non-iced wing and b) iced wing at *y/b* = 0.28.

Rex) [21] to create unstructured boundary layer meshes. The meshing process begins with first discretizing the surface of the wing, which can be seen in Fig. 3.4. When discretizing the wing surface, it is imperative to ensure that the leading edge and trailing edge of the wing is well defined in order to properly capture the flow physics. When comparing the meshing requirement between the geometry with and without ice, the ice shape introduces complex curvatures to the surface that must be well refined. Without properly discretizing the geometry of the ice shape by using a highly refined mesh, the resulting mesh can inappropriately smooth out the ice shape's features. Thus, as can be seen in Fig. 3.4b, the number of nodes for the geometry of the ice shape along the leading-edge portion of the wing was drastically increased as compared to the rest of the surface.

As for the rest of the domain, for the clean (un-iced) geometry's baseline mesh, the boundary layer grid for the configurations was grown to a maximum layer count of 50 layers using a growth rate of 1.15 and a boundary decay of 0.95. Boundary decay is defined as the rate at which the isotropic unstructured mesh cell size set by the size of the surface triangles, transitions to the mesh's maximum isotropic cell size in the domain. Standard meshing criterion were used including making sure that the wall normal grid resolution in the boundary layer has sufficient resolution near the wall. In order to ensure a $y+$ equal to 1 for the grid, an initial grid height, Δs, of 6.452 μm was imposed on the extrusion. Similar to the clean geometry, the boundary layer for the iced geometry was grown with the same characteristics (growth rate and y+ value). From Fig. 3.4, the most notable difference between the two meshes is the extent of the boundary layer growth into the far field. This is due to the T-rex methodology, which grows layers until the final layer either reaches a stopping criterion or the local cells are isotropic. With the same initial step size and growth rate, a geometry's surface that is discretized by smaller cell sizes will thus reach isotropy sooner. Figure 3.5 provides another illustration of this artifact via cross-sectional views of both geometries alongside close-ups of the leading edge. Averaging over every angle of attack, the domain for the un-iced wing is composed of $24.4 \cdot 10^6$ nodes and $52.3 \cdot 10^6$ cells, while the domain for the iced-wing is composed of $28.1 \cdot 10^6$ nodes and $70.2 \cdot 10^6$ cells. The number of iterations

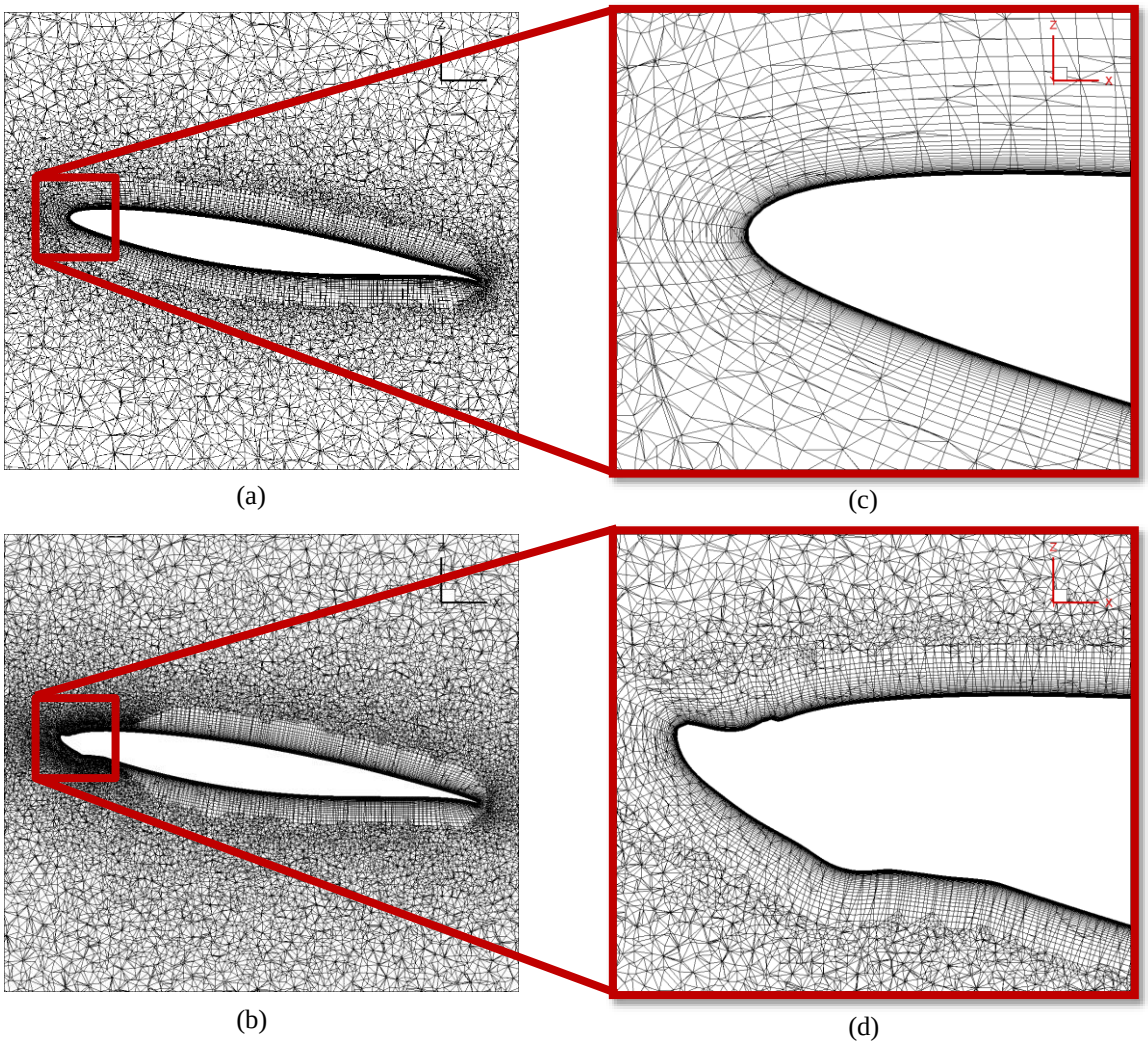

Fig. 3.5 a-b) Example of cross-sectional view of the mesh generated for both the non-iced and iced wings at a *y/b* = 0.28 and c-d) close up of the leading edge of the geometries.

required to come to a converged solution for this mesh was dependent upon the angle of attack. Convergence was based on the change in value of a given coefficient was less than 0.001% for at least 5,000 iterations. At an angle attack of 2-deg., 20,000 iterations were needed, while at an angle of attack of 10-deg., 120,000 iterations were needed.

A grid convergence study was performed for the iced wing at an angle of attack of 8-deg. For the refined mesh, the number of nodes along the upper surface of the wing was doubled in order to ensure finer discretization of both the wing surface and the T-rex methodology away from the wall. In combination with refining the surface, the section of the modeled wind tunnel in close proximity to the model, was also refined in order to help reduce the growth of the cells connecting the wall to wing. This refinement was achieved by reducing the max cell edge length defining the wall boundary condition from 5.08 cm to 2.54 cm. The refined mesh is composed of $36.0 \cdot 10^6$ nodes and $101.0 \cdot 10^6$ cells. Since this increase in resolution had a negligible effect (as shown in Results section), it was concluded that the flow solutions are grid independent and further grid refinement was not necessary.

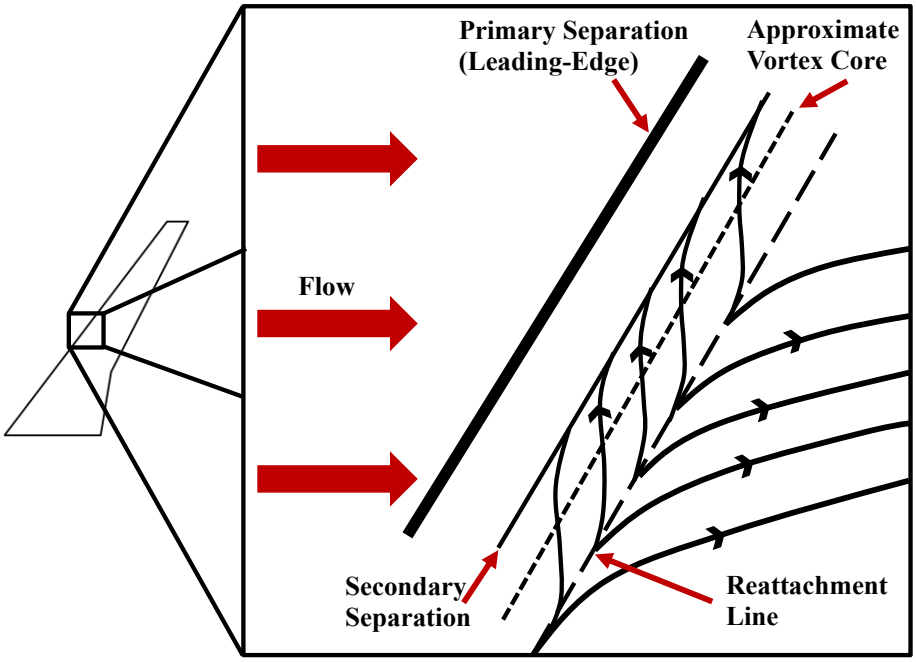

Fig. 3.6 Schematic of surface streamlines caused by flow separating at the leading-edge and creating a vortex with separation and reattachment lines based on sketch in Ref.[22].

3 – Results

The following will focus on results for the 8.9% scaled CRM65 wing with and without a leading-edge ice shape. Both sets of results will present data in the form of pressure distribution and aerodynamic coefficients (i.e., lift, drag, and pitching moment) at angles of attack of 4, 6, 8, and 10-deg. For the geometry with an ice shape, experimentally collected mini-tufts and oil flow visualization data are compared with computationally-calculated wall shear stress in order to characterize the flow near the surface of the wing.

3.1 – Surface Flow Field Visualization

Oil flow visualization and mini-tufts were captured experimentally in order to examine the flow near the surface of the wing. Both of these techniques are used to visually provide insight on the fluid dynamics of the region closest to the surface of a wind tunnel model. Oil flow visualization leverages the use of oil dabs placed strategically upstream along a model's surface such that flow patterns are formed as the wind tunnel runs. The benefit of this technique is that oil can highlight areas of separation due to its inability to penetrate separation boundaries. Mini tufts on the other hand, are placed intermittently along the whole surface of the wind tunnel model. They are used to both understand the direction of the flow along the surface, as well as determine if there are any regions of unsteady flow features based on the frequency and magnitude of their fluctuations over time. Both of these experimental sets are compared to the wall shear stress calculated by the numerical methodology used in this paper.

The comparison is conducted using the in-depth analysis provided by Poll *et al.* [22] on the stalling characteristics of a swept-wing. Figure 3.6 is a rendition of a figure highlighted in their study, but herein modified towards the specific geometry analyzed in this study. As shown in Fig. 3.6, a swept-wing during flow separation creates a leading-edge vortex with a primary and

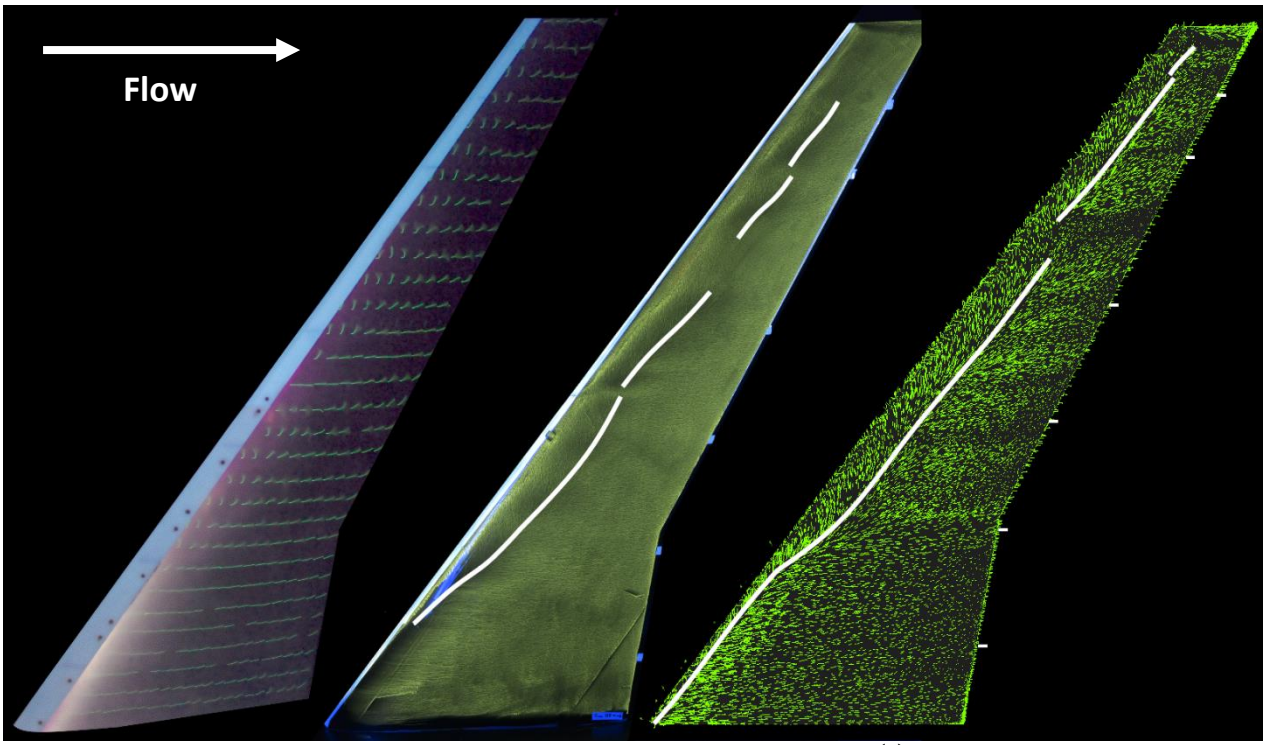

(a) (b) (c)

Fig. 3.7 Comparison of surface flow patterns at 6-deg. angle of attack for: a) experimental mini tufts, b) experimental oil flow visualization, and c) computational wall shear stress for the baseline mesh of the iced swept-wing. White lines are superimposed on b) and c) to indicate flow reattachment location.

secondary separation region that tends to run from the root of the wing to the tip. This leading-edge vortex is composed of a separation line, a vortex core, and a reattachment line. The separation line is just aft of the leading edge of the wing while the reattachment line is further downstream. The location of the reattachment line is dependent upon the strength of the vortex. Between these two lines, the flow tends to move from the reattachment line towards the separation line. Treating the separation and reattachment lines as asymptotes, the flow between the two lines tend to exhibit an s-shaped pattern. As seen in Fig. 3.6, these streamlines have an inflection point that correlates to the vortex core. As the angle of attack increases, the starting location of the separation tends to move closer to the root of the wing and the separation region grows in length in the chordwise direction. Herein, we will refer to this type of flow separation, which is dominated by strong spanwise flow as "swept stall." This differs from the classical two-dimensional airfoil stall which has been defined as occurring when an airfoil is at a high enough angle of attack such that the flow separating from the leading edge of the airfoil can no longer reattach to the suction side of the airfoil. When this occurs, large unsteady flow features due to highly chaotic bluff body separation dominate the flow field and negatively impact the aerodynamic performance of the airfoil. However, the spanwise components of flow on a stalled swept-wing induced by the sweep of the wing can have a much more controlled flow separation region [21], which may make it more amenable to conventional RANS predictions.

To quantify the flow patterns for the present geometry and angles of attack, experimental flow visualizations are compared to the numerically-calculated wall shear stress as shown in Fig. 3.7 for the 6-deg. angle of attack iced wing case. For the mini tufts, attached flow is reflected by the

tufts aligned with the streamwise direction whereas tufts aligned in the spanwise direction or towards the leading edge, indicate regions of separation. For the oil flow visualization and wall shear stress images, white lines were added along the reattachment lines based on Poll *et al.*'s definition [22]. Both the mini tufts and the oil-flow visualization show that there are regions of separation just aft of the leading edge. The presence of these separation regions show that the ice shape causes an earlier onset of this stall-like separation behavior when compared to a clean swept-wing [15]. In general, the separation zone, which includes both the primary and secondary separation, has a chord wise length that is initially small at y/b=0.11 and then expands significantly to about 20% of the chord length by the Yehudi break (y/b=0.28). Thereafter, the region is approximately constant in length towards the wing tip. Because of the wing taper, this is consistent with a greater chordwise fraction of separation as this region moves towards the wing tip. Notably, the oil flow shows a series of breaks in the separation line with significant spanwise variations. These breaks and the strong spanwise flow component indicate that the leading-edge ice on this wing results in a "swept stall" flow separation which is demonstrably different from classical two-dimensional airfoil flow separation.

Computationally, RANS is generally able to predict the overall pattern of flow separation seen in the oil flow visualization. However, the extent of the separation in the chordwise direction is much less significant at y/b=0.2, and in general is somewhat underpredicted for the remaining outboard portions. The RANS predictions show similar breaks and variations in the separation line as seen in the oil flow visualization, though not as many breaks. Further examining the additional breaks in the experimental data, the absence of a clear direction of the flow along the surface of the wing can be related to a weak flow influence on the oil on the surface of the wing, associated with a nearly "dead flow" zone. This claim is supported by the relatively small magnitude of the vectors defining the wall shear stress computed by RANS. Such a weak flow combined with multiple separation breaks is consistent with a separation flow pattern that is highly unsteady and unstable. Overall, the RANS predictions for flow separation are quite reasonable, especially considering flow separation on complex three-dimensional surfaces is notoriously difficult to predict. While the refined grid produces a slightly more advanced flow separation region inboard and some small differences in the dead region flow directions, overall these are small compared to the differences with respect to the experimental flow visualization results. Furthermore, as will be shown the overall three-dimensional pressure distributions, these features are even less sensitive to grid effects, indicating that these dead zone differences do not drive the aerodynamic properties (other grid resolution studies were informally completed, and the differences were highly consistent with that at 8-deg). As such, the basic flow features are largely independent of grid resolution, and the small differences between predictions and measurements can be attributed to the empirical nature (and associated uncertainty) of turbulence modeling. However, to better understand the flow physics occurring in this swept stall region, it is herein recommended to conduct instantaneous unsteady three-dimensional experiments and simulations in both chordwise and spanwise planes. In addition, an improved understanding of the three-dimensional character of the spanwise running flow above the wing surface (including mean separation streamlines and vorticity fields) would provide better understanding of swept stall on iced wings.

For angles of attack of 8-deg. and 10-deg., both Figs. 3.8 and 3.9 respectively show that in terms of accuracy, RANS is able to predict the pattern captured in the experimental data. Starting near the Yehudi break, both the mini-tufts and oil flow visualization show majority of the flow being directed towards the wing tip or the leading edge. Using Poll's [22] description (Fig. 3.6), this suggests the presence of swept stall along majority of the upper surface of the wing. The

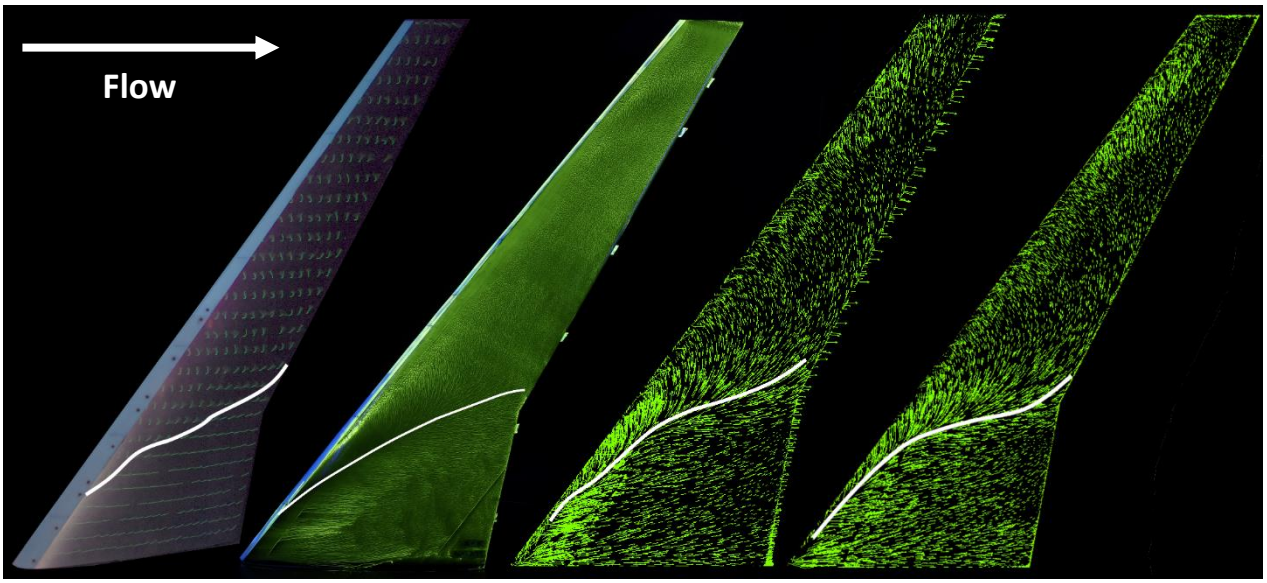

(a) (b) (c) (d)

Fig. 3.8 Comparison of surface flow patterns at 8-deg. angle of attack for: a) mini tufts, b) oil flow, c) baseline mesh, and d) refined mesh computational wall shear stress for the iced swept-wing. White lines again indicate flow reattachment location.

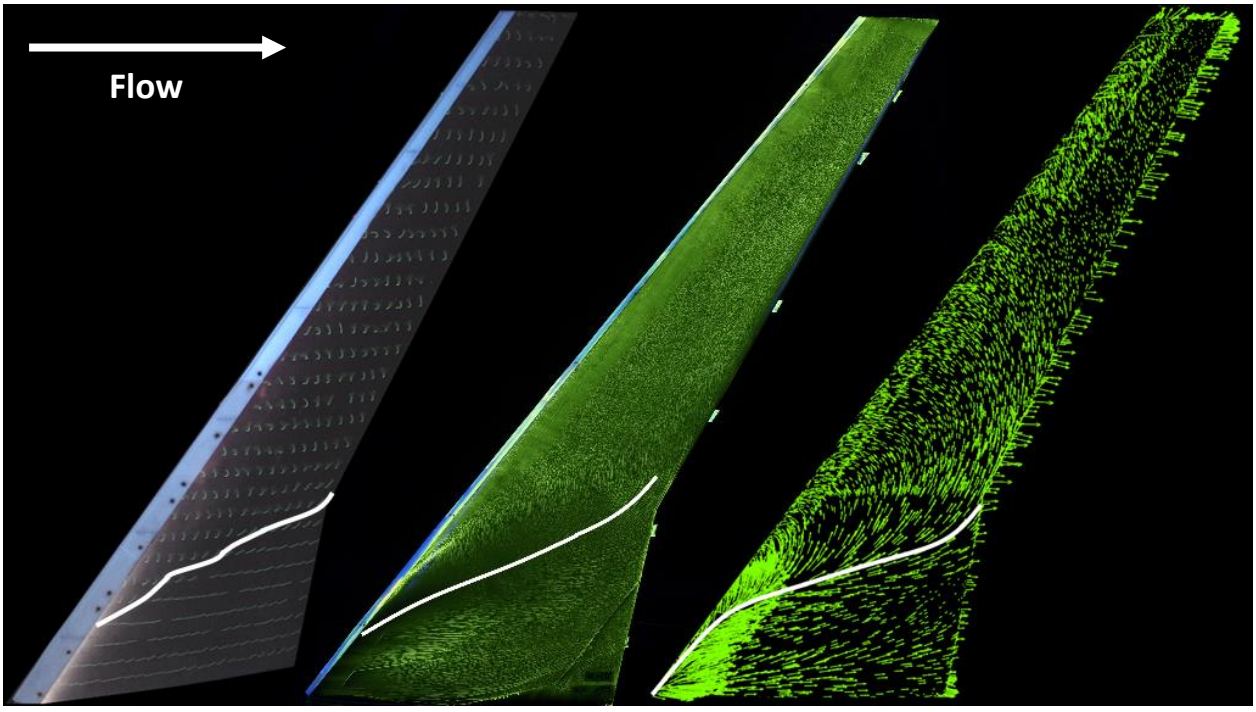

(a) (b) (c)

Fig. 3.9 Same as Fig. 3.8 except for 10-deg angle of attack. (Note: (c) shows the refined mesh)

computed wall shear stress shows that RANS is able to accurately predict this large region of stall. The wall shear stress also shows that the flow begins to significantly separate around a spanwise location of *y/b* = 0.11 and significantly grows in the chordwise direction until the wing is completely stalled near the Yehudi break. The difference between the 8-deg. and 10-deg. case is the extent of the separation along the upper surface. The gradual increase of flow separation and leading edge vortex size along the upper surface of the wing as the angle of attack increases, was similarly seen in the swept NACA0012 studied by Kwon & Sankar [12]. Comparing the baseline mesh to the refined mesh for 8-deg., while there are some minor variances in the flow visualization between the two meshes near the root of the wing (the refined mesh shows faster reattachment), they both exhibit very similar wall shear patterns along the upper surface of the wing. Further analysis on the impact of this difference due to grid resolution will be discussed in the pressure distribution and aerodynamic coefficient section. To summarize the flow visualization results, there are some small discrepancies between the experimental data and computational data at 6-deg. where the swept stall has first significantly appeared (flow separation is small for 4-deg.), but RANS is able to well predict the flow field captured by the oil flow visualization for the iced swept-wing at the higher angles of attack studied (8-deg. and 10-deg).

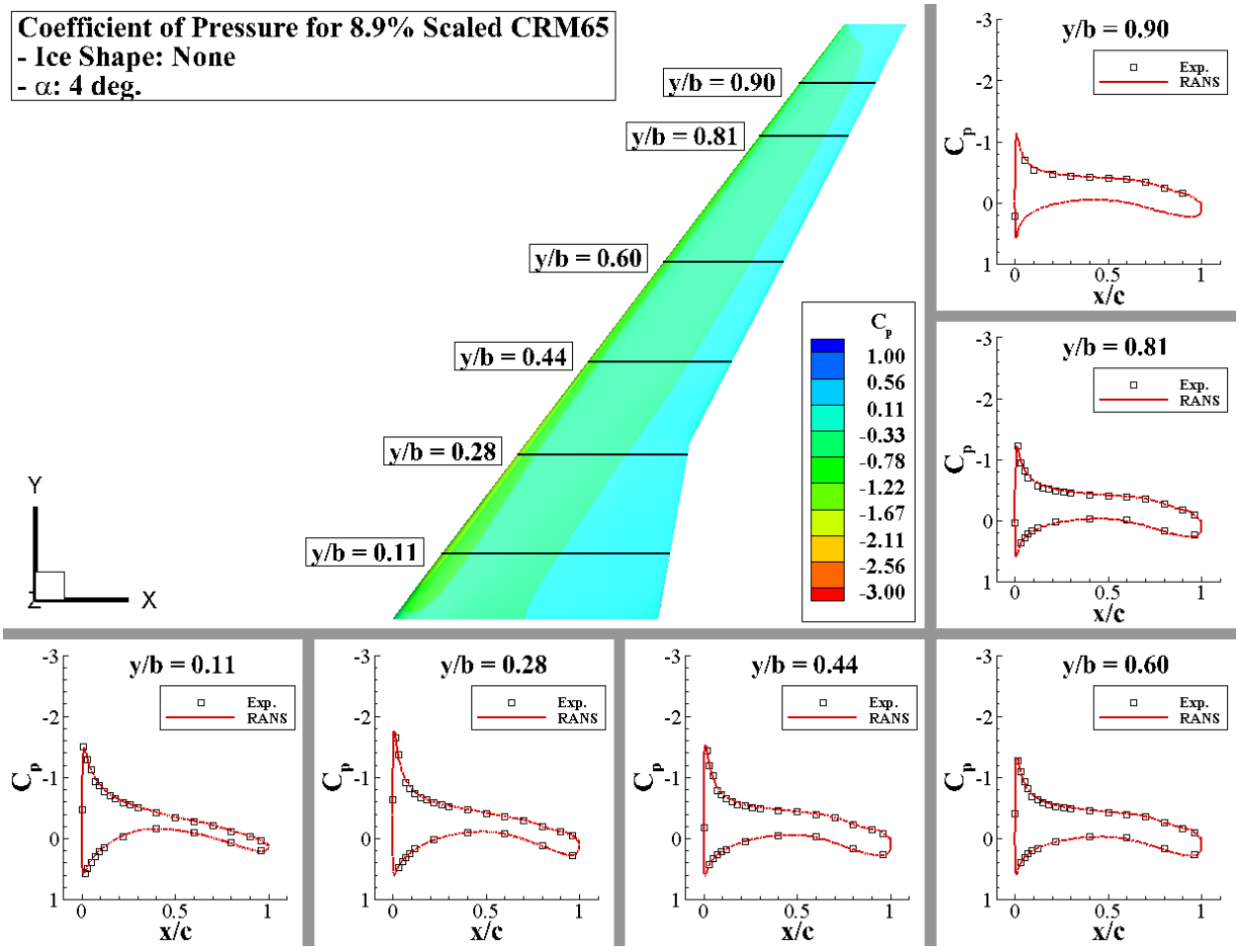

Fig. 3.10 Calculated coefficient of pressure surface color contours for upper surface of non-iced wing at 4-deg. angle of attack with chordwise coefficient of pressure distribution comparisons at six spanwise locations.

3.2 – Pressure Distributions

The experimental model included pressure taps in 10 streamwise rows along the surface of the wing [15]. at *y/b* = 0.11, 0.28, 0.44, 0.6, 0.81, and 0.90. Figures 3.10 through 3.16 provide the predicted coefficient of pressure contours along the upper surface of the wing geometries derived from the RANS results. The figures also present a quantitative comparison of the experimental and computational pressure distribution at fixed *y/b* locations at angles of attack of 4, 6, and 8-deg for clean wing (no ice shape) and wing with ice shape. The first pair of comparisons to consider is provided by Fig. 3.10 and 3.11 for the un-iced and iced geometries respectively at an angle of attack of 4-deg. For both figures, the upper surface pressure contours show very little variation along the span of the wing. In terms of the pressure distribution at the selected *y/b* locations, RANS *k-ω* SST accurately captures the experimental trends for this 4-deg. case for both clean and ice-shape configurations. While the clean wing exhibits little variation in pressure coefficient distribution along the span, the iced wing presents a different story. Starting around *y/b* = 0.60 in Fig. 3.11, both the experimental and predicted pressure distribution curves show a plateau of constant pressure near the leading edge of the wing. Diebold *et al.* [23] have attributed this plateau to the presence of a leading-edge vortex being formed aft of the ice horn. The strength of the leading-edge vortex and associated flow separation increases as *y/b* increases.

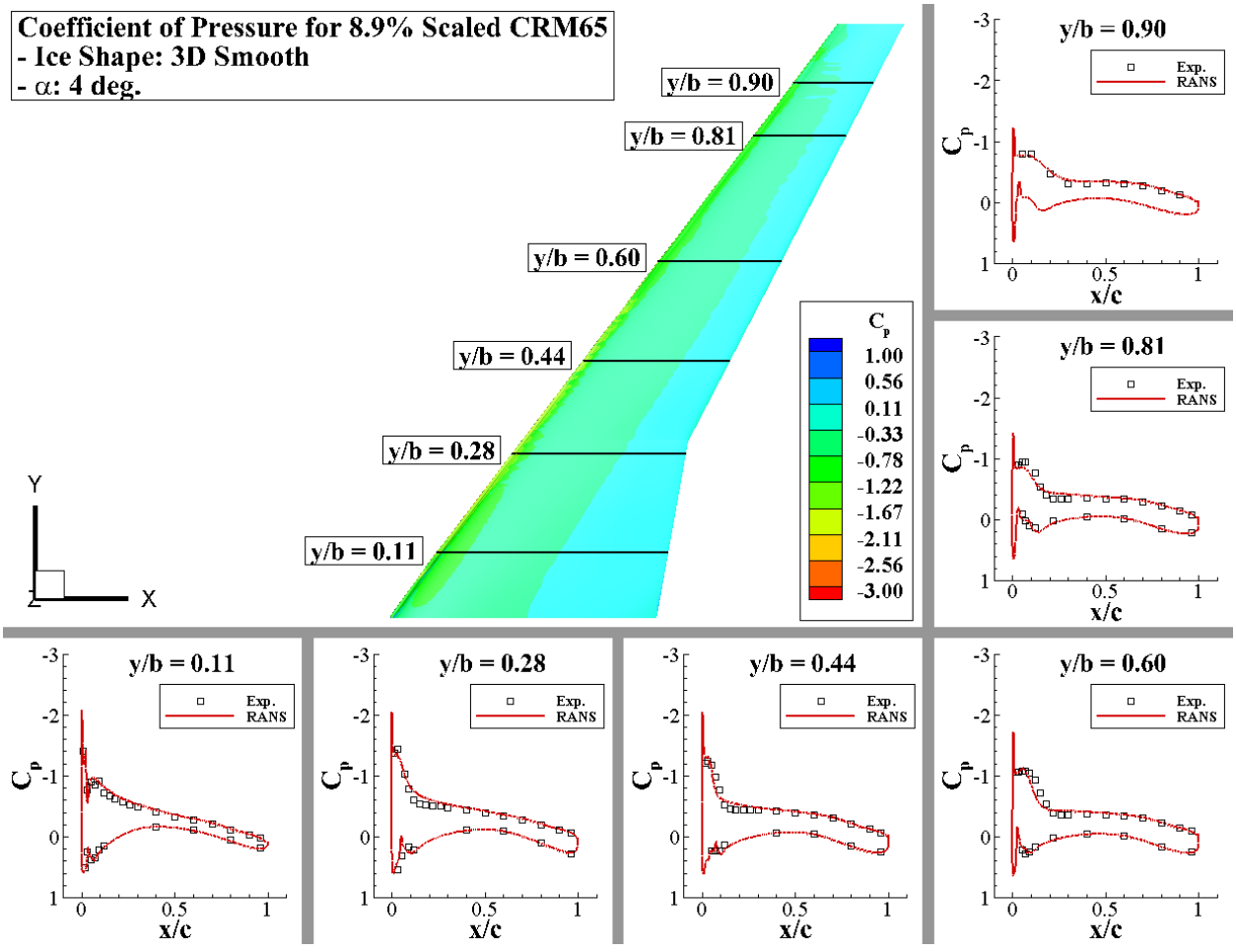

Fig. 3.11 Same as Fig. 10 except for addition of leading-edge ice shape.

Figures 3.12 and 3.13 show the pressure contour and pressure distribution for the clean and ice-shape wing respectively at an angle of attack of 6-degrees. Similar to the 4-deg. case, the clean wing at 6-deg. shows very little variation in the pressure contour along the span, while the iced wing does exhibit some variance. RANS accurately captures the coefficient of pressure at all of the spanwise locations for the clean wing as seen in Fig. 3.12. For the wing with the ice-shape as seen in Fig. 3.13, the pressure contours indicate that the leading-edge suction peak is strongest (indicated by red contours) inboard up to the Yehudi break (y/b = 0.28). While the magnitude of the spike of the suction peak can't be quantitatively confirmed by the experimental data, it is qualitatively similar to what is seen at other points across the span of the wing. Compared to the 4-deg. ice-shape case, the coefficient of pressure plateaus are more pronounced and extend further along the upper surface in the chordwise direction. This is consistent with a stronger leading-edge vortex and larger region of flow separation. In general, RANS accurately captures the coefficient of pressure in the inboard region and again near the tip (y/b = 0.11, 0.28, and 0.90). At y/b = 0.44, 0.60 and 0.81, RANS under-predicts the extent of the pressure plateaus, which is attributed to unpredicting the flow separation at these locations, consistent with differences observed in the oil flow visualization and the wall shear stress in Fig. 3.7.

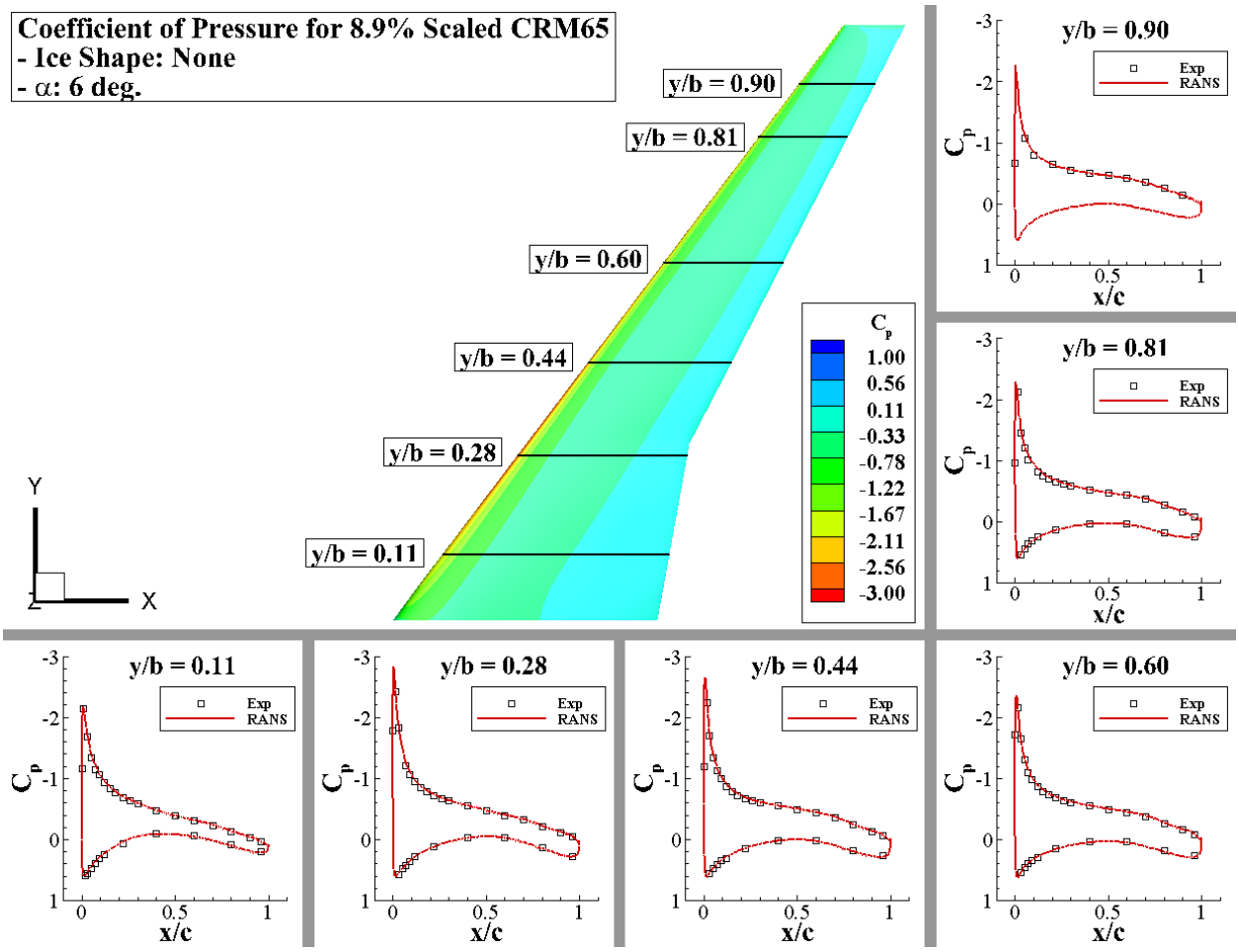

Fig. 3.12 Same as Fig. 3.10 except for 6-deg angle of attack.

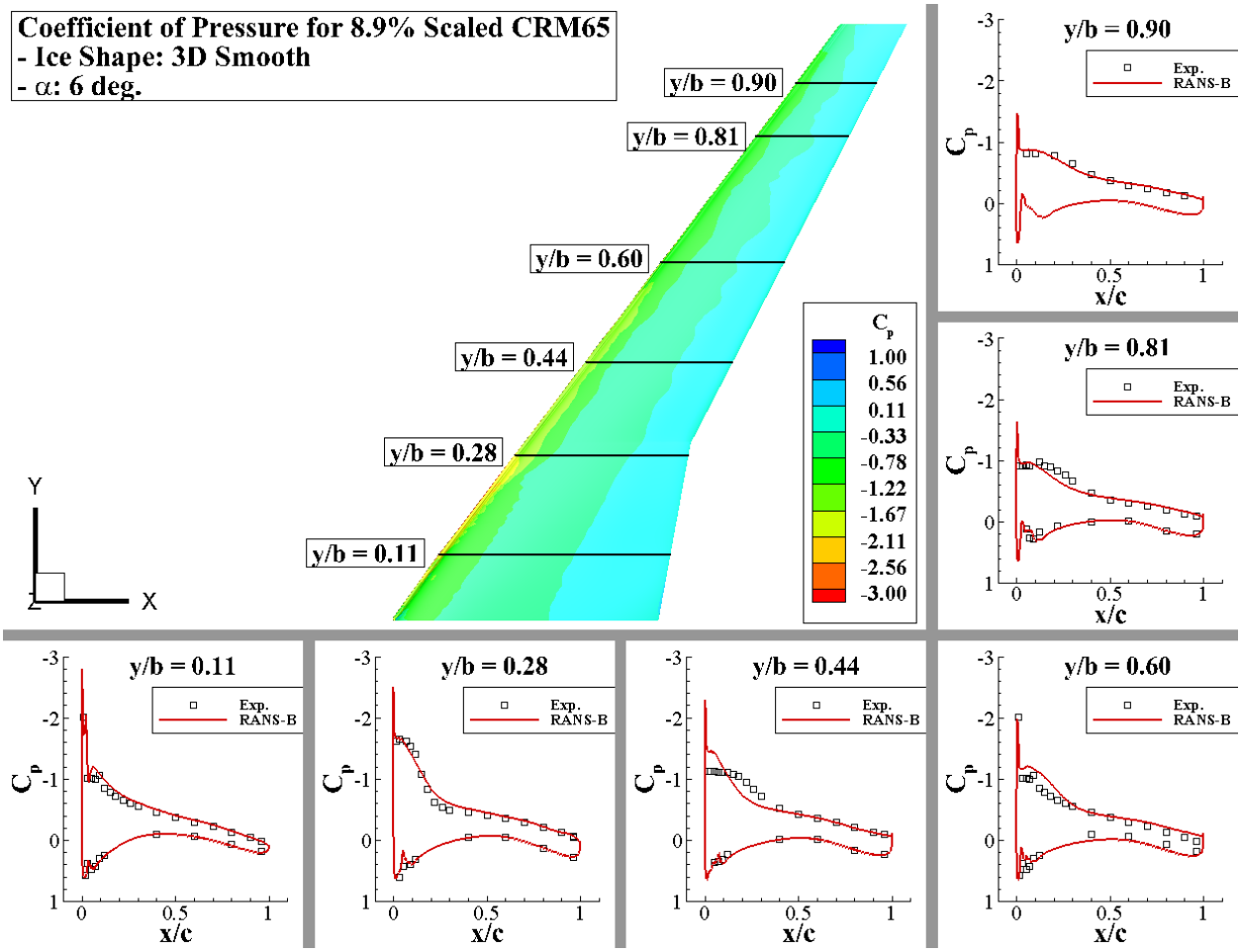

Fig. 3.13 Same as Fig. 3.10 except for 6-deg angle of attack and ice shape, where RANS predictions stem from baseline mesh (RANS- B)

Figures 3.14 and 3.15 show the pressure contour and pressure distribution for the clean and ice-shape wing respectively at an angle of attack of 8-deg. In contrast to both the 4-deg. and 6-deg. cases, the clean wing at 8-deg. exhibits a stronger spanwise variation in the pressure contour near the wing tip. In particular, there is a lower suction peak in the pressure distribution of both the experimental and RANS data at a spanwise location of $y/b = 0.90$ in Fig. 3.14, indicating onset of outboard stall for this clean configuration. In regards to predictive accuracy for this case with no ice shape, RANS is able to capture the overall pressure distribution. For the wing with an ice-shape at this angle of attack (Fig. 3.15), the pressure contours again indicate that the leading-edge suction peak is strongest (indicated by red contours) inboard up to the Yehudi break ($y/b = 0.28$). In the outboard region past $y/b = 0.44$, the wing is completely separated (similar to that observed in swept stall) and this is consistent with the flow separation shown in the oil flow visualization in Fig. 3.8. Despite this massive separation, RANS is remarkably able to capture the general trend of the pressure distribution. However, there are some discrepancies. At $y/b = 0.28$, the numerical methodology overpredicts the leading-edge suction peak, while the pressure plateaus are underpredicted in length for $y/b = 0.44$, 0.60, 0.81, and 0.90 indicating that the experimental separation is stronger than what was simulated. Also shown in this figure is a comparison between the baseline and refined grid cases. The differences between the two grids are small (generally less than 1%) so that the results can be considered nearly grid independent. However, the refined case

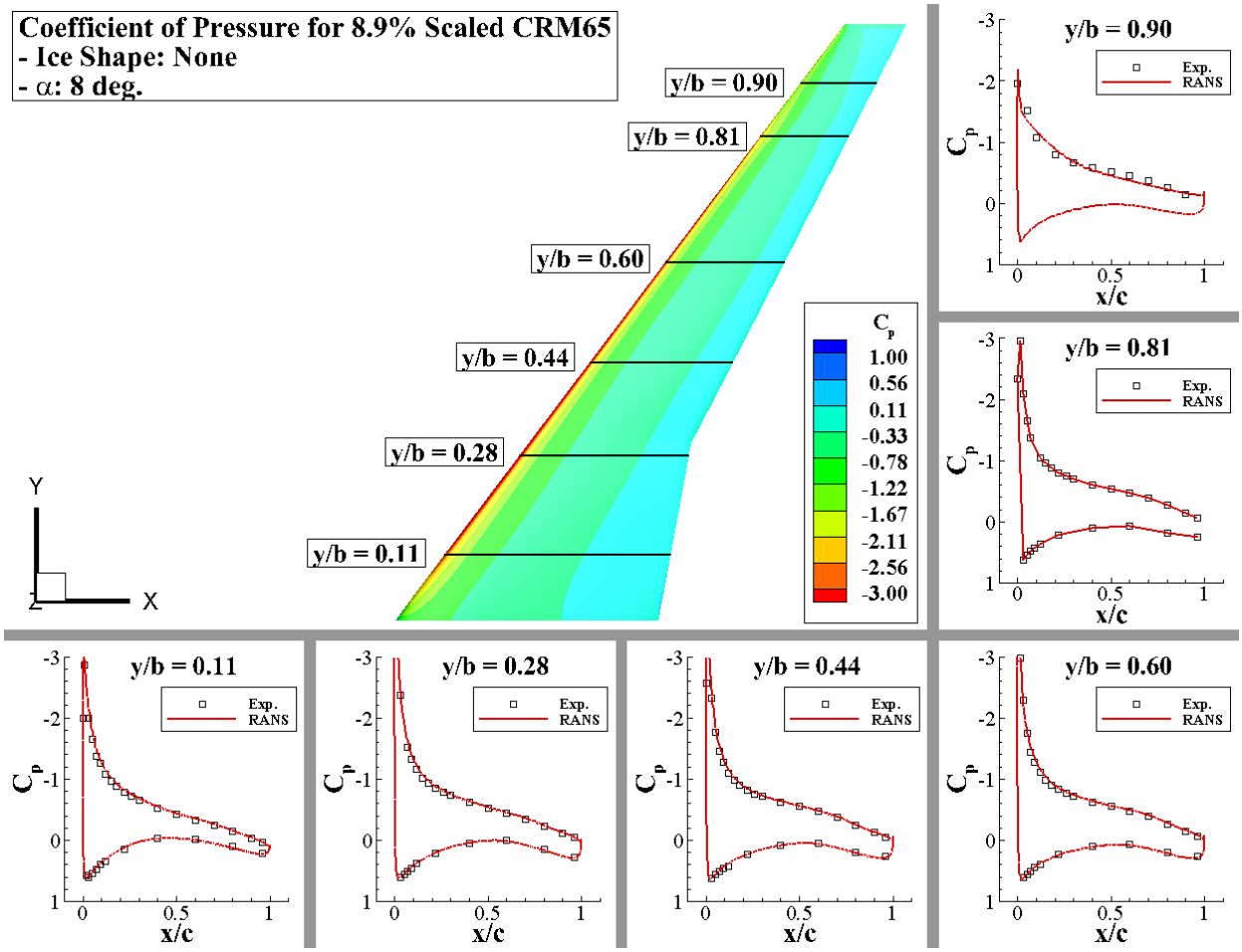

Fig. 3.14 Same as Fig. 3.10 except for 8-deg angle of attack

prediction of reattachment near the leading edge of the root of the wing aligns slightly better with the experimental data.

The pressure contour and distribution of the wing geometry with an ice shape at angle of attack of 10-deg. is shown in Fig. 16. The predicted pressure contours again indicate that the leading-edge suction peak (indicated by red contours) continues to be limited to the inboard region and tends to peak at y/b = 0.11. This is consistent with the story seen in the oil flow visualization whereby a large majority of the upper surface of the wing is stalling. While at y/b = 0.11 the flow is still attached, the separation aft of the ice shape near the Yehudi break has noticeably grown. Similar to the 8-deg. case, RANS is able to capture the general trend of this separation along the surface of the wing but underpredicts the extent of the pressure plateaus.

3.3 – Aerodynamic Coefficients

The aerodynamic coefficients are plotted in Figs. 3.17 and 3.18 for the clean wing and the wing with an ice shape respectively. When there is no ice shape, RANS was able to accurately capture the coefficient of lift in the linear region of the lift curve and the pitching moment as seen in Figs. 3.17a and 3.17b. However, RANS somewhat overpredicts the drag (by about 5%) at 8-deg. as seen on Fig. 3.17c. In general, this is in line with what is expected of the RANS accuracy for attached flow conditions and demonstrates that the clean configuration is well predicted up to 8-deg. As the

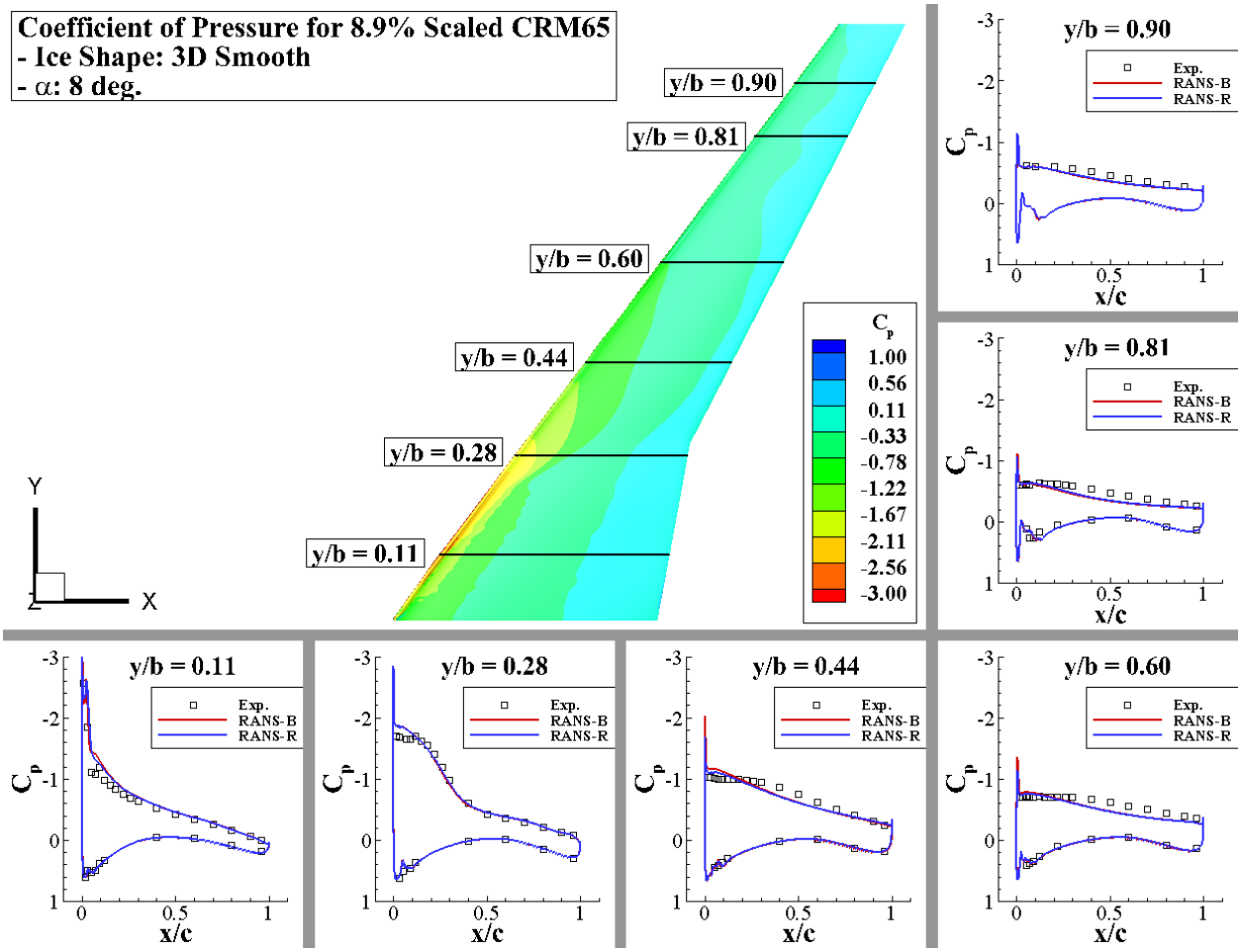

Fig. 3.15 Same as Fig. 3.10 except for 8-deg angle of attack and ice shape, showing RANS predictions from both baseline mesh (RANS- B) and refined mesh (RANS-R)

angle of attack increases and there are significant regions of separation, RANS tends to decrease in fidelity and is not able to fully predict the fluid dynamics, as can be seen in the other cases of this study and the coefficient of pressure plots referenced earlier.

As for the wing with an ice shape, Figs. 3.18a and 3.18b show that at angles of attack leading up to the sudden change in the pitching moment slope after 6-deg., RANS proves to be reasonable in predicting the coefficients for the complex geometry. In general, the experimental and computational data shows that the iced wing is still producing an increasing amount of lift as angle of attack increases. This is quite different than the C_L curve for the clean wing in Fig. 3.17, which shows a distinct max-C_L between αoa = 12 and 14 deg. As such, we cannot define a clear point of stall by definition for the iced swept wing. Also shown in this figure are the baseline and refined grid cases. The differences between the baseline and refined grids are small, generally less than 1%, which means that the results can be considered nearly grid-independent. As such, the shortfall of the RANS predictions at high angles of attack can be primarily attributed to the inherent limitations of the turbulence modeling for this highly complex three-dimensional flow, especially for highly separated conditions. However, the RANS performance for this swept icing wing flow is generally better than expected. considering RANS performance for non-swept wings with such ice accretion is generally not good [9].

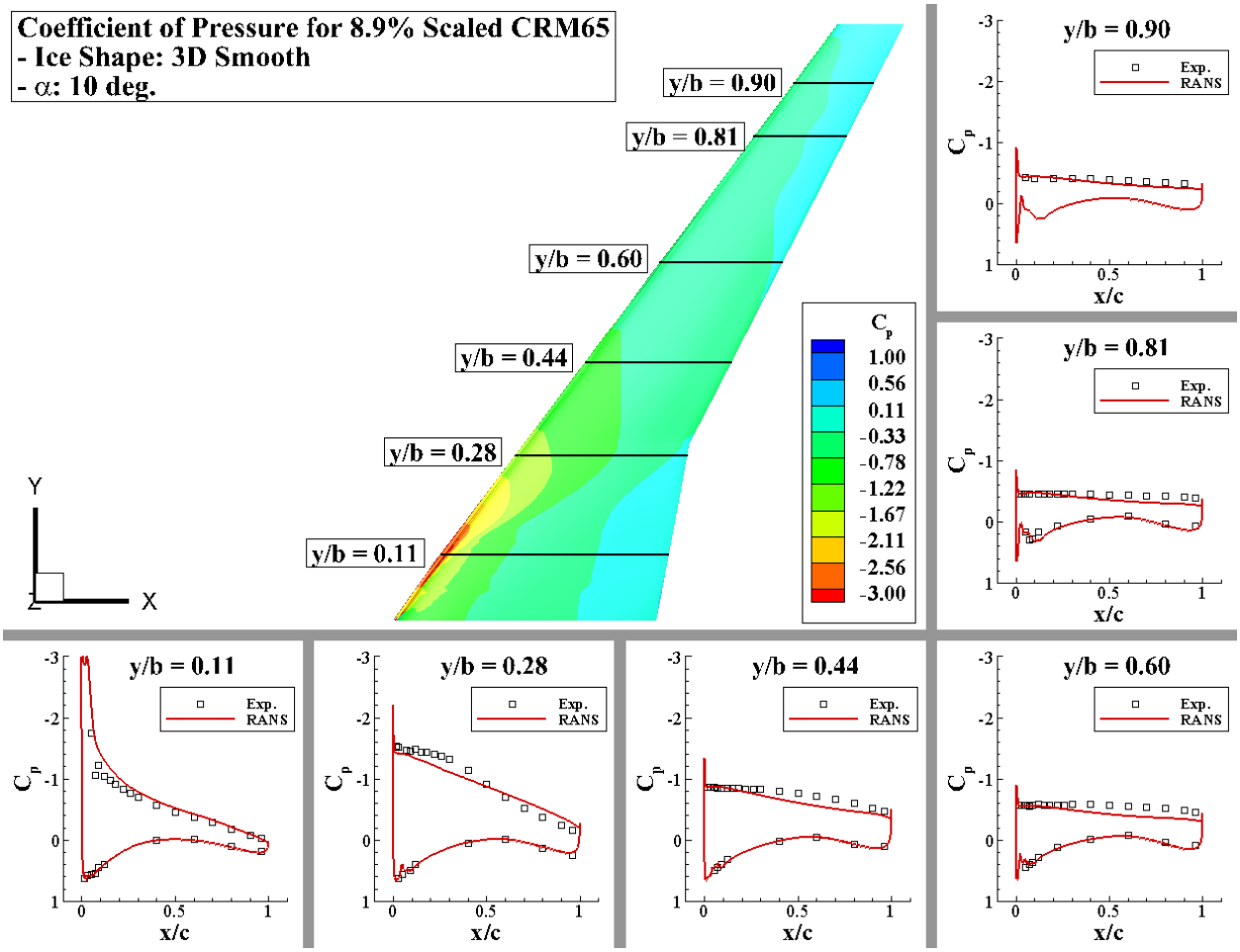

Fig. 3.16 Same as Fig. 3.10 except for 10-deg angle of attack and ice shape.

At angles of attack higher than 6-deg., RANS begins to slightly under-predict lift and significantly under-predicts the absolute value of the aerodynamic pitching moment. This discrepancy in the coefficient of pitching moment can be associated with the difference between the experimental and computational pressure distributions and the moment center, which is located such that it coincides with the leading edge of the wing near $y/b = 0.44$. Since RANS underpredicts the suction-side pressure distribution along majority of the chord for regions outboard of $y/b = 0.44$ (see Figs. 3.15 and 3.16), this results in a lower integrated portion of the lift force being applied downstream of the moment center, resulting in the lower coefficient of moment than the experimental data. Since the inboard region tends to have an over-prediction of the suction-side pressure values, this causes further discrepancies in the moment, but tends to reduce the discrepancies in the lift. In terms of drag prediction with an ice shape, there is again an underprediction at high angles of attack (like seen for the clean case), but this is rather modest considering the flow has such massive separation as seen in Figs. 3.8 and 3.9. Overall, RANS proved to be surprisingly capable of predicting the aerodynamics of an 8.9% scaled CRM65 wing, despite substantial outboard flow separation for the case with an ice shape.

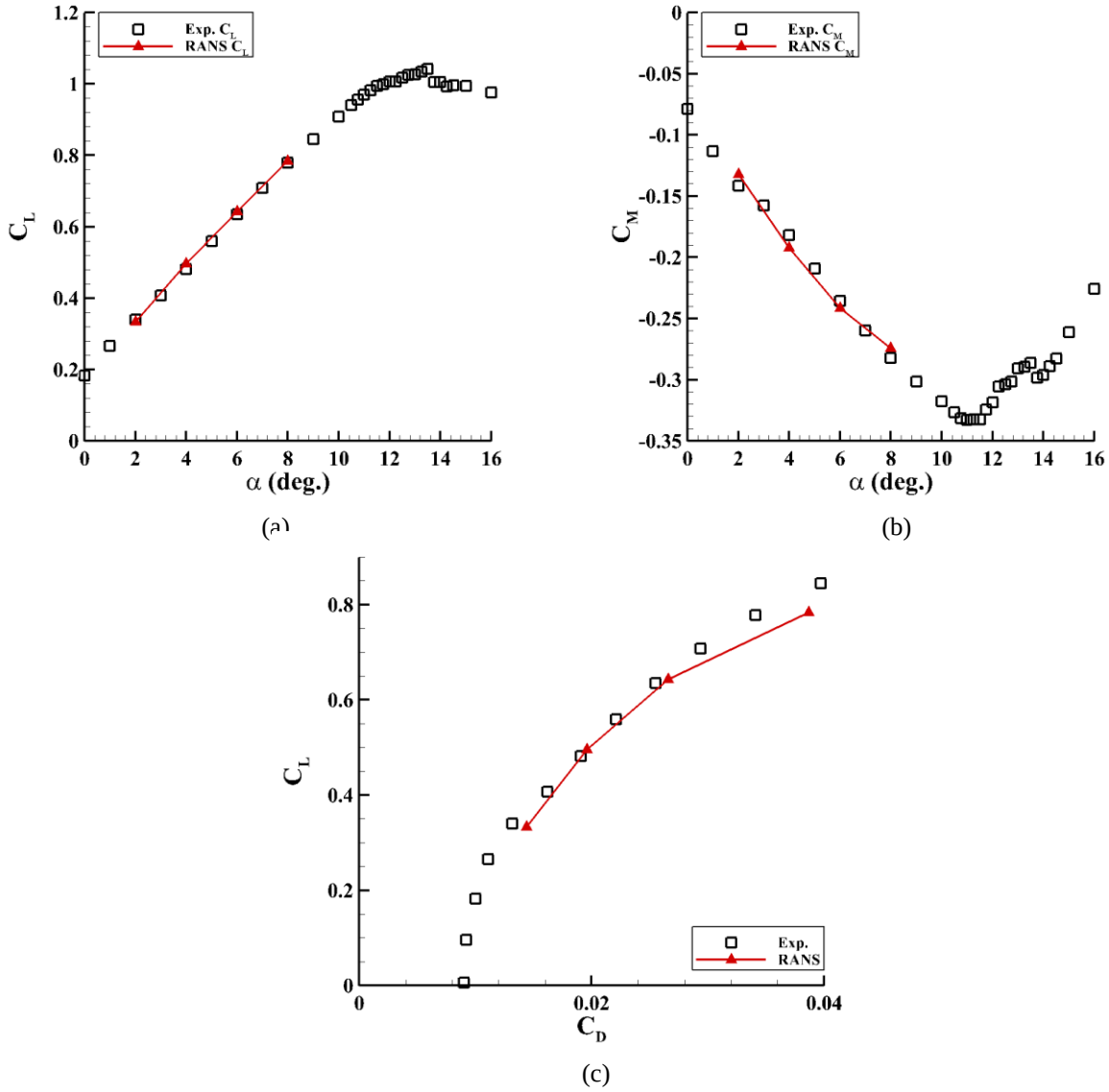

Fig. 3.17 Comparison of experimental and predicted for non-iced wing of: a) lift coefficient and b) moment coefficient vs. angle of attack and b) lift coefficient vs. drag coefficient.

4 – Conclusion

The aerodynamics of a swept-wing with leading edge ice accretion is not well understood due to the lack of publicly available experimental data, and the uncertainty as to whether RANS can predict the relevant aerodynamics. The objective of this study is to assess the ability of RANS *k-ω* SST to predict the flow physics and aerodynamic performance parameters for a Common Research Model swept-wing with and without an ice shape. The wing was modelled and simulated in a domain similar to the experimental tests conducted at the Wichita State University's Walter H. Beech Wind Tunnel. This experimental and computational work is herein reported to provide the community with more qualitative and quantitative information. As seen in the experimental and computational data, the flow around the 8.9% scaled CRM65 when there is a leading-edge ice shape, is highly complex and three-dimensional. In particular, as the angle of attack increases, the

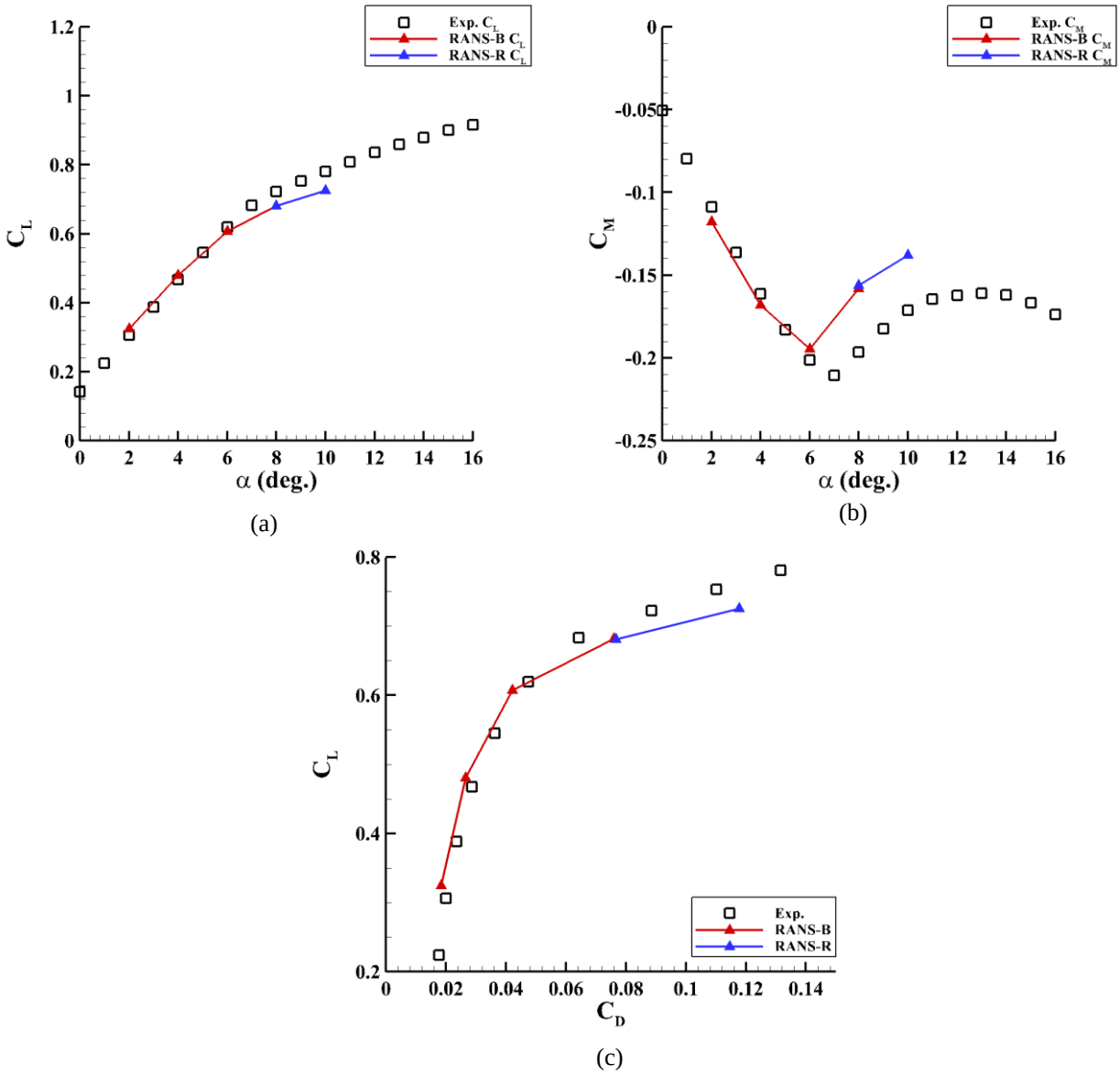

Fig. 3.18 Same as for Fig. 3.17 except for iced wing and with baseline (B) and refined (R) predictions.

separation starts from the outboard region and tends to grow in length in the chordwise direction. This separation is dominated by strong spanwise flow and differs significantly from the classic two-dimensional airfoil stall. When it first occurs (at 6-deg. angle of attack for present conditions with an ice shape), this stall is initially confined to a portion of the chord and generally outboard of the Yehudi break. However, at higher angles of attack, the entire region outboard of the Yehudi break is separated. In contrast, the clean wing shows very little evidence of separation up to 8-deg. angle of attack and has only weak spanwise variation in the pressure coefficient.

The RANS prediction for the swept-wing with an ice shape at 4-deg. angle of attack show a spanwise running vortex forms just aft of the leading-edge. This vortex grows in strength as the angle of attack increases. Qualitatively, RANS proved via wall shear stress data to be quite capable in accurately predicting the existence and strength of this vortex at 6, 8, and 10-deg. The prediction capability of RANS to capture general wing stall characteristics is also reflected in the pressure

distribution plots and the time-averaged aerodynamic coefficients. The prediction of the aerodynamic performance parameters for the clean and ice-shape geometries were reasonably resolved by the RANS solution. However, the absolute value of the coefficient of pitching moment at 8 and 10-deg. angle of attack, was underpredicted for the iced geometry and this can be associated with the difference between the experimental and computational pressure distributions.

Overall, the current (and conventional) RANS approach was surprisingly able to provide reasonable fidelity for this complex flow over a swept iced wing. This may be attributed to the three-dimensional effects which provided a strong spanwise flow component so that the separation was not like a typical bluff-body flow. However, more conditions would need to be considered before any general claims can be made. Recommendations for future work include the pursuit of three main objectives: 1) an improved understanding of the three-dimensional character of the spanwise running flow above the wing surface and its impact on iced swept-wing aerodynamics, 2) an improved understanding of the influence of the unsteady flow physics and its impact on flow separation stability and extent, 3) exploring improvement to RANS to improve the predicted accuracy of the pressure distribution along the swept-wing when separated due to leading edge ice, and 4) investigating the differences in flow physics and aerodynamics for the simplified ice shape (considered herein) vs. and an ice shape that captures the discrete details of ice shapes that have been observed experimentally.

Chapter 3 References

[1] Broeren, A. P., Potapczuk, M. G., Lee, S., Malone, A. M., Paul, B. P., and Woodard, B., "Ice-Accretion Test Results for Three Large-Scale Swept-Wing Models in the NASA Icing Research Tunnel," *8th AIAA Atmospheric and Space Environments*, AIAA 2016-3733, June 2016. https://doi.org/10.2514/6.2016-3733

[2] Fujiwara, G. E. C., Bragg, M. B., and Broeren, A. P., "Comparison of Computational and Experimental Ice Accretions of Large Swept Wings." *Journal of Aircraft*, Vol. 57, No. 2, 2020, pp. 342–359. https://doi.org/10.2514/1.C035631.

[3] Broeren, A. P., Potapczuk, M. G., Riley, J. T., Villedieu, P., Moëns, F., and Bragg, M. B., "Swept-Wing Ice Accretion Characterization and Aerodynamics," 5*th AIAA Atmospheric and Space Environments Conference*, AIAA 2013-2824, June 2013. https://doi.org/10.2514/6.2013-2824

[4] Camello, S. C., Bragg, M. B., and Lum, C. W., "Effect of Ice Shape Fidelity on Swept-Wing Aerodynamic Performance," *9th AIAA Atmospheric and Space Environments Conference*, AIAA 2017-4373, June 2017. https://doi.org/10.2514/6.2017-4373

[5] Zeppetelli, D., and Habashi, W. G., "In-Flight Icing Risk Management Through Computational Fluid Dynamics-Icing Analysis." *Journal of Aircraft*, Vol. 49, No. 2, 2012, pp. 611–621. https://doi.org/10.2514/1.C031609.

[6] Alam, M. F., Thompson, D. S., and Walters, D. K., "Hybrid Reynolds-Averaged Navier–Stokes/Large-Eddy Simulation Models for Flow Around an Iced Wing." *Journal of Aircraft*, Vol. 52, 2015. https://doi.org/10.2514/1.C032678.

[7] Zhang, Y., Habashi, W. G., and Khurram, R. A., "Zonal Detached-Eddy Simulation of Turbulent Unsteady Flow over Iced Airfoils." *Journal of Aircraft*, Vol. 53, 2016. https://doi.org/10.2514/1.C033253.

[8] Xiao, M., Zhang, Y., and Chen, H., "Numerical Study of an Iced Airfoil Based on Delayed Detached- Eddy Simulation with Low Dissipation Scheme," *9th AIAA Atmospheric and Space Environments Conference*, AIAA 20178-3761, 2017. https://doi.org/10.2514/6.2017-3761

[9] Stebbins, S. J., Loth, E., Broeren, A. P., and Potapczuk, M., "Review of Computational Methods for Aerodynamic Analysis of Iced Lifting Surfaces," *Progress in Aerospace Sciences*, Volume 111, 2019. https://doi.org/10.1016/j.paerosci.2019.100583.

[10] Liu, C., Liu, Z., and Sakell, L., "Comments on the Feasibility of LES for Wings, and on a Hybrid RANS/LES Approach," *Proceedings of the First AFGSR International Conference*

on DNS/LES. August 1997.

[11] Pan, J., and Loth, E., "Detached Eddy Simulations for Iced Airfoils." *Journal of Aircraft*, Vol. 42, No. 6, 2005. https://doi.org/10.2514/1.11860.

[12] Kwon, O. J., and Sankar, L. N., "Numerical Simulation of the Flow about a Swept Wing with Leading-Edge Ice Accretions." *Computers and Fluids*, Vol. 26, 1997, pp. 183–192. https://doi.org/10.1016/S0045-7930(96)00038-2.

[13] Vassberg, J., Dehaan, M., Rivers, M., and Wahls, R., "Development of a Common Research Model for Applied CFD Validation Studies," *26th AIAA Applied Aerodynamics Conference, AIAA 2008-6919*, August, 2008. https://doi.org/10.2514/6.2008-6919.

[14] Vassberg, J. C., DeHaan, M. A., Rivers, M. S., and Wahls, R. A., "Retrospective on the Common Research Model for Computational Fluid Dynamics Validation Studies." *Journal of Aircraft*, Vol. 55, No. 4, 2018, pp. 1325–1337. https://doi.org/10.2514/1.C034906.

[15] Broeren, A. P., Woodard, B., Diebold, J. M., and Moens, F., "Low-Reynolds Number Aerodynamics of an 8.9% Scale Semispan Swept Wing for Assessment of Icing Effects," *9th AIAA Atmospheric and Space Environments Conference*, AIAA 2017-4372, June 2017. https://doi.org/10.2514/6.2017-4372

[16] Harper, C. W., and Maki, R. L.. "A Review of the Stall Characteristics of Swept Wings," NASA TN D-2373, July 1964.

[17] Camello, S. C., Lee, S., Lum, C. W., and Bragg, M. B., " Generation of Fullspan Leading-Edge 3D Ice Shapes for Swept-Wing Aerodynamic Testing," *8th AIAA Atmospheric and Space Environments Conference*, AIAA 2016-3737, June 2016. https://doi.org/10.2514/6.2016-3737

[18] Wilcox, D. C., "Turbulence Modeling for CFD," DCW Industries, La Canada, CA, 1994.

[19] Menter, F. R. "Two-Equation Eddy-Viscosity Turbulence Models for Engineering Applications." *AIAA Journal*, Vol. 32, No. 8, 1994. https://doi.org/10.2514/3.12149.

[20] Munoz-Paniagua, J., García, J., and Lehugeur, B., "Evaluation of RANS, SAS and IDDES Models for the Simulation of the Flow around a High-Speed Train Subjected to Crosswind." *Journal of Wind Engineering and Industrial Aerodynamics*, Vol. 171, 2017. https://doi.org/10.1016/j.jweia.2017.09.006.

[21] Steinbrenner, J. P., "Construction of Prism and Hex Layers from Anisotropic Tetrahedra," *22nd AIAA Computational Fluid Dynamics Conference*, AIAA 2015-2296, June 2015. https://doi.org/10.2514/6.2015-2296

[22] Poll, D., “Spiral Vortex Flow Over a Swept-Back Wing.” *The Aeronautical Journal*, Vol. 90, No. 85, 1986, pp. 185–199. https://doi.org/10.1017/S0001924000015670

[23] Diebold, J. M., Broeren, A. P., and Bragg, M., "Aerodynamic Classification of Swept-Wing Ice Accretion," *5th AIAA Atmospheric and Space Environments Conference*, AIAA 2013-2825, June 2013. ttps://doi.org/10.2514/6.2013-2825

Chapter 4

Numerical Simulation of Iced Swept Wing Aerodynamics with RANS, DES, and IDDES

1 – Introduction

Aircraft ice accretion is a critical national safety issue, but one which is not well understood in terms of the three-dimensional aerodynamics for commercial aircraft wing geometries. One reason is that experimental data has not been previously available for modern geometry aircraft wings with realistic geometry ice shapes consistent with atmospheric icing conditions. To determine the appropriate ice shapes which can arise for such wings, experimental icing data was collected at the NASA Glenn Research Center Icing Research Tunnel (IRT) for a swept-wing icing project. In these experiments, ice shapes were accreted to the leading edge of a hybrid model that of a 65% scaled Common Research Model (CRM65) developed by Broeren *et al.* [1]. The resulting ice accretions reasonably matched the expected geometric complexity based on previous ice accretion testing for swept wings. These ice accretions were captured via laser scans and then digitized and manipulated to provide water-tight CAD models that could be used for 3D-printed sub-scaled ice shapes on the 8.9% scale model of the CRM65 [2]. Using such 3-D printed shapes, the second set of experiments was conducted in subsequent aerodynamic wind tunnel tests. These conditions found significant partial-span flow separation occurring starting at angles of attack as small as 6 degrees, whereby the associated fluid dynamics were highly complex and three-dimensional [3].

A review of the aerodynamics of iced wings by Stebbins *et al.* discussed research by Alam *et al.*, Zhang *et al.*, and Xiao *et al*. [4–7]. These sources highlighted that unsteady flow features and the associated fluctuating aerodynamic loads can adversely affect flight aerodynamics and thus, aircraft operation and safety. This underlying problem requires manufacturers to pursue icing certification, which represents a large potential cost due to the combination of wind tunnel tests and flight tests that can be involved. Zeppetelli *et al.* [8] have shown that Computational Fluid Dynamics (CFD) can help address this problem due to its ability to identify aerodynamic issues at the beginning/early phases of the design processes for an aircraft. With the advancement of numerical methodologies that can capture the flow structures relevant to iced aerodynamics, CFD has the potential to save significant costs in aircraft design and icing certification processes. However, for modern swept wings with leading-edge ice shapes, very little CFD has been completed so it is not clear as to which flow conditions lead to highly unsteady flow and which

methodologies can accurately predict the aerodynamics. Accuracy is a particular issue since computationally predicting such flows can be challenging due to the large regions of partial flow separation on a modern swept wing (which has high spanwise variation and spanwise flow, coupled with feature complexity and large unsteadiness). These conditions are not normally addressed with conventional turbulence modeling in Reynolds-Averaged Navier-Stokes approaches (RANS). The primary alternatives for high Reynolds number aerodynamic flows are generally based on the Detached Eddy Simulations (DES) method by Spalart [9]. DES is a hybrid coupling of Reynolds–Averaged Navier-Stokes (RANS) and Large Eddy Simulation (LES) techniques. The DES approach was first successfully applied to iced airfoils and simple wings (no sweep) by Pan *et al.* [10] with at least qualitative success. Recent studies by Butler *et al.* [11] employed Detached Eddy Simulations (DES) and Improved Delayed Detached Eddy Simulations (IDDES), where the latter advanced the computational robustness of the DES numerical method. However, extensive work completed by Saini *et al.* [12] has shown that the success of these HRL methods is susceptible to their ability to predict the dynamics in the "grey area". This grey area is the intermediate location at which the numerical model transition from unsteady RANS to the scale-resolving mode of LES. Furthermore, DES, IDDES, and other hybrid techniques have not been previously examined for a swept wing (that is consistent with modern commercial aircraft wings) with three-dimensional leading-edge ice shapes (that are consistent with experimentally observed ice accretions). This is an important issue to address since the application and assessment of DES and IDDES for these aerodynamic flows can be very useful for researchers to determine "which tool is best for the job". Thus, the present study is a part of a larger overall initiative to understand iced wing aerodynamics by a consortium of organizations including NASA, the Federal Aviation Administration (FAA), the Office National d'Etudes et Recherches Aérospatiales (ONERA), Boeing, the University of Illinois, the University of Virginia, and the University of Washington.

The goal of this particular study is to explore the fidelity and robustness of DES and IDDES compared to RANS for a CRM65 wing with a leading-edge ice shape at various moderate angles of attack. To the authors' knowledge, no previous work has analyzed the ability of DES and IDDES (or other hybrid turbulence approaches) to predict the complexity of a flow field that is semi-detached (i.e., neither fully attached nor fully detached/separated) for an iced swept wing.

2 – Computational Domain & Methodology

2.1 – Problem Description

An 8.9% scale version of the semi-span swept CRM65 wing is studied in this paper consistent with the work done by Stebbins *et al.* [13] The CRM65 wing is based upon the Common Research Model (CRM) developed by Vassberg *et al.* [14] to help fulfill the need to have a contemporary experimental database that can directly support the validation of various applications of CFD (e.g., simulating ice accretion, validating turbulence models, etc.) and was comparable in design to modern-day commercial airplanes. The CRM65 65% scale version of the CRM is comparable to a variety of large commercial aircraft (e.g., Airbus A320 and Boeing 737-800). This size was picked based on the balance of relevancy for large and intermediate aircraft, as well as tunnel size restrictions for NASA's IRT [1]. An 8.9% scale of the CRM65 was employed for aerodynamic testing in the Wichita State University (WSU) Walter H. Beech Wind Tunnel, as seen in Fig. 4.1.

The key features for this wing include a span of 1.524 m, a mean aerodynamic chord (MAC) of 0.4234 m, a taper ratio of 0.23, and a leading-edge sweep angle of 37.2 deg [15].

In terms of geometry, the present computational domain was developed with a cross-section that matches the aforementioned WSU wind tunnel. The corner chamfers of the wind tunnel, which can be seen in Fig. 4.1, were not included in the computational domain. Similarly, this study did not model the streamlined shroud used in the experiments, but the 6.23 cm gap between the bottom of the wing geometry and the floor was included. The computational domain set the outflow boundary condition at a location of 30·MAC downstream, and the inflow boundary condition at 10·MAC upstream from the center of rotation. The present study modeled all of the walls of the wind tunnel to utilize the uncorrected aerodynamic data collected during the experimental tests. The final computational domain measured 2.134 m high by 3.048 m wide by 19.68 m long and is the same as the one employed by Stebbins *et al.* [13]. The ice shape for the 8.9% scaled CRM65 wing can be seen in Fig. 4.1 and was developed by simplifying the spanwise variation in the highly three-dimensional ice shapes by interpolating along the span via user-defined splines that replicated the major cross-sectional ice features in 2.54 cm increments.

In terms of flow conditions, the overall properties of the present computational study were selected to match the experimental setup of Broeren *et al.* [15] and Camello *et al.* [3]. These studies collected data via force balance measurements, surface pressure taps, oil flow visualizations, mini tufts, and wake surveys at a Reynolds number of $1.8 \cdot 10^6$ and a Mach number of 0.18 in the WSU wind tunnel. Computationally, a velocity boundary condition was assigned to the inlet, while a pressure outlet boundary condition was assigned to the outlet. Finally, the angles of attack for this study were selected among those measured experimentally, focusing on those that yield significant partial flow separation, for which the nonlinear aerodynamics are most important. These conditions were critical in determining the extent to which DES and IDDES could sufficiently predict an unsteady and semi-detached flow field, and overall aerodynamic characteristics.

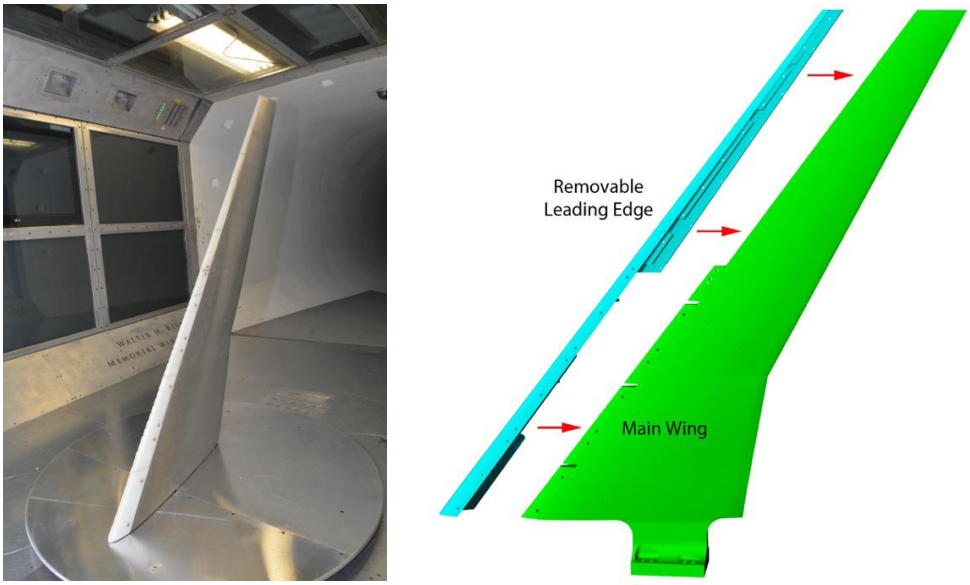

(a) (b)

Fig. 4.1 a) Wind tunnel installation of 8.9% scaled CRM65 with removable leading edge and b) original CAD model [3].

2.2 – Numerical Methodologies

Turbulent unsteady flow can be characterized by eddies with different lengths and time scales. Theoretically, one can resolve the whole spectrum of turbulent scales using DNS without modeling turbulence. However, for most engineering applications, the numerical cost is prohibitive, especially for high Reynolds number conditions [16]. Therefore, another approach to solving the Navier-Stokes equations is to use a length scale filter that filters out eddies smaller than either the determined length scale or the mesh grid spacing. Since the equations obtained by the filter process are governed by the dynamics of large eddies, this approach is called Large Eddy Simulation (LES). The LES method solves the large eddies directly (three-dimensional unsteady aspects) while the small eddies are modeled (with sub-grid scale turbulence modeling). The large eddies are typically comparable in size to the characteristic integral length scales of the turbulent flow, while the small eddies are responsible for the dissipation of the turbulence kinetic energy. Thus, the filter needs to be chosen carefully. While not as intensive as DNS, one of the main weaknesses of LES is its high requirement for memory allocation, or RAM, and CPU run times that are orders of magnitudes higher when compared to RANS calculation. This is because LES requires substantially finer meshes than the meshes typically used for RANS. To obtain stable statistics of the flow being modeled, problems utilizing LES must integrate over longer periods. Unlike RANS, to properly resolve all the turbulent length scales, the LES gridding near the wall needs to be well resolved in both the normal and parallel directions. This sometimes is neither achievable nor affordable, especially when the Reynolds number is large, and the flow is massively separated. Thus, the Wall-Modelled LES (WMLES) model was developed to activate RANS turbulence models in the inner part of the logarithmic layer while the outer part of the boundary layer uses a modified LES formulation. However, even with WMLES, LES is not currently practical for the full-scale aerodynamics of an aircraft wind, like the CRM65.

To avoid the high CPU requirements for a pure LES approach at high aerodynamic Reynolds numbers, the Detached Eddy Simulation (DES) approach was created by Spalart [9] to combine the LES and RANS approaches practically. In the DES model, which is referred to as a Hybrid RANS/LES (HRL) model, RANS is employed in the attached boundary layer regions, while the LES treatment is applied to the free shear and separated regions. This hybrid approach with LES and RANS is aimed to address both the high computational cost of a pure LES numerical method and the weakness of RANS to handle massive flow separations.

All HRL methods (e.g., DES and IDDES) require a transition from resolving the flow field using RANS to LES. To achieve this, the flow is generally divided into three main regions that reflect this transition: Unsteady-RANS (URANS) region, the grey area region (where there is a transition from RANS to LES), and Scale Resolved region which is modeled with an LES type of approach [12]. As outlined by Saini *et al.* [12], the predictive capability of IDDES has a large dependency on both the mesh refinement as well as the underlying RANS model. Furthermore, both of these dependencies affect the size of the "grey area" and can have a non-negligible effect on the final results. The "grey area" itself is defined where $0 < \tilde{f}_d < 1$. At $\tilde{f}_d = 1$, the numerical method is behaving in the URANS mode, and at $\tilde{f}_d = 0$, the numerical method is behaving in a scale resolving (e.g., LES) mode. In terms of fluid dynamics across an aerodynamic shape, this transition region is important as it helps bridge the gap between flow fields with very minor separation to flow fields with major separation (e.g., swept wing at low angles of attack vs. moderate angles of attack vs. high angles of attack). Further details and implications of the grey area can be found in Saini *et al.* [12].

In the current study, DES and IDDES methods are employed. Two of the most significant practical issues with the DES approach are "Modeled-Stress Depletion" (MSD) and "Grid-Induced Separation" (GIS) [9]. Another common issue with the DES and other WMLES methods is the "Logarithmic-Layer Mismatch" (LLM). To resolve these issues, the Delayed DES (DDES) was introduced to detect boundary layers and help delay the early onset of separation [17]. Furthermore, an Improved Delayed DES (IDDES) approach was developed to resolve LLM and MSD [18]. This model is also designed to prevent GIS and allow LES modeling of wall boundary layers. In the IDDES method, a sub-grid length scale is defined to represent not only the local characteristics of the grid but also the wall distance. It tends to depress this sub-grid scale and give it a steep variation, which subsequently stimulates instabilities and boosts the resolved Reynolds stress. In addition to addressing LLM, several components of IDDES include new empirical functions. The IDDES approach implemented herein modifies the transport equation of the turbulent kinetic energy (the equation of specific dissipation rate remains unmodified) as:

$$\frac{\partial(\rho k)}{\partial t} + \frac{\partial(\rho k u_i)}{\partial x_i} = \frac{\partial}{\partial x_j}\left[(\mu + \sigma_{k3}\mu_t)\frac{\partial k}{\partial x_j}\right] + G_k - Y_k \cdot F_{IDDES} \tag{4.1}$$

In the above equation, k is the turbulent kinetic energy, ρ is the density, u is the fluid mean velocity, and the terms for turbulent kinetic energy generation (G_k) and distraction (Y_k) are described in Menter [19]. F_{IDDES} is a new length scale defined for the IDDES formulation and is based on both the RANS turbulent length scale, the LES grid length scale, and the wall distance. Details can be found in Shur *et al.* [18] and IDDES is now a highly common hybrid approach for aerodynamics with large flow separation [20].

For the present study, IDDES was the main numerical method tested at angles of attack of 6, 8, and 10-deg. for the aerodynamics of an iced CRM65. However, DES was also tested at an angle of attack of 10-deg. to provide a brief comparison of the two methodologies which have different grey area treatments. In addition, both methods were compared to a conventional RANS approach, since this is the industry standard for aircraft design. The underlying RANS model used for DES and IDDES in this study is k-ω SST. This is consistent with the work completed by Stebbins et al. [13] for the same geometry. To employ these models, the commercial code ANSYS Fluent was used for all simulations and the settings are consistent with the work presented by Butler *et al.* [11]. After running the cases to convergence using RANS, the simulations continued solving with the respective IDDES and DES methods using a dual-time stepping approach with an implicit scheme. The time step (Δt) chosen was 0.0005 sec. to satisfy an accuracy condition (to capture unsteadiness of the large-scale structures) of $\Delta t < 0.1c/U_\infty$, where c is the MAC of the wing and U_∞ is the freestream velocity (62.1 m/s).

2.3 – Meshing Technique

The meshes for this study were generated using the anisotropic tetrahedral extrusion method (T-Rex) to create unstructured boundary layer meshes [21]. As seen in Fig. 3.2, the mesh is initiated by defining the surface of the model. For this study, it was deemed the most appropriate to use an unstructured grid for the surface to best mesh the swept wing as it helps captures the complexity of the surface topology as defined by the ice shape. Once the surface mesh has been defined, the volume mesh is grown from the surface using an appropriate Δs and growth rate. For this study, an initial cell height of 6.452 μm was used to ensure an appropriate $y+$ value equal to

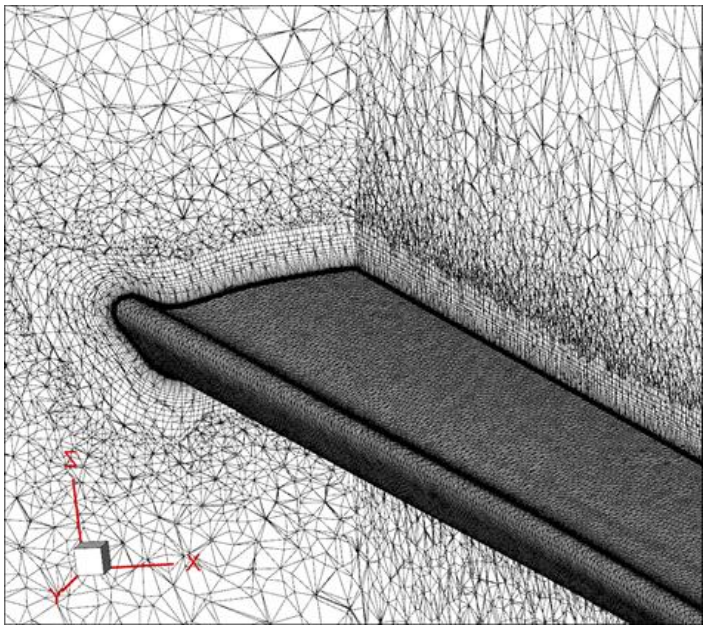

(a)

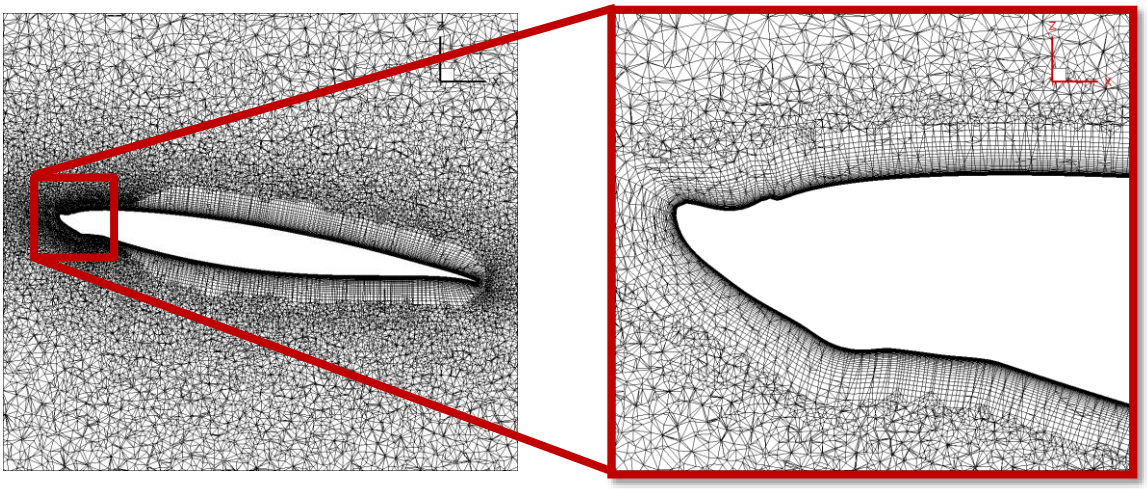

(b)

Fig. 4.2 a) Orthogonal cross-sectional view and b) cross-sectional view in the X-Z plane at *y/b* = 0.28 of the mesh generated for the iced wing. [13]

approximately 1, and the growth rate was chosen to be 15% with a cap of 50 max layers. The baseline surface mesh cells were isotropic and had an average edge length of 2.13 mm. Fig 4.2a provides an orthogonal view of the mesh with cuts in both the spanwise and chordwise directions. These cuts showcase the hybrid mesh of the domain where the T-Rex was grown from the surface using hexahedral and switched to tetrahedral in the domain discretizing the region beyond the boundary layer mesh. Fig. 4.2b provides a zoomed-in diagram of the chordwise cut of the mesh at a *y/b* = 0.28.

As in Stebbins *et al.* [13], two grids were used to analyze the fluid dynamics at an angle of attack of 8-deg. The baseline mesh was refined along the upper surface of the wing to achieve further discretization of the region just aft of the leading-edge ice shape by reducing the cell edge length in this region was reduced from 1.27 mm to 0.914 mm. The far-field was also refined near the geometry by reducing the max cell edge length from 5.08 cm to 2.54 cm. While the baseline mesh is composed of $28.1 \cdot 10^6$ nodes and $70.2 \cdot 10^6$ cells, the refined mesh presented in this study for comparison is composed of $36.0 \cdot 10^6$ nodes and $101.0 \cdot 10^6$ cells. As discussed by Stebbins *et al.* [22] in their wake refinement study, it was deemed unnecessary to add high refinement aft of the wing's trailing edge. The baseline mesh was used for the cases at an angle of attack of 6 and 8-deg., while the refined mesh was used for the cases at an angle of attack of 8 and 10-deg.

3 – Results

The following section discusses the comparison of hybrid DES and IDDES predictions compared to experiments for the aerodynamics of an 8.9% CRM65 wing with a leading-edge ice shape. This includes flow field visualizations, surface pressure distributions, and time-averaged aerodynamic coefficients. Additionally, the analysis compares against Stebbins *et al.*'s [13] work using RANS for the same configuration and flow field conditions.

3.1 – Flow Field Visualization

To characterize the instantaneous flow complexity captured by DES and IDDES, flow visualization was applied using three-dimensional surface contour maps. Chakraborty *et al.* [23] have shown that there are several schemes available to identify vortices in the field. Some of these schemes include the Q-criterion [24], the λ_2-criterion [25], and the Δ-criterion [26]. Of the schemes mentioned, the Q-criterion has been used most frequently in recent studies and is defined as the following:

$$Q = \frac{1}{2}\left(tr\left(\Lambda_{ij}\right)^2 - tr\left(\Lambda_{ij}{}^2\right)\right) = \frac{1}{2}\|\bar{\Omega}\|^2 - \|\bar{S}\|^2 \tag{4.2}$$

where Λ is the velocity gradient tensor, S and Ω are the symmetric and antisymmetric components of the velocity gradient tensor. When $Q > 0$, the flow is largely dominated by fluid rotation or vorticity. When $Q < 0$, the flow is dominated by viscous stresses.

To utilize the Q-criterion, it is necessary to pick an appropriate value for a given problem that will sufficiently capture the desired level of observable turbulence. Too low of a value will produce a visual that is saturated with flow field information, while too high of a value will produce a visual that showcases minimum turbulent structures. After examining a range of Q-criterion values for the present flow fields to best capture the separated turbulent flow features, Q-criterion isosurfaces were set based on $Q(c/U_\infty)^2 = 100$, where c is the MAC of the wing and U_∞ is the freestream velocity. In this study, Figures 4.3 to 4.5 compare the turbulent structures present in the flow field at different angles of attack by using this scheme. At an angle of attack of 6-deg., Fig 4.3 shows the Q-criterion highlighting streaks of vortical features emanating from a leading-edge spanwise-running separated region (bound vortex), originating near the root of the wing. These streaks become more complicated (with larger structures) and more frequent towards the tip, indicating high three-dimensionality.

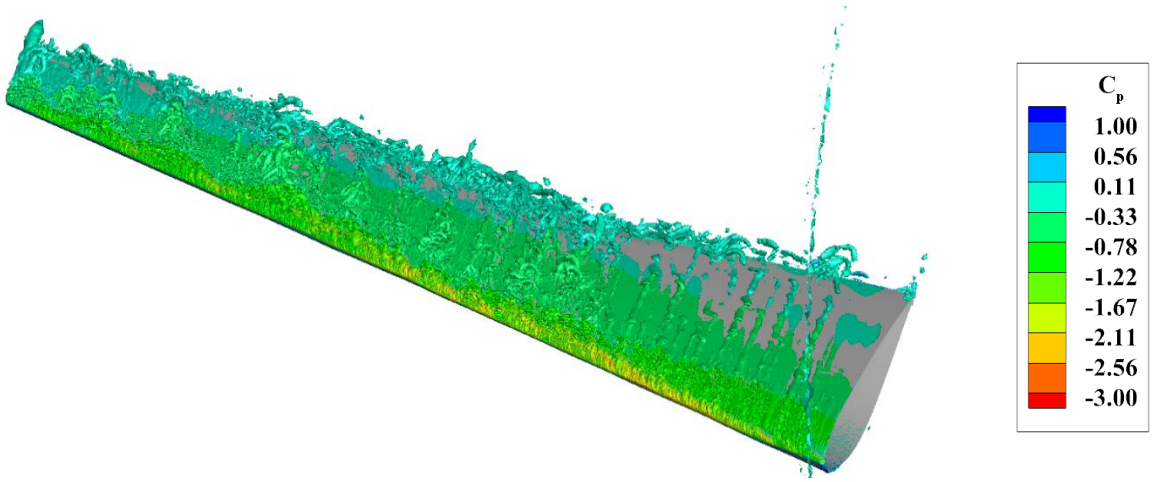

Fig. 4.3 Iso-surface defined by *Q*-criterion and colored by the coefficient of pressure for an instantaneous flow realization at an angle of attack of 6-deg. using the baseline mesh. [20]

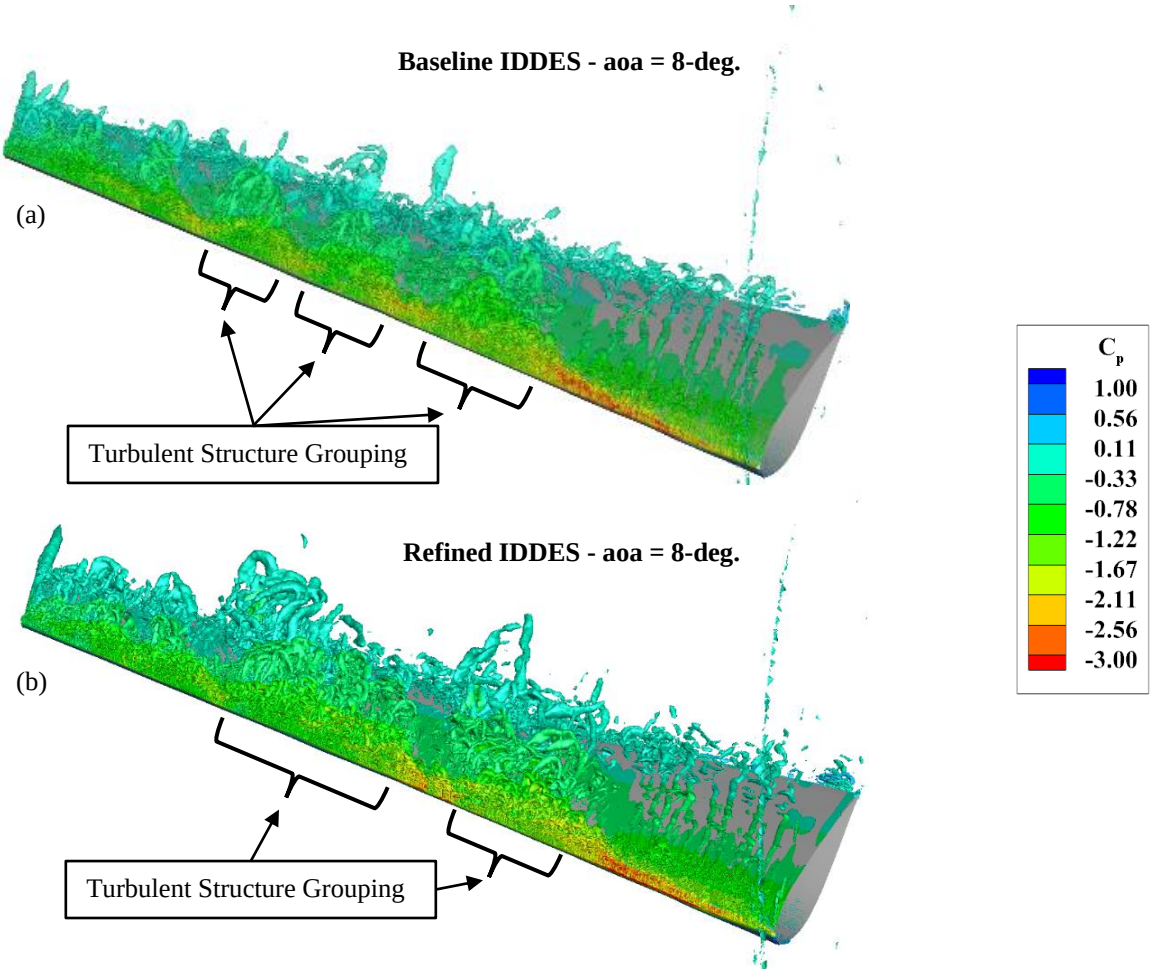

Fig. 4.4 Iso-surface defined by *Q*-criterion and colored by the coefficient of pressure for an instantaneous flow realization at an angle of attack of 8-deg. using a) the baseline mesh and b) the refined mesh. [20]

As the angle of attack increases to 8-deg., as shown in Fig. 4.4, the turbulent structures in the flow field are more prevalent across the span of the wing. This behavior is consistent with Brown *et al.*'s [27] data, which found the size (e.g. diameter) of the turbulent structures depicted by *Q*-criterion isosurfaces to grow with increasing angle of attack. Comparing the baseline mesh to the refined mesh, there are clear differences in the development of the flow over the wing as well as the size and grouping of the turbulent structures. In the baseline mesh, there are breaks between the turbulent structure groupings where the coefficient of pressure increases in magnitude and causes a localized low-pressure region. In contrast, there are fewer breaks amongst the turbulent structures when using the refined mesh. Additionally, the groupings of turbulent structures are more pronounced in size and extent along the chordwise and streamwise direction of the wing for the refined mesh case.

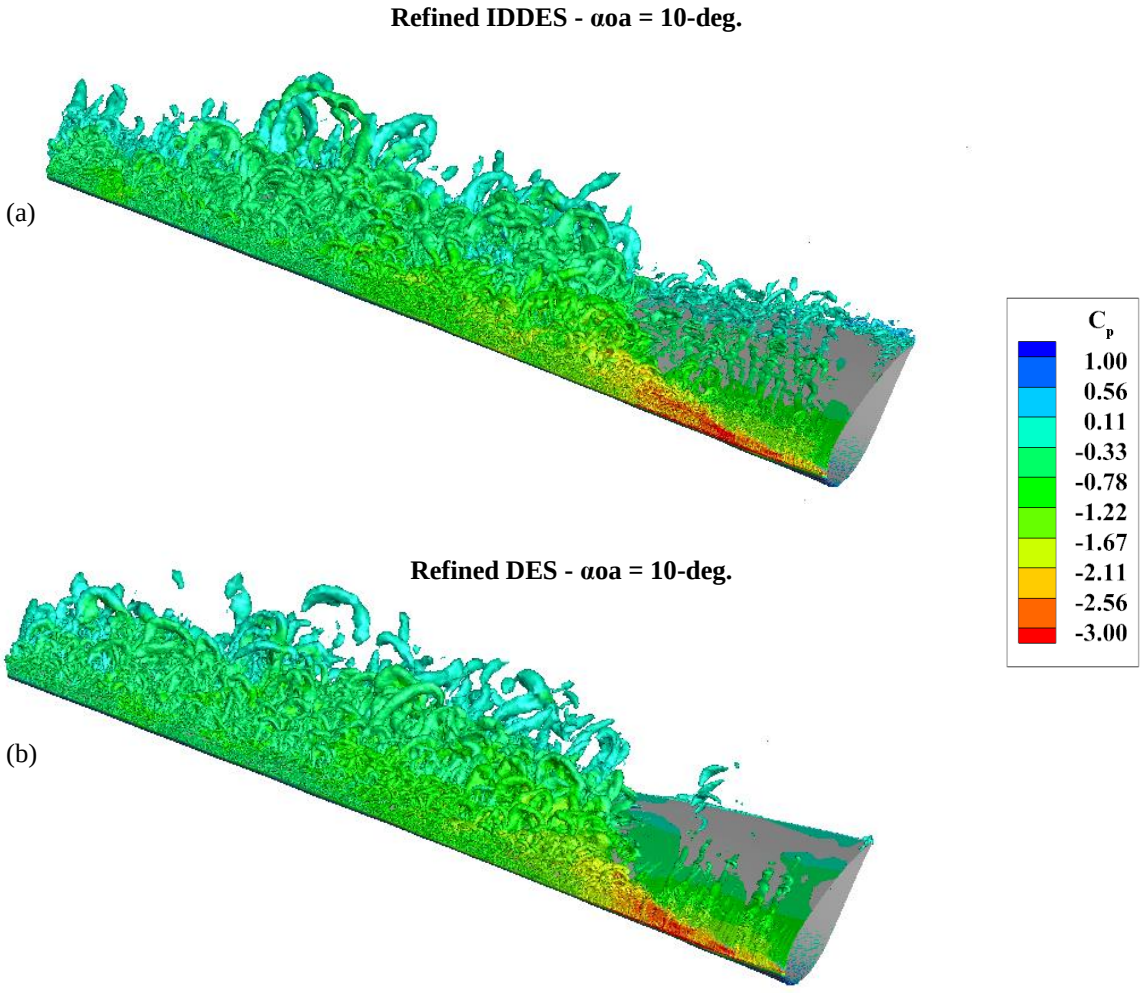

Fig. 4.5 Iso-surface defined by *Q*-criterion and colored by the coefficient of pressure for an instantaneous flow realization at an angle of attack of 10-deg. using the refined mesh for a) IDDES and b) DES.

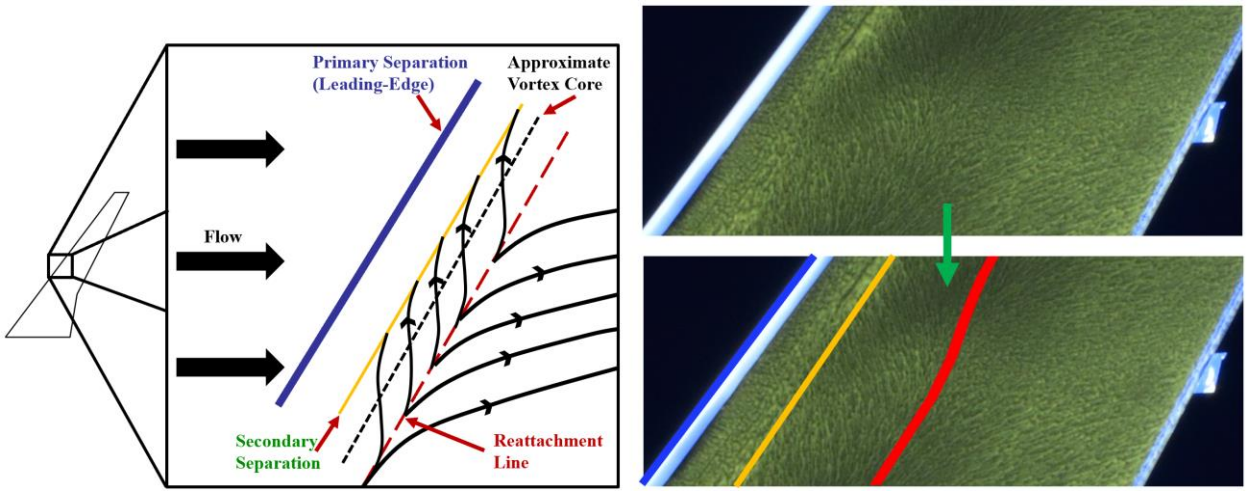

Fig. 4.6 Schematic and oil flow visualization example of surface streamlines caused by flow separating at the leading edge. Based on Poll [28].

Comparing the angle of attack of the 8-deg. case to the 10-deg. case in Fig. 4.5, the distinct groupings of turbulent structures visible at 8-deg. have largely disappeared at the higher angle of attack. Both the IDDES and DES cases at this angle of attack show very similar flow field behavior with only minimal discrepancies. DES was chosen only near the root of the wing, while the spanwise running vortex is still present aft of the leading edge and the magnitude of the low-pressure region has grown, the flow remains largely attached to the upper surface of the wing. One of the larger differences between DES and IDDES for these figures is the presence of relatively small turbulent structures near the root of the wing. Comparing the inboard section to the outboard section, the predicted turbulent structures in the flow field have significantly grown in size and extent over both the span and chord of the wing.

The experiments conducted by Broeren *et al.* [1] included the collection of both mini tufts and oil flow visualization data. This information helps visually identify locations of attached and separated flow along the surface of the wing. An in-depth analysis and method were provided by Poll [27] to support the interpretation of oil flow visualization results to understand near-wall flow field behavior. This method was subsequently applied by Stebbins *et al.* [13] to understand the computationally calculated wall shear stress via RANS and is reflected in the diagram shown in Fig. 4.6. For a swept wing with a leading-edge ice shape at low to moderate angles of attacks, two major forms of turbulent flow can be observed using the near wall fluid dynamics visualization technique. The first is a vortex just aft of the leading edge that runs from the root of the wing to the tip. The second is a separation region that initiates just aft of the primary vortex and is composed of a separation line, vortex core, and reattachment line. In Figures 4.7 to 4.9, the reattachment line is represented by a white line.

Figure 4.7 compares mini-tuft, oil flow visualization, and wall shear stress for the iced swept wing at an angle of attack of 6-deg. Comparing the mini-tuft data in Fig. 4.7a to the oil flow visualization data in Fig. 4.7b, flow separation can be defined by the tufts pointing in a direction that is significantly non-parallel to the flow direction (e.g., pointing in the spanwise direction or towards the leading edge). Figure 4.7c shows that the RANS predicted wall shear stress shows good agreement with the experimental data with regard to the areas of separate and attached flow as denoted by the white line. Fig. 4.7d shows that the time-averaged IDDES flow field does not

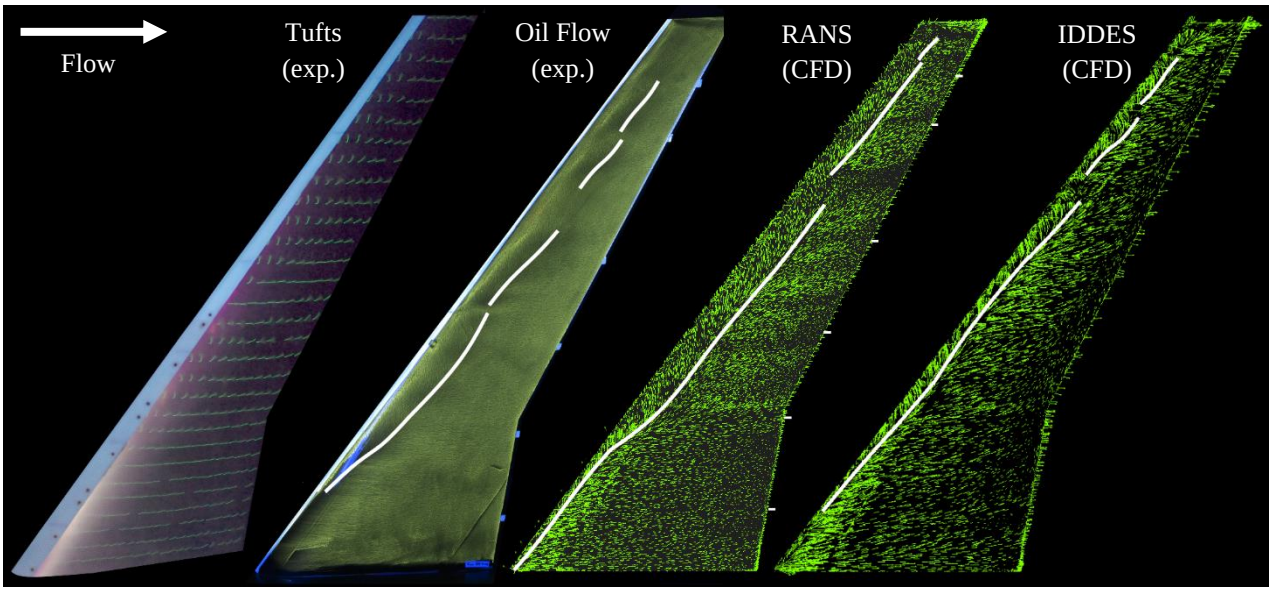

Fig. 4.7 Comparison of time-averaged surface flow patterns at 6-deg. angle of attack for a) experimental mini tufts, b) experimental oil flow visualization, and computational wall shear stress for the baseline mesh using c) RANS and d) IDDES. White lines indicate flow reattachment location.

fully capture the same fluid dynamics as the experimental data and there is a clear reduction in the area of separation in the chordwise direction across the span of the wing. The highlighted reattachment line has noticeably moved closer to the leading edge.

The differences between RANS and IDDES at an angle of attack of 6-deg. can be seen at an angle of attack of 8-deg. in Figure 4.8. RANS provides a very accurate representation and prediction of the near-wall flow field for both the baseline and refined mesh, but IDDES is unable to replicate the same flow features. Similar to Fig. 4.4, which showed very distinct turbulence structure groupings, the same patterning can be seen in the wall shear stress data. Whereas both the experimental and RANS data show complete flow separation past the Yehudi break in the spanwise direction, IDDES shows limited regions of separation that do not extend to the trailing edge of the wing. While the prediction using the refined mesh is generally better than the baseline mesh, it still predicts limited regions of separation. An underprediction of separation is consistent with an overprediction of turbulent entrainment and mixing so that the mixing layer grows quicker and attaches sooner. This suggests that IDDES is over-predicting turbulent mixing in the grey region, where both RANS-like turbulent mixing and LES-like turbulent mixing are present. Such grey area transition can be difficult to predict for HRL methods when the flow separation point is not distinct. However, for the present flow, the strong three-dimensionality (as evidenced by the many of the tufts pointing in the spanwise direction) may be the primary problem since previous studies of ice effects on highly two-dimensional wings were reasonably predicted by the same IDDES method used here [11].

At an angle of attack of 10-deg., as seen in Fig. 4.9, IDDES and DES can better predict the flow field when compared to both the experimental data and the RANS data. Similar to what is seen at an angle of attack of 8-deg., the experimental data shows that the flow is attached near the root of the wing and is separated over the upper surface of the wing past the Yehudi break. For DES and

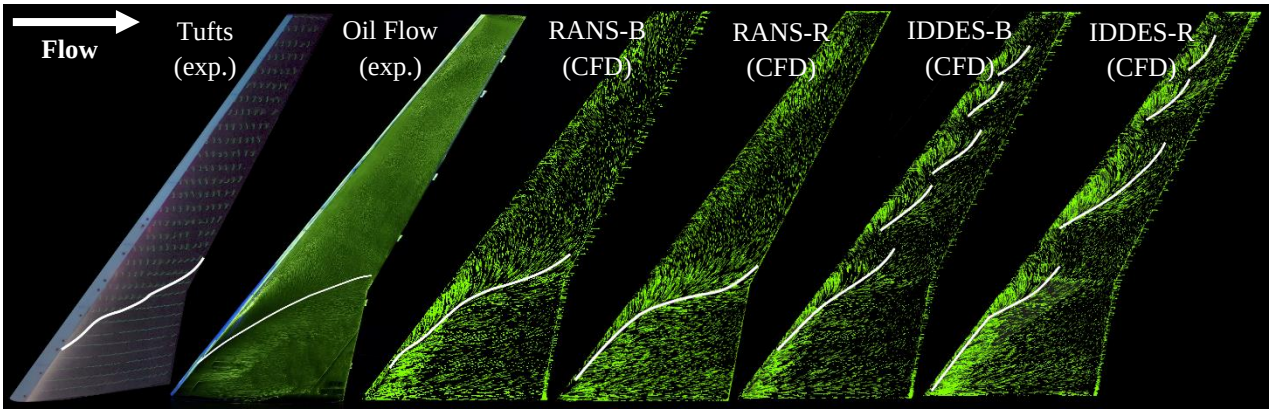

Fig. 4.8 Comparison of time-averaged surface flow patterns at 8-deg. angle of attack for a) mini tufts, b) oil flow, and computational wall shear stress using c) RANS with baseline mesh, d) RANS with refined mesh, e) IDDES with baseline mesh, and f) IDDES with refined mesh. White lines again indicate flow reattachment location.

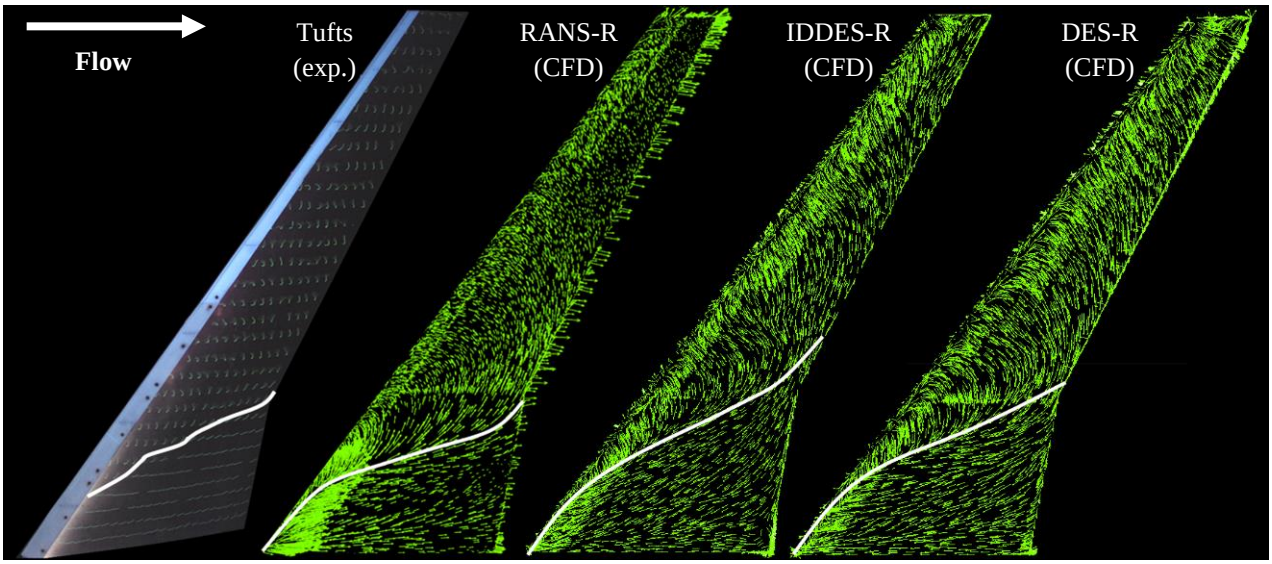

Fig. 4.9 Comparison of time-averaged surface flow patterns at 10-deg. angle of attack for a) mini tufts and computational wall shear stress using the refined mesh for b) RANS, c) IDDES, and d) DES. White lines again indicate flow reattachment location.

IDDES the flow separation has progressed across a majority of the upper surface, but the predictions fall just short of coming below the Yehudi break. Another major point to note that can be seen in Fig.4.7 to 4.9 is the complexity of the flow pattern depicted by both RANS and IDDES. Both sets of data are indicating that the flow within the separated region does not simply point in a single direction but varies widely across the span of the wing. This shows that the flow field

produced by a swept-wing with a leading edge ice shape is significantly more complex than the 2-D separated flow fields highlighted in the review by Stebbins *et al.* [4].

3.2 – Pressure Distributions

The experimental work conducted by Broeren [15] collected pressure data via 10 streamwise rows of pressure taps along the surface of the wing. The pressure tap rows were located at *y/b* = 0.11, 0.28, 0.44, 0.60, 0.81, and 0.90. Figures 10 to 12 leverage the resulting data from the experiment to provide a comparison of the pressure distribution along the surface of the wing. The coefficient of pressure contours generated from the RANS simulations is highlighted in the top left of the figures, while the experimental vs. computational data is shown along the periphery. For understanding flow separation via the pressure distribution plots, Broeren *et al.* [28] characterized separation as being associated with a near-constant coefficient of pressure value versus *x/c*.

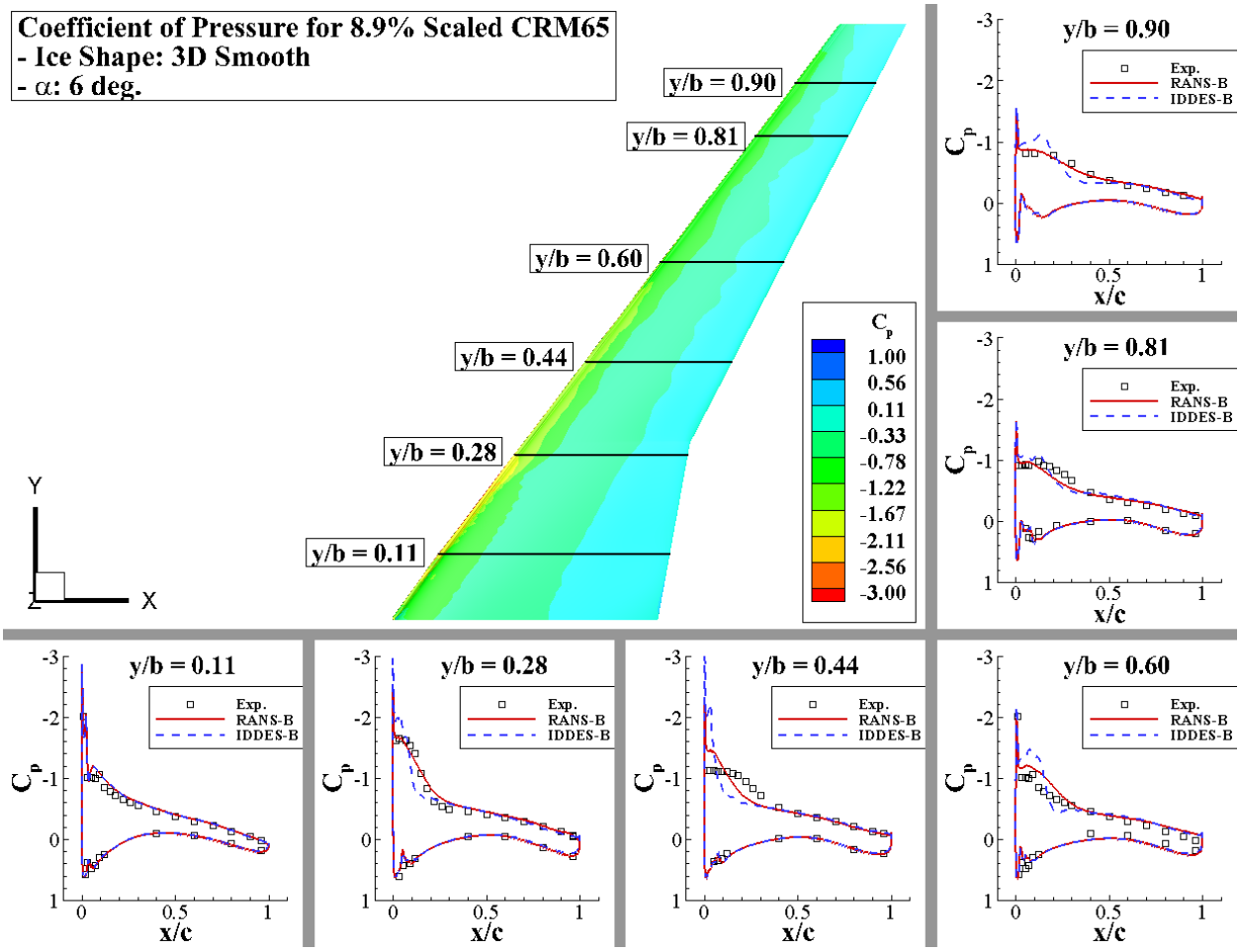

Fig. 4.10 Time-averaged coefficient of pressure color contour on the upper surface for an iced wing at 6-deg. angle of attack with the chordwise coefficient of pressure distribution comparisons at six spanwise locations.

The first set of comparisons to consider is provided in Figure 4.10 for the swept wing at 6-deg. angle of attack. As Stebbins *et al.* [13] noted, the RANS simulations that leveraged the *k-ω* SST turbulence model proved to be quite accurate in capturing the pressure distribution along the wing's lower and upper surface. This remains consistent at each spanwise location. In contrast, we see that IDDES was not able to accurately capture the pressure distribution. Similar to the wall shear stress data highlighted in Fig. 4.7, at the most inboard spanwise location, *y/b* = 0.6, both RANS and IDDES accurately capture the near-surface fluid dynamics. However, examining *y/b* = 0.28 and 0.44, IDDES consistently predicts the flow is reattaching over a shorter distance in the chordwise direction when compared to the experimental and RANS data. This suggests that IDDES is over-predicting turbulent mixing in the grey region, where both RANS-like turbulent mixing and LES-like turbulent mixing are present, and that this over-prediction is related to the strong three-dimensionality of the flow. At spanwise locations beyond *y/b* = 0.44, IDDES can more accurately capture the extent of the flow separation but overpredicts the maximum value of the pressure plateau defining the flow separation. This is again consistent with an overprediction of turbulent mixing in the grey region.

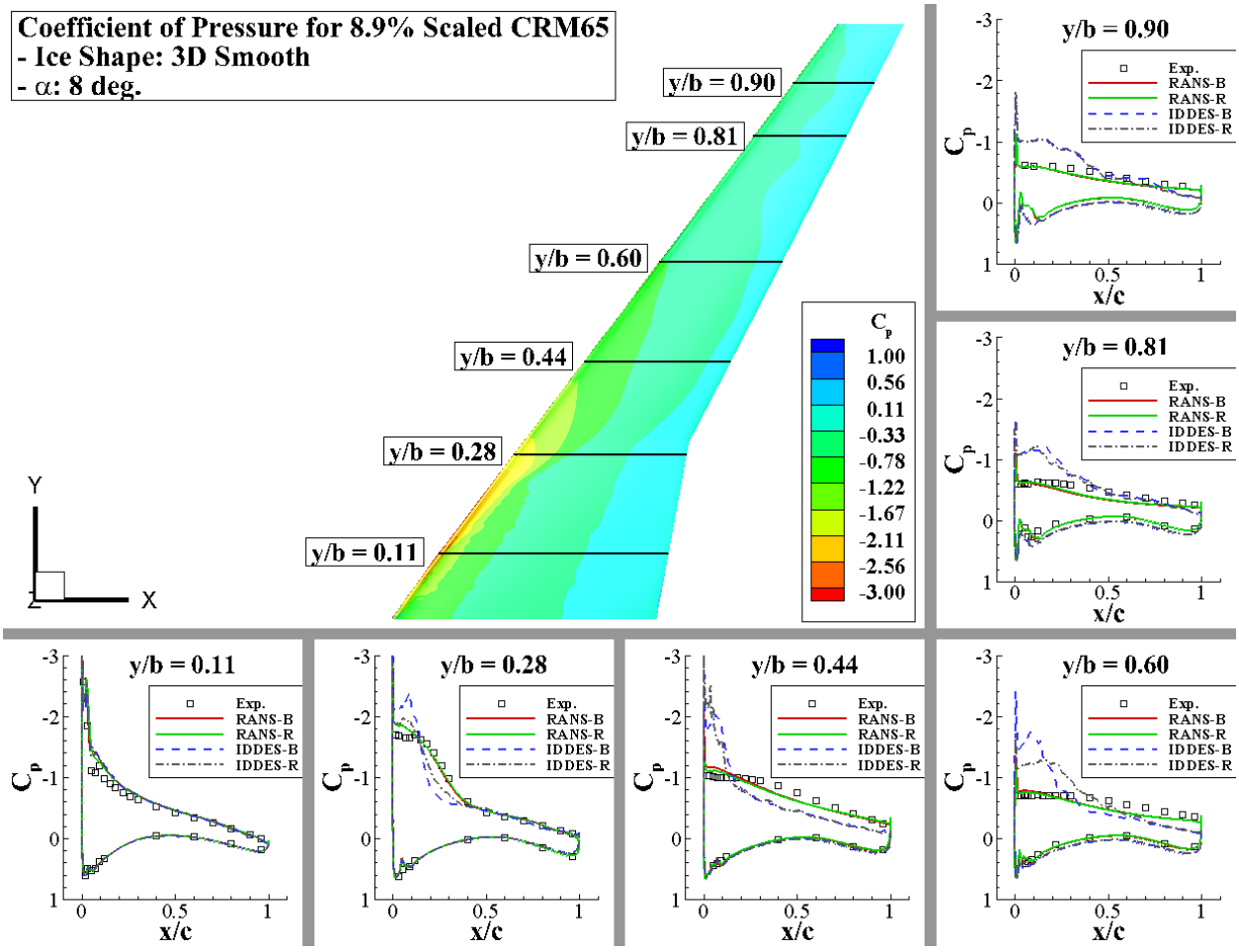

Fig. 4.11 Same as Fig. 10 except for at an angle of attack of 8-deg.

Figure 4.11 provides a similar story regarding experimental vs. RANS vs. IDDES at an angle of attack of 8-deg. Here, the mesh sensitivity study is highlighted and compares the results of the numerical methodologies using two selected meshes. At *y/b* = 0.11, both RANS and IDDES capture the general trend of the pressure distribution albeit with some higher values just aft of the leading edge. Moving outboard, similar to at an angle of attack of 6-deg., IDDES predicts a smaller separation along the upper surface, which leads to errors in predicting the coefficient of pressure. This is consistent with the wall shear stress behavior examined in Fig. 4.8, where the flow is only separated for about half of the chord across the span of the wing, but then reattaches. This result does not line up with the experimental data which shows that the flow should be fully separated at all outboard locations greater than *y/b* = 0.44. Comparing the baseline mesh to the refined mesh, the predicted coefficient of pressure peak along the upper surface is reduced (most notably at *y/b* = 0.60), but the increase in cell resolution does not allow for IDDES to accurately capture the flow field behavior.

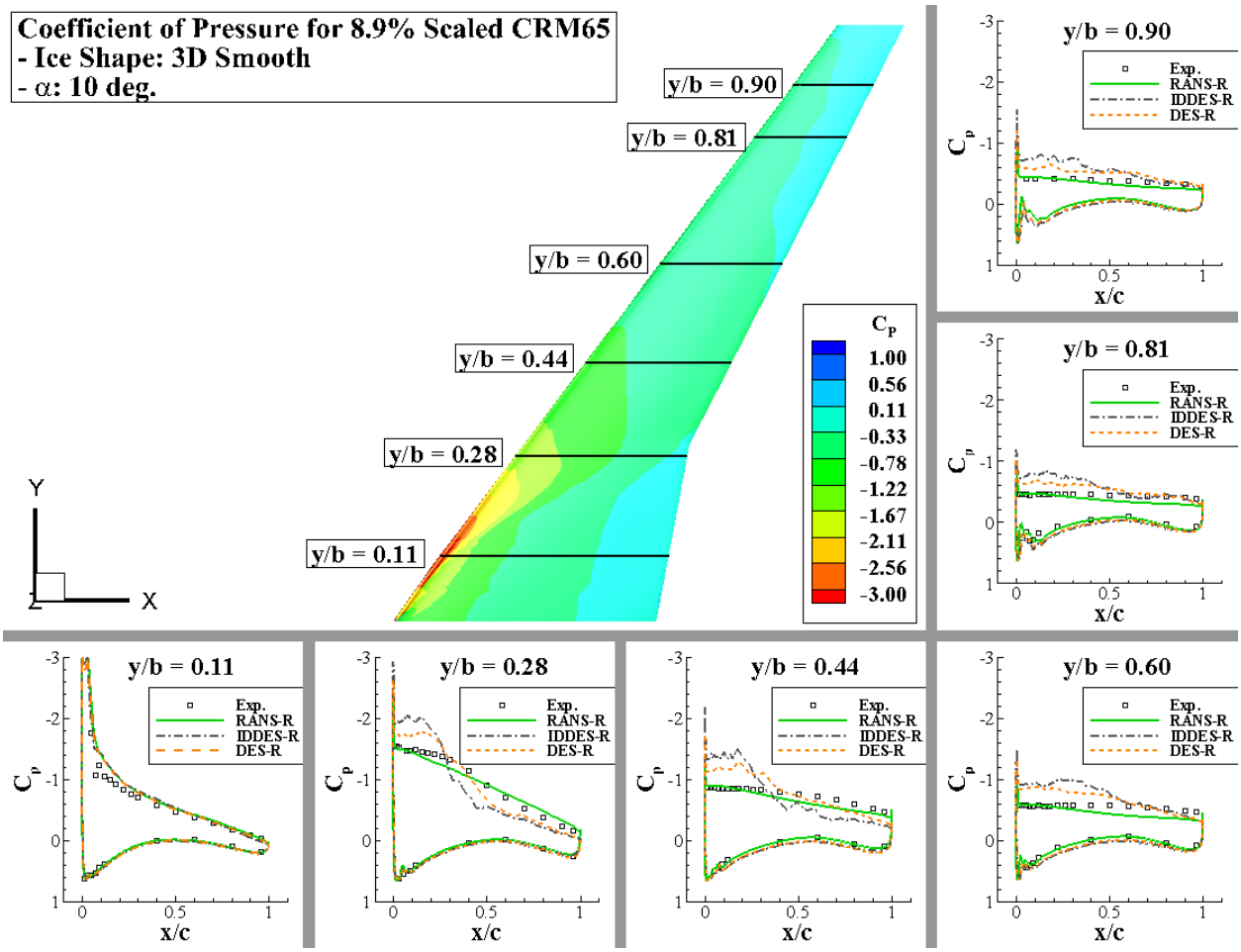

Fig. 4.12 Same as Fig. 10 except at an angle of attack of 10-deg.

Figure 4.12 compares both DES and IDDES to the experimental data and RANS. At an angle of attack of 10-deg., DES and IDDES are more closely aligned with the experimental data and RANS prediction. At y/b = 0.11, the flow is generally attached and the IDDES, DES, and RANS predictions stack closely on top of one another and capture the general trend of the coefficient of pressure. Further outboard, the pressure distribution profiles generated from RANS predicts the complete flow separation across the span of the wing starting at y/b = 0.28. However, the DES and IDDES continue to underpredict flow separation at these outboard locations, e.g. produce coefficients of pressure distributions that are more consistent with the inboard attached flow at y/b = 0.11 than the actually-observed highly separated flow, suggesting that DES and IDDES overpredict turbulent mixing in the grey region when there is complex three-dimensional flow separation.

3.3 – Aerodynamic Coefficients

Figure 4.13 compares the ability of RANS, IDDES, and DES to accurately predict the aerodynamic coefficients of the swept wing with a leading-edge ice shape. Time-averaging was done across IDDES and DES across 1,000 to 4,000 iterations (i.e. 0.5 to 2.0 seconds of flow time) to allow a statistically converged average. As the angle of attack increased, it was necessary to average over a longer period of time in order to obtain a stable solution (i.e. the angle of attack of 6-deg. case took 1,000 iterations while the angle of attack of 10-deg. case took 4,000 iterations). In Fig. 4.13a, RANS captures both the trend and value at low to moderate angles of attack but begins to underpredict the value around 8-deg. At an angle of attack of 6 and 8-deg., DES and IDDES can accurately capture the coefficient of lift, but this is contradictory to the numerical methods' ability to capture the pressure distribution along the span of the wing as noted in Fig. 4.11. This highlights the necessity to not rely only on the time-averaged aerodynamic coefficients to determine the ability of a turbulence model to accurately predict the flow field but to review the flow domain and other characteristics as well. By ignoring the latter, it is possible to improperly accept answers that are misleading and not entirely correct. As the angle of attack increases, it is more apparent the overprediction of the coefficient of pressure magnitude by both DES and IDDES results in a higher lift value. Similar to the coefficient of pressure plots in Fig. 4.12, DES performs slightly better than IDDES at an angle of attack of 10-deg.

Figure 4.13b focuses on comparing the coefficient of pitching moment for the numerical methods versus experimental data. At an angle of attack of 7-deg., the experimental data features a pitching moment break characterized by the sudden slope change from negative to positive. While RANS can accurately capture the coefficient of pitching moment trend up to 6-deg., it predicts that the pitching moment break occurs at a lower angle of attack. Furthermore, it does not accurately predict the value of the coefficient of pitching moment after 8-deg. In contrast to RANS, IDDES does not capture the pitching moment break and carries a negative slope through angles of attack of 8 and 10-deg. DES provides a slight improvement over IDDES, but both HRL methods overpredict the magnitude of the coefficient of pitching moment. This is consistent with the behavior displayed in the pressure distribution plots of Fig. 4.12. Based on a moment arm located at x = 0.4441 m, the overprediction of the pressure distribution at spanwise locations greater than y/b = 0.44 results in a larger negative rolling moment.

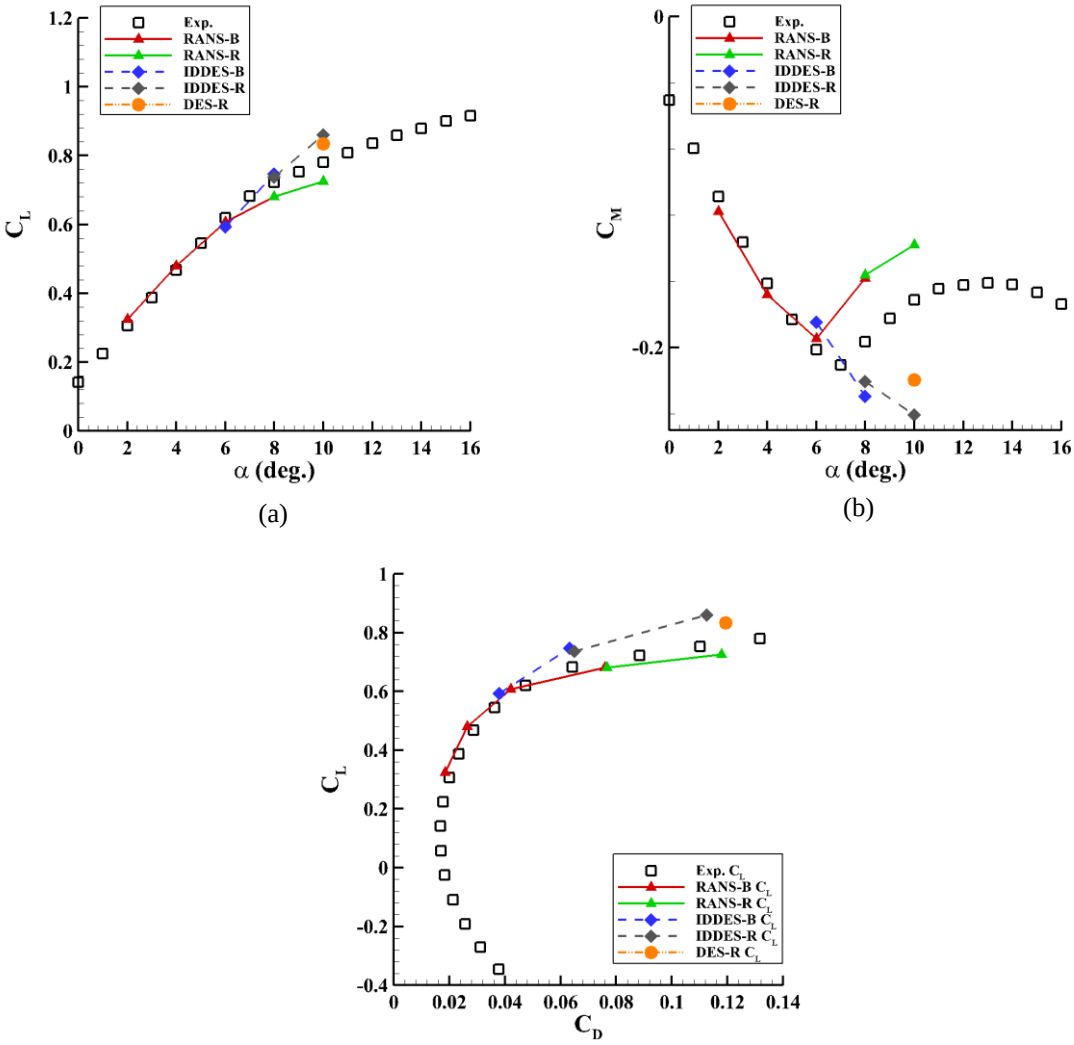

Fig. 4.13 Comparison of experimental and predicted time-averaged aerodynamics for a) coefficient of lift vs. angle of attack, b) coefficient of pitching moment vs. angle of attack, and b) lift-drag polar.

Figure 4.13c shows that the general trend of the Lift-Drag polar is well captured by the turbulence models. At low angles of attack, RANS accurately captures both the lift and drag of the swept wing. As the angle of attack increases, RANS underpredicts both the lift and drag of the swept wing. For IDDES, at an angle of attack of 6-deg., the lift value is well predicted but the drag value is underpredicted. This discrepancy in predicted drag value versus experimental data increases at angles of attack greater than 6-deg. This difference can be associated with the lack of accuracy in predicting the flow separation as highlighted in previous figures.

4 – Conclusion

Recent experimental work has investigated the impact of leading-edge ice accretion shapes on the aerodynamics of a 65% version of the Common Research Model (CRM). The objective of this study is to leverage the accumulated experimental data to assess the ability of DES and IDDES to

predict the complex flow physics and aerodynamic performance for semi-detached flow over a swept wing at moderate angles of attack. The wing in this study was modeled in a computational domain similar to a previous RANS study performed by Stebbins *et al.* [13]. Historically, HRL methods have shown good agreement with experimental data for 3D extruded airfoils and un-swept wings with ice accretion. While IDDES, and more fundamentally DES, were developed to perform well with flow fields that are fully separated, their performance for semi-detached spanwise flows over swept wings is not well documented. To the authors' knowledge, this was the first use of HRL methods to predict the flow physics and aerodynamics of a swept wing with leading-edge ice.

Separated flow over a swept wing is highly unsteady and three-dimensional. *Q*-criterion allows for visualization of the turbulent structures present in the flow field at a snapshot in time. As the simulated angle of attack progresses from 6 to 10-deg., both DES and IDDES predict that the size of these turbulent structures increases as the flow progressively becomes more separated.

The near-wall fluid dynamics were investigated with experimental mini tufts and oil flow visualization data compared to computationally calculated wall shear stress. The experimental results showed that high angles of attack produce high spanwise flow (with many tufts pointing in the spanwise direction) with large outboard flow separation, extending to the trailing edge. While this behavior was captured with RANS, the outboard separation (past the Yehudi break) was significantly underpredicted IDDES and DES due to flow reattachment well before the trailing edge. This is consistent with an overprediction of turbulent entrainment and mixing so that the mixing layer grows quicker and attaches sooner. This suggests that IDDES is over-predicting turbulent mixing in the grey region, where both RANS-like turbulent mixing and LES-like turbulent mixing are present. Such grey area transition can be difficult to predict for HRL methods when the flow separation point is not distinct. However, for the present flow, the strong three-dimensionality may be the primary problem.

The underprediction of outboard separation by DES and IDDES at high angles of attack was also reflected in both the pressure distribution plots and the integrated aerodynamic coefficients. For all angles of attack analyzed in this study, DES and IDDES were only able to capture the pressure distribution at the most inboard spanwise location and did not accurately capture the large outboard flow separation regions. These inaccuracies consisted of both over-predicting the magnitude of the pressure plateau defining flow separation, as well as when the flow reattached to the upper surface of the wing. These discrepancies led to the overprediction of the integrated coefficient of lift, as well as not capturing the right angle of attack at which there is a pitching moment break in the experimental data.

The issues listed above can be linked to the presence of a complex spanwise component of flow velocity over the upper surface of the wing and an inaccurate prediction of the fluid dynamics in the transition zone between the URANS region and the scale-resolved region. This transition zone, or "grey area", is known to be sensitive to the mesh and underlying RANS model as well. However, the present IDDES results show that the underlying RANS model is not problematic and that higher-resolution IDDES did not solve the problem. Therefore, the highly three-dimensional nature of the flow separation is expected to be the primary culprit for the over-predicting turbulent mixing in the grey region, where both RANS-like turbulent mixing and LES-like turbulent mixing are present. Recommendations for future work include the pursuit of three main objectives: 1) understanding the turbulent mixing performance of the "grey area" for predicting iced swept wing aerodynamics, 2) exploring improvements to IDDES and other zonal methods for highly three-

dimensional separation flows to increase accuracy prediction, and 3) investigating the differences in flow physics and aerodynamics for a simplified ice shape (3D smooth geometry) vs. a high fidelity ice shape (3D complex geometry).

Chapter 4 References

[1] Broeren, A. P., Potapczuk, M. G., Lee, S., Malone, A. M., Paul, B. P., and Woodard, B. "Ice-Accretion Test Results for Three Large-Scale Swept-Wing Models in the NASA Icing Research Tunnel." 2016.

[2] Camello, S. C., Lee, S., Lum, C. W., and Bragg, M. B. "Generation of Fullspan Leading-Edge 3D Ice Shapes for Swept-Wing Aerodynamic Testing." *8th AIAA Atmospheric and Space Environments Conference*, AIAA 2016-3737, June 2016. https://doi.org/10.2514/6.2016-3737

[3] Camello, S. C., Bragg, M. B., and Lum, C. W. "Effect of Ice Shape Fidelity on Swept-Wing Aerodynamic Performance." *9th AIAA Atmospheric and Space Environments Conference*, AIAA 2017-4373, June 2017. https://doi.org/10.2514/6.2016-3737

[4] Stebbins, S. J., Loth, E., Broeren, A. P., and Potapczuk, M. "Review of Computational Methods for Aerodynamic Analysis of Iced Lifting Surfaces." *Progress in Aerospace Sciences*, Vol. 111, 2019, p. 100583. https://doi.org/10.1016/j.paerosci.2019.100583.

[5] Alam, M. F., Thompson, D. S., and Walters, D. K. "Hybrid Reynolds-Averaged Navier–Stokes/Large-Eddy Simulation Models for Flow Around an Iced Wing." *Journal of Aircraft*, Vol. 52, 2015. https://doi.org/10.2514/1.C032678.

[6] Zhang, Y., Habashi, W. G., and Khurram, R. A. "Zonal Detached-Eddy Simulation of Turbulent Unsteady Flow over Iced Airfoils." *Journal of Aircraft*, Vol. 53, 2016. https://doi.org/10.2514/1.C033253.

[7] Xiao, M., Zhang, Y., and Chen, H. "Numerical Study of an Iced Airfoil Based on Delayed Detached- Eddy Simulation with Low Dissipation Scheme." *9th AIAA Atmospheric and Space Environments Conference*, AIAA 2017-3761, June 2017. https://doi.org/10.2514/6.2017-3761

[8] Hu, S., Zhang, C., Liu, H., Wang, F., and Li, Y. "IDDES Simulation of Flow Separation on an 3-D NACA23012 Airfoil with Spanwise Ridge Ice." *2018 AIAA Atmospheric and Space Environments Conference*, AIAA 2018-2862, June 2018. https://doi.org/10.2514/6.2018-2862

[9] Spalart, P. R. "Detached-Eddy Simulation." *Annual Review of Fluid Mechanics*, Vol. 41, 2009. https://doi.org/10.1146/annurev.fluid.010908.165130.

[10] Pan, J., and Loth, E. "Reynolds-Averaged Navier-Stokes Simulations of Airfoils and Wings with Ice Shapes." *Journal of Aircraft*, 2004. https://doi.org/10.2514/1.587.

[11] Butler, C., Qin, C., and Loth, E. "Improved Delayed Detached-Eddy Simulation on a

Swept Hybrid Model in IRT." *8th AIAA Atmospheric and Space Environments Conference*, AIAA 2016-3736, June 2016. https://doi.org/10.2514/6.2016-3736

[12] Saini, R., Karimi, N., Duan, L., Sadiki, A., and Mehdizadeh, A. "Effects of Near Wall Modeling in the Improved-Delayed-Detached-Eddy-Simulation (IDDES) Methodology." *Entropy*, Vol. 20, No. 10, 2018, p. 771. https://doi.org/10.3390/e20100771.

[13] Stebbins, S., Loth, E., Broeren, A., Potapczuk, M., and Porter, C. "Aerodynamics of a Common Research Model Wing with Leading-Edge Ice Shape." *Journal of Aircraft*, Vol. 58, No. 4, 2021. https://doi.org/10.2514/1.C036188.

[14] Vassberg, J., Dehaan, M., Rivers, M., and Wahls, R. "Development of a Common Research Model for Applied CFD Validation Studies." *26th AIAA Applied Aerodynamics Conference*, August, 2008. https://doi.org/10.2514/6.2008-6919.

[15] Broeren, A. P., Woodard, B., Diebold, J. M., and Moens, F. "Low-Reynolds Number Aerodynamics of an 8.9% Scale Semispan Swept Wing for Assessment of Icing Effects," *9th AIAA Atmospheric and Space Environments Conference*, AIAA 2017-4372, June 2017. https://doi.org/10.2514/6.2017-4372

[16] Lawson, S. J., Woodgate, M., Steijl, R., and Barakos, G. N. "High Performance Computing for Challenging Problems in Computational Fluid Dynamics." *Progress in Aerospace Sciences*, Vol. 52, 2012, pp. 19–29. https://doi.org/10.1016/j.paerosci.2012.03.004.

[17] Deck, P. R., Deck, S., Shur, M. L., Squires, K. D., Strelets, M. Kh., and Travin, A. "A New Version of Detached-Eddy Simulation, Resistant to Ambiguous Grid Densities." *Theoretical and Computational Fluid Dynamics*, 2006, pp. 181–195. https://doi.org/10.1007/s00162-006-0015-0.

[18] Shur, M. L., Spalart, P. R., Kh, M., and Travin, A. K. "A Hybrid RANS-LES Approach with Delayed-DES and Wall-Modelled LES Capabilities." *International Journal of Heat and Fluid Flow*, Vol. 29, No. 6, 2008, pp. 406–417. https://doi.org/10.1016/j.ijheatfluidflow.2008.07.001.

[19] Menter, F. R. "Two-Equation Eddy-Viscosity Turbulence Models for Engineering Applications." *AIAA Journal*, Vol. 32, No. 8, 1994. https://doi.org/10.2514/3.12149.

[20] Stebbins, S. J., Qin, C., and Loth, E. "Computations of Swept Wing Icing Aerodynamics." *AIAA SciTech 2019 Forum*, AIAA 2019-0328, January 2019. https://doi.org/10.2514/6.2019-0328

[21] Steinbrenner, J. P. "Construction of Prism and Hex Layers from Anisotropic Tetrahedra." *22nd AIAA Computational Fluid Dynamics Conference*, AIAA 2015-2296, June 2015.

https://doi.org/10.2514/6.2015-2296

[22] Stebbins, S. J., and Loth, E. “Computational Analysis of the Wake Structure of a Swept-Wing.” *AIAA SciTech 2022 Forum*, AIAA 2022-1170, January 2022. https://doi.org/10.2514/6.2022-1170

[23] Chakraborty, P., Balachandar, S., and Adrian, R. J. “On the Relationships between Local Vortex Identification Schemes.” *Journal of Fluid Mechanics*, Vol. 535, 2005, pp. 189–214. https://doi.org/10.1017/S0022112005004726.

[24] Hunt, J. C. R., Wray, A. A., and Moin, P. “Eddies, Streams, and Convergence Zones in Turbulent Flows.” *Center for Turbulence Research, Proceedings of the Summer Program*, No. 1970, 1988.

[25] Jeong, J., and Hussain, F. “On the Identification of a Vortex.” *Journal of Fluid Mechanics*, Vol. 285, 1995. https://doi.org/10.1017/S0022112095000462.

[26] Chong, M. S., Perry, A. E., and Cantwell, B. J. “A General Classification of Three-Dimensional Flow Fields.” *Physics of Fluids A: Fluid Dynamics*, Vol. 2, No. 5, 1990. https://doi.org/10.1063/1.857730.

[27] Brown, C. M., Kunz, R. F., Kinzel, M. P., Lindau, J. W., Palacios, J. L., and Brentner, K. S. “RANS and LES Simulation of Airfoil Ice Accretion Aerodynamics.” *6th AIAA Atmospheric and Space Environments Conference*, AIAA 2014-2203, June 2014. https://doi.org/10.2514/6.2014-2203

[28] Poll, D. “Spiral Vortex Flow Over a Swept-Back Wing.” *The Aeronautical Journal*, Vol. 90, No. 85, 1986, pp. 185–199.

[29] Broeren, A. P., Diebold, J. M., and Bragg, M. B. “Aerodynamic Classification of Swept-Wing Ice Accretion.” Cleveland, Ohio, 2013.

Chapter 5

Simulations of Ice Particle Impacts on a Hypersonic Forebody

1 – Introduction

The growing desire for hypersonic vehicles has steadily pushed the design and development of various types of vehicles forward. These vehicles range from single to repeated use, and from air-breathing propulsion systems to boost and glide. One of the many concerns for the development of these vehicles is their ability to withstand the various environments and atmospheric conditions they are exposed to within their flight envelope. Their flight envelope, examples of which can be seen in Fig. 5.1, encompasses a range of altitudes at which various meteorological particles can exist. At high velocities, these particles can be damaging to a vehicle's forebody, engine components, optical sensors and radomes [1]. As such, engineers need to be aware of the materials being used and coatings applied to counteract erosion for key components.

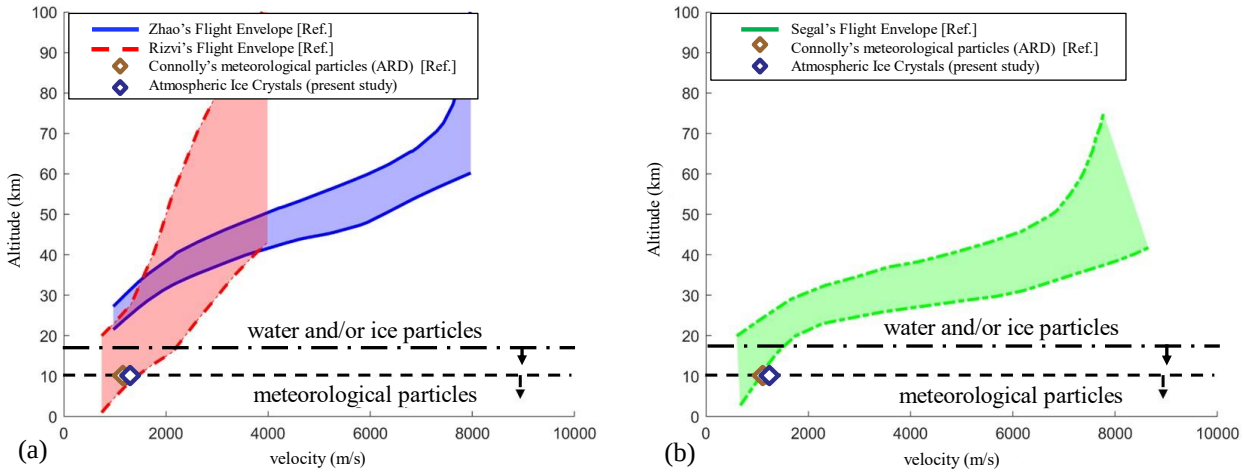

Fig. 5.1 General flight envelopes of a) boost-glide and b) air-breathing hypersonic vehicles with maximum altitudes expected for meteorological particles [9] and ice particles analyzed herein.

Recent studies have focused on understanding two key components surrounding the physics of particle interaction with hypersonic vehicles. The first component entails identifying the type of particles that can exist at relevant altitudes and their various characteristics. A particle's material, shape, and size all have a driving influence on how they behave in the hypersonic flow regime as well as what damage it can cause to vehicles. Understanding what type of particles exist helps to understand the driving physics and particle trajectories. These aspects play an important role in the overall damage and erosion of the material covering a surface [2–8]. Connolly *et al.* [9] highlighted that there are very few publicly available studies of particles at hypersonic speeds. Those that are available, have utilized first-order theoretical approximations [10,11] and did not consider either the shape of the particle or the flow compressibility.

The second component of these studies utilized experiments and simulations to focus on understanding a small subset of models defining the erosion of surface materials. Erosion occurs when a given object is subjected to the repeated impact of particles that exist in a given fluid domain (e.g., flying through a cloud composed of water and ice). Most studies have found that while damage to the vehicle caused by meteorological particles is a function of the particle's characteristics, it is also a function of the vehicle's material composition and resistance to erosion [8]. One such study completed by Cai *et al.* [2], examined the impact of various-sized quartz sand particles on a boronized coating, whose properties can be found in the reference. The results allowed them to develop the following empirical formula for erosive weight loss per unit time of a boronized coating:

$$E_m = \sin(\beta)\, v_p^{e1} d_p^{e2}\, \rho_p^{e3} q k \rho_c K_c^{e4} H^{e5} \tag{5.1}$$

Where q is mass of the incoming particles (kg/h), β is the incident angle of the particle impact trajectory relative to the surface (˚), ρ_c is the density of the coating (g/m3), ρ_p is the density of the particles (g/m3), v_p is the impact velocity of the particles (m/s), d_p is the particle diameter (μm) , K_c is the fracture toughness of the target (MPa·m$^{1/2}$), and H is the microhardness of the target (GPa). The exponents *e1*, *e2*, *e3*, *e4*, and *e5* are assigned values based on the best fit for the experimental data.

Another study done by Lorenz [8] highlighted that the total erosion wear of an object is a combination of the cutting wear and impact wear. At low impact angles, the impact wear is essentially negligible. With other simplifications noted by Lorenz, the total erosion wear, or WR_t (g), reduces to:

$$WR_t = \frac{m_{p,total} v_p^2 cos^2 \beta}{2\varphi} \tag{5.2}$$

Where Lorenz defined $m_{p,total}$ as the total weight of the particles impinging on the target (lb), β as the impact angle (˚), v_p is the impact velocity of the particles (ft/s), φ is the cutting resistance of the material (ft-lb/g).

Palmer *et al.* [6] further built on the work done by Lorenz and Papadopoulos *et al.* [8,12] to develop generic erosion models with respect to crater diameter and depth due to particle impact on various materials for heat shields. The overall erosion/recession of the heatshield, Σp (m), was found to be a function of the crater diameter (D_c), crater penetration depth (p), impact angle (β), and number of particles impacting the target per unit area (N_p).

$$\sum p \sim D_c^2 p N_p (\cos\beta)^n \tag{5.3}$$

Computational advancement in fluid dynamic analysis has allowed for both the analysis of shock boundary-layer interactions stemming from complex geometries as well as providing increased fidelity in hypersonic flow fields such that erosion models can be used in conjunction with predicted particle trajectories. Accurate flow field predictions requires increased fidelity in predicting the drag and impact physics of irregular-shaped solid particles [13]. For medium-fidelity models, one-way coupling (i.e., only calculating fluid impact on particle) for the particle trajectory is sufficient as high-fidelity models require resolution of the physics defining the particle influence on the fluid and particle to particle interaction. These interactions are on the order of milliseconds and would result in a substantial cost to model the numerous particle impacts that will occur over the surface of the vehicle body. Additionally, medium-fidelity simulations will support reducing the scope of high-fidelity simulations by eliminating the subset of particles that have a small enough aerodynamic response time. These particles will generally be influenced by the freestream flow direction before interacting with the boundary layer and will be carried away from the vehicle body.

The objective of this study is to understand the theoretical trajectories, changes in characteristic particle properties, and subsequent impact and erosion for a range of ice particle diameters. While the impact of particles on subsonic vehicles has been widely researched and understood [14,15], there are only a select number of studies that look at the impact on hypersonic vehicles either experimentally or computationally. To support this analysis, a particle drag model will be used to determine the influence of ice particle shape on the final trajectory in a compressible flow. For a large set of particles injected at discreet radial locations along the nose cone of the vehicle body, discrete particle properties, such as velocity and temperature, are tracked from injection to impact. These properties will be compiled and analyzed to determine potential damage to the vehicle body as well as any phase change of the ice particles before impact. To the authors' knowledge, this is the first publicly known study to utilize computational methods to consider and track atmospheric ice particles based on shape and mass distribution, analyze their impact on a hypersonic vehicle at a specified point in the flight trajectory, and determine mass erosion per unit time based on empirical formulas derived from particle impacts on specific materials.

2 – Approach

2.1 – Flight Condition

As noted by Connolly *et al.* [9], particle damage is a combination of both the particle impact physics as well as the net number of particles. As altitude increases, there is both a reduction in the influence of drag on the particle trajectory before impact, as well as an increase in the theoretical vehicle velocity based on the flight trajectories seen in Fig. 5.1. However, an increase in altitude will also result in a decrease in the particle concentration present along the flight trajectory. An Advisory Circular released by the Federal Aviation Administration (FAA) [16] notes that clouds composed of ice particles can exist past 10 km, but Ekelund et al. [17] have shown that the ice water concentration (IWC) of clouds is the greatest around 6 km and begins to rapidly decrease past 10 km. At 10 km, the peak IWC observed is approximately 400 g/m3 and will be utilized in this study. Focusing on a flight condition with an altitude of 10 km and a vehicle speed of 1,200 m/s ($Re_v = 33.7 \cdot 10^6$) will allow for a reasonable analysis of ice particle impact and a comparison against previous data for ash/sand particles. At this altitude, the freestream temperature and pressure are -50 ˚C and 26,436.3 Pa respectively.

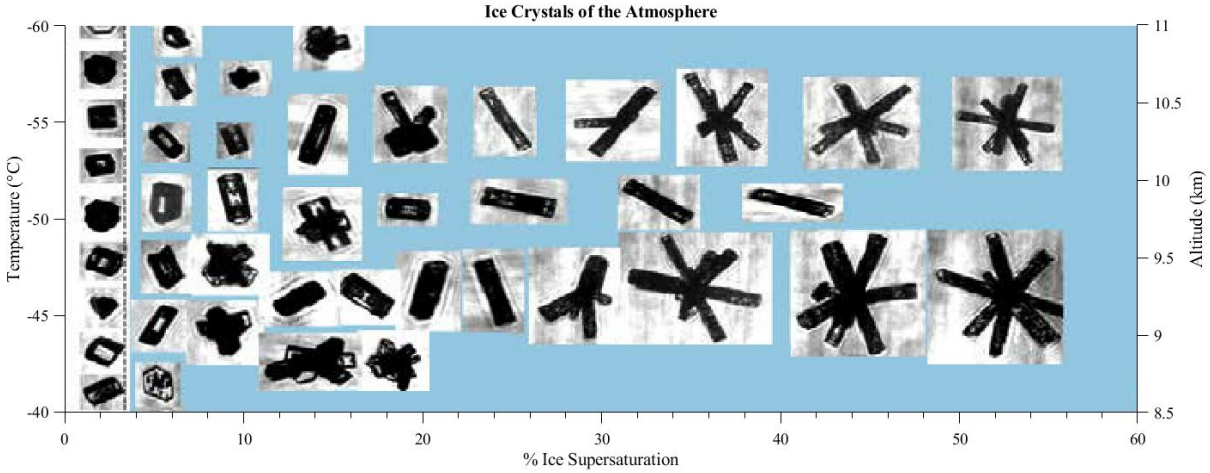

Fig. 5.2 Images of ice shapes for altitudes ranging from 8.5 to 11 km and temperatures ranging from -60 to -40 ˚C including a wide range of ice supersaturation. (Adapted from Bailey et al. [28])

The hypersonic vehicle selected for this study is based on the geometries outlined by Connolly *et al.* [9]. The forebody is an axisymmetric cone with a 15 deg. half-angle and a leading-edge radius of 10 mm. Only the forebody was simulated as this is one of the more critical regions of a hypersonic vehicle due to the complex gas-dynamic and boundary layer interaction occurring near the bow shock. The geometry was designed such that the streamwise coordinate (x) would be 0 at the point where the conical forebody would meet the axis line if there was no leading-edge radius. This results in an actual nose tip that starts at x = 0.0286 m.

2.2 – Ice Shapes and Mass Distributions

At the flight condition for this study, three different types of ice shapes can be found: plate-like, column-like, and irregular (used interchangeably with aggregate). Each of these ice shapes can be seen in Fig. 5.2, and Table 5.1 highlights the different concentration levels of the ice shapes at -50 ˚C. Additionally, at this altitude, the peak While irregular ice shape has the largest concentration of the three types, it is necessary to pre-determine whether or not this ice shape, which resembles an aggregation of column-like ice shapes, can withstand the pressure jump across the shock emanating from the vehicle body. Gundlach [18] found that irregular (or aggregate) ice shapes have a tensile strength of <5 kPa. At an altitude of 10 km, the freestream pressure is 26,344 kPa. Using oblique shock wave equations, the theoretical pressure increase P_1/P_0 is 3.697 across the shock. This results in a sufficient pressure differential that will cause the irregular ice shape to break up before impact on the vehicle body. This study then assumes that the aggregate ice shape break up will result in a variety of sizes that are largely column ice shapes.

The ice diameters used in this study are based on the bins defined originally by Jeck [19] and supplemented by information compiled by Moisseev et al. [20] for ice particle size data [21,22]. Plate and column ice naturally form up to 3,000 μm and irregular types of ice shapes dominate the particles that are sized 3,000 μm to 10,000 μm in diameter. Assuming that the irregular ice shapes will break into ice shapes that are half the original diameter, the mass percentage bins defined by Jeck [19] for particles of 3,000 to 6,000 μm and 6,000 to 10,000 μm, will be redistributed accordingly as 1,500 to 3,000 μm and 3,000 to 5,000 μm respectively. Accounting for the

redistributed mass, Table 5.2 tabulates the final ice particle size distribution and the mass percentage that is utilized in this study. This distribution is based on simplifying the bin of ice particle diameters provided at high altitudes by taking the mean of each bin. The final distribution shows that most of the expected mass in a given cloud is associated with 650 and 2,000 μm particles. Additionally, for this study, the particles are assumed to have a density of 917 kg/m^3 and a specific heat capacity of 2,180 J/(kg ˚C).

Table 5.1 Concentration of different ice particle shapes at T_∞ = -50 ˚C. and selected aerodynamic characteristics [27]

Ice Shapes	Concentration (%)	Aspect Ratio (E)	C_{shape}	C_D
Plate-like	21.80	0.27	4.52	1.90
Column-like	31.11	2.37	1.52	0.64
Irregular	47.09	-	-	-

Table 5.2 Bin size distribution by fraction of ice particles mass and by shape [19]

d_p range (μm)	d_p (μm)	m%	m_{plate}%	m_{column}%	$Re_{p,0}$
50 – 100	75	1.5	0.33	1.17	2,530
100 – 300	200	12.0	2.62	9.38	6,740
300 – 1000	650	43.0	9.37	33.63	21,900
1,000 – 3,000	2,000	43.0	9.37	33.63	67,400
3,000 – 5,000	4,000	0.5	0.11	0.39	135,000

2.3 – Numerical Methodology

For this study, the calculation of the particle trajectories is broken into two simulations performed in ANSYS Fluent. The flow field around the vehicle body is solved in the first simulation, and the second simulation consists of injecting the particles into the converged solution of the first simulation. The simulations utilize a density-based solver with third-order discretization in combination with the shear stress transport (SST) turbulence model. The mesh used in both simulations is the product of a coarse mesh subjected to iterative adaptive meshing. The goal of the adaptive mesh was to ensure proper resolution of the shock by determining which cells contained the largest pressure gradients. The overall process, which consisted of splitting the selected cells four times, was repeated five times and created a final refined mesh with $2 \cdot 10^6$ cells. To ensure proper resolution of the boundary layer, an initial cell height in the wall-normal direction was prescribed a length of 0.5 μm. Subsequent cells were generated from the initial layer by using a growth rate of 1.20 until a total of 40 cells span the boundary layer in the wall-normal direction. The final mesh can be seen overlayed on top of pressure contours in Fig 5.3.

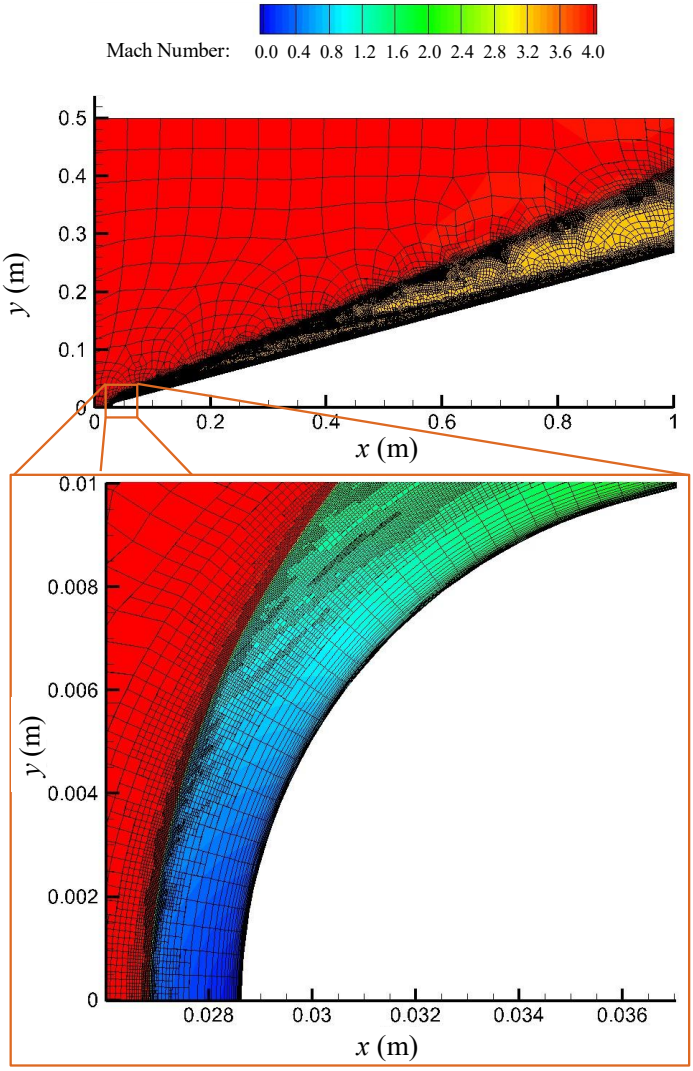

Fig. 5.3 Axisymmetric fine mesh using adaptive meshing near the shock with contours of Mach Number: a) full simulated flow domain and b) closeup near leading edge radius.

For the particle trajectory simulations, it is necessary to define an appropriate particle drag model to accurately predict the particle trajectories and velocities for both plate and column ice shapes. The equation of motion for a particle is defined in ANSYS [23] as the following:

$$\frac{dv_p}{dt} = F_D\left(v_f - v_p\right) + \frac{g_x(\rho_p - \rho_f)}{\rho_p} + F_x \tag{5.4}$$

Where v_p is the particle velocity, v_f is the velocity of the fluid, F_D is the drag force, g_x is the gravitational acceleration, ρ_p is the density of the particle, and ρ_f is the density of the fluid. The last term, F_x, encompasses additional forces calculated by ANSYS that act on the particle. Generally, for meteorological water and ice particles, the effects of gravity can largely be ignored as the particles have no appreciable fall velocity and are balanced by the atmospheric updraft until the particles grow in mass.

The drag force (F_D) is defined by ANSYS as a function of the coefficient of drag (C_D), the relative Reynolds number (Re_p), particle density (ρ_p), and particle diameter (d_p):

$$F_D = \frac{18\mu_f}{\rho_p d_p^2} \frac{C_D Re_p}{24} \tag{5.5}$$

$$Re_p = \frac{\rho d_p |v_p - v_f|}{\mu_f} \tag{5.6}$$

Work completed by Loth [24] found that for non-spherical particles at intermediate particle Reynolds numbers, the coefficient of drag can be defined as the following:

$$C_D = C_D^* \cdot C_{Shape} \tag{5.7}$$

Additionally, the normalized drag coefficient, C_D^*, can be approximated as 0.42 for particles that have a sufficiently high Re_p. This was validated by Loth [24] through a compilation of various studies focused on different particle shapes. For irregular particles, C_{shape} is a function of the normalized surface area, A_{surf}^*:

$$C_{shape} = 1 + 1.5\sqrt{A_{surf}^* - 1} + 6.7\left(A_{surf}^* - 1\right) \; for\, E \leq 1 \tag{5.8}$$

$$C_{shape} = 1 + 0.7\sqrt{A_{surf}^* - 1} + 2.4\left(A_{surf}^* - 1\right) \; for\, E \geq 1 \tag{5.9}$$

Equating plate ice shapes as oblate spheroids (aspect ratio, $E < 1$) and column ice shapes as prolate spheroids (aspect ratio, $E > 1$) it is possible to define A_{surf}^* for both particles as:

$$A_{surf}^* = \frac{E^{-2/3}}{2} + \frac{E^{4/3}}{4\sqrt{1-E^2}} \ln\left(\frac{1+\sqrt{1-E^2}}{1-\sqrt{1-E^2}}\right) \quad for\, E \leq 1 \tag{5.10}$$

$$A_{surf}^* = \frac{E^{-2/3}}{2} + \frac{E^{1/3}}{2\sqrt{1-E^{-2}}} \sin^{-1}\left(\sqrt{1-E^{-2}}\right) \quad for\, E \geq 1 \tag{5.11}$$

Using the tabulated data compiled by Um *et al.* [25] for the aspect ratio of plate and column ice, the final values for E, C_{shape}, and C_D can be found in Table 5.1 and are used for the rest of this study.

3 – Results

3.1 – Gas Flow Around Forebody

As noted in the previous section, Fig. 5.3 overlays the final refined adaptive mesh over contours of Mach number in the full domain (Fig. 5.3a) and near the nose of the vehicle body (Fig. 5.3b). An adaptive mesh was developed before particle injection to ensure proper resolution of the shock formed by the vehicle body in a Mach 4 flow condition. The adaptive mesh results in a distinctly defined weak oblique shock above the vehicle body where the Mach number has decreased from Mach 4 to about Mach 3. Figure 5.3b further highlights the refinement of the adaptive mesh by showcasing the large cluster of cells defining the bow shock near the nose of the vehicle. In this region near the nose of the vehicle, the flow comes to rest at the stagnation point and subsequently interacts with the downstream development of the boundary layer across the surface of the vehicle body. Additionally, this region is where the largest temperature rise occurs across the shock occurs and exceeds 300 ˚C, as seen in Fig 5.4.

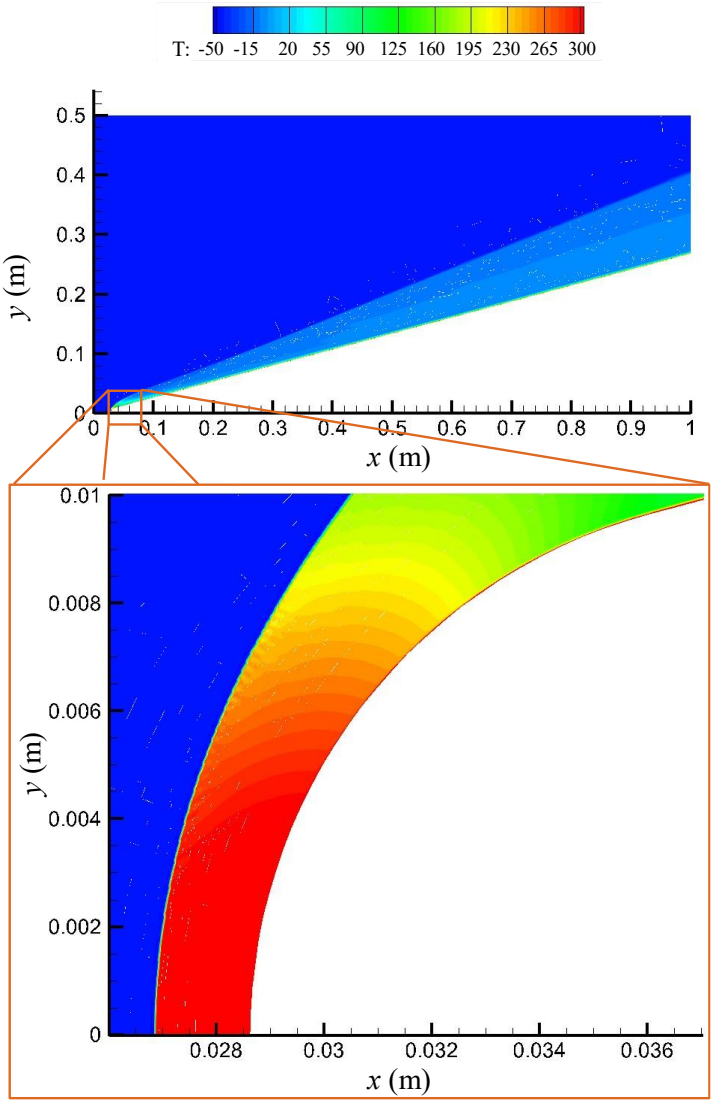

Fig. 5.4 Contours of temperature (˚C) around a hypersonic cone traveling at Mach 4 with a zoomed in view of the boundary layer a) and b).

A grid resolution study was done by Connolly *et al.* [9] on a similar mesh in order to determine the quality of the adaptive mesh. The study consisted of investigating the resolution of the total pressure distribution along the leading-edge nose. As can be seen in Fig. 5.4b, this area was chosen as this was the most complex region with the largest observable gradients. Their study found that the predictions produced by the coarse and refined meshes were nearly identical and thus were confident in achieving grid convergence.

A pressure contour of the fluid domain can be seen in Figure 5.5. As expected of a supersonic flow, the pressure sharply increases downstream of the shockwave. Additionally, Fig 5.5 uses streamtraces to highlight the velocity field of the fluid domain. The presence of the geometry, and subsequently the oblique shock, causes the fluid to turn in the $+y$ direction of the fluid domain. As will be discussed in the following section, this behavior drives the physics of the incoming particles prior to impact on the vehicle forebody.

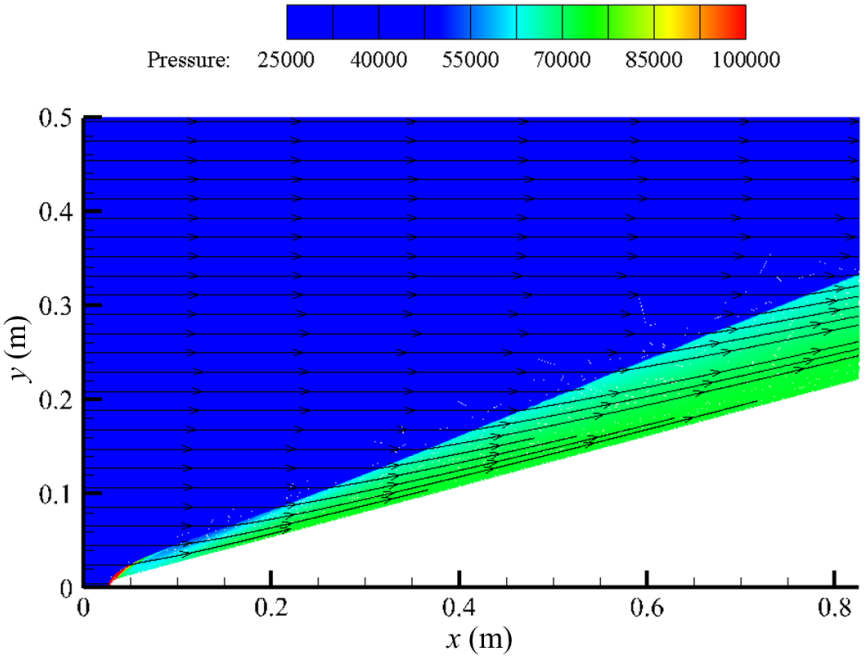

Fig. 5.5 Contours of pressure (Pa) around a hypersonic cone traveling at Mach 4 with an overlay of streamtraces defining the velocity field of the fluid domain.

3.2 – Particle Trajectories

Select particle tracks originating from the inlet boundary condition are highlighted in Fig. 5.6 for both ice shapes with a focus on particle diameters of 75 and 650 μm. One of the key factors to consider when analyzing the impact of the flow domain on particles is the time scales each particle experiences along the trajectory. There are three regimes of time scales to consider: external flow, boundary layer, and particle impact. As noted by Connolly *et al.* [9], each of these time scales can then be compared to the particle response time, which is essentially a function of particle size. Examples provided show that the aerodynamic response time, τ_p, increases with particle size (e.g., a 1μm particle has a response time of ~10 μs whereas a 100 μm particle has a response time of ~0.1 s) [26].

$$\tau_p = \frac{\rho_p d_p^2}{18\mu_f f} = \frac{4\rho_p d_p}{3\rho_f w_{rel} C_D} \tag{5.12}$$

$$w_{rel} = v_p - v_{f@p} \tag{5.13}$$

The smaller the aerodynamic response time, the more likely the particle will be influenced by the time scales of external flow (~$2\cdot10^{-4}$ s), boundary layer (~$2\cdot10^{-5}$ s), and particle impact (~$4\cdot10^{-7}$ s).

Comparing to the study conducted by Connolly *et al.* [9] where the minimum particle diameter analyzed was 1 μm, the minimum diameter of this study is 75 μm. For a 75 μm diameter particle of plate ice, very few of displayed particles were influenced by the flow past the oblique shock and did not impact the surface of the vehicle. As the diameter increases for the plate ice to 650 μm, only one particle trajectory amongst those displayed does not hit the vehicle body. For column ice, the number of trajectories that impact the vehicle body for particles with a diameter of 75 μm (Fig.

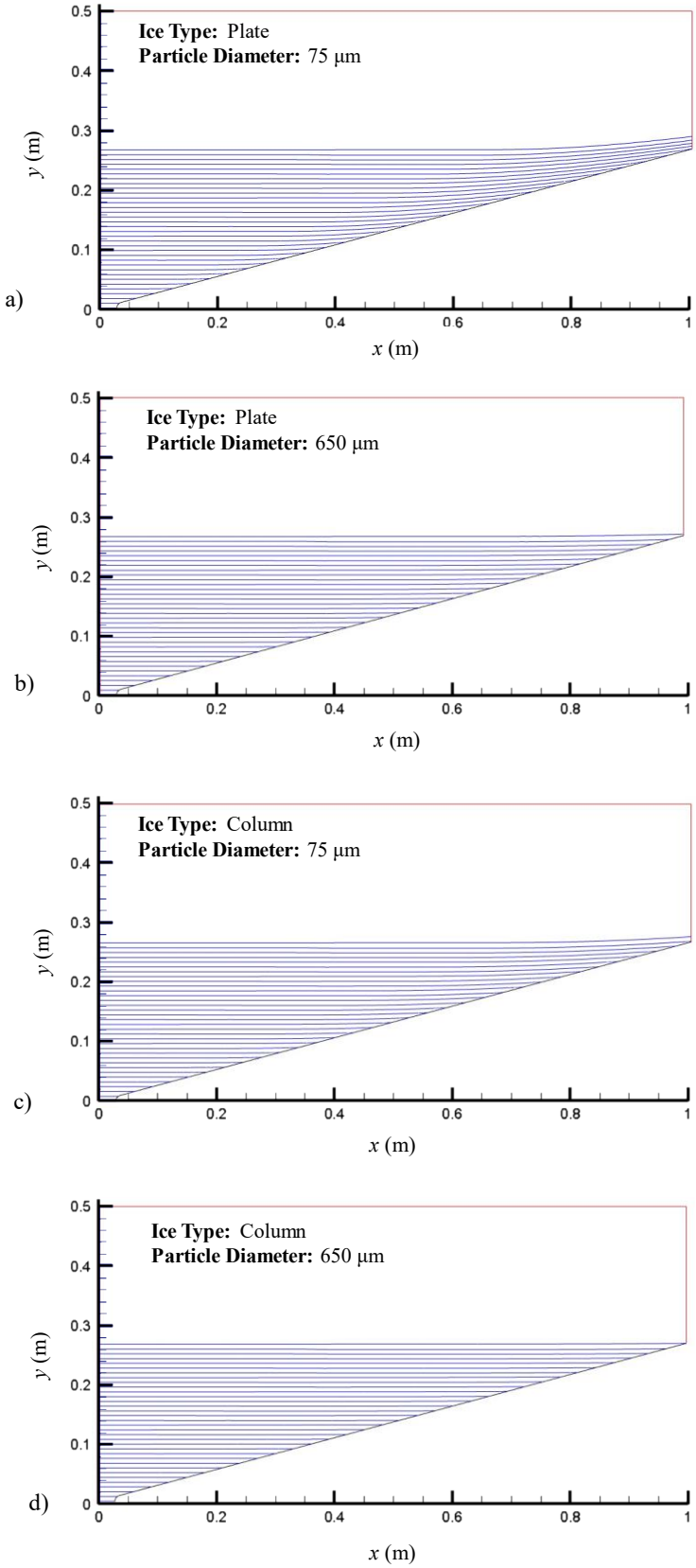

Fig. 5.6 Particle tracks for plate and column ice particle diameters of 75 µm and 650 µm

5.6c) is higher than for plate ice, and all the trajectories shown for the 650 um particles (Fig. 5.6d) make an impact.

As each particle transverses its trajectory, various particle properties change with time. Two key parameters that are tracked in this study are velocity and temperature. Fig. 5.7 captures a select set of particles released at the midpoint of the radial extent of the cone (x = 0, y = 0.134 m). In contrast to the particles analyzed and injected at the same location in the study by Connolly *et al.* [9], every particle impacts the vehicle body. The longest period of travel, defined as the time from injection into the flow to impact with the surface, for the particles is ~0.55 s and is experienced by the 75 μm particle. Over this period, the particle only slows down slightly and impacts at a velocity that is less than 5% different from the initial velocity. As the particle diameter increases to 4,000 μm, the change in velocity is almost negligible and the particle largely impacts at its original injected speed.

Replotting Fig. 5.7 as Impact Velocity Magnitude vs. Particle Diameter in Fig. 5.8, the difference between plate and column ice is further highlighted. Overall, for any given particle diameter, column ice impacts the vehicle at a higher velocity, which can be attributed to the lower coefficient of drag. For the smallest particle size analyzed, the delta change from the initial velocity for the plate ice is twice that of the column ice. As the particle size increases, both particle types experience a relatively low change in velocity. Fig. 5.8b highlights a very close trend for plate and column ice impact as a function of Stokes number (St):

$$St = \frac{u_0}{l_0}\tau_p \tag{5.14}$$

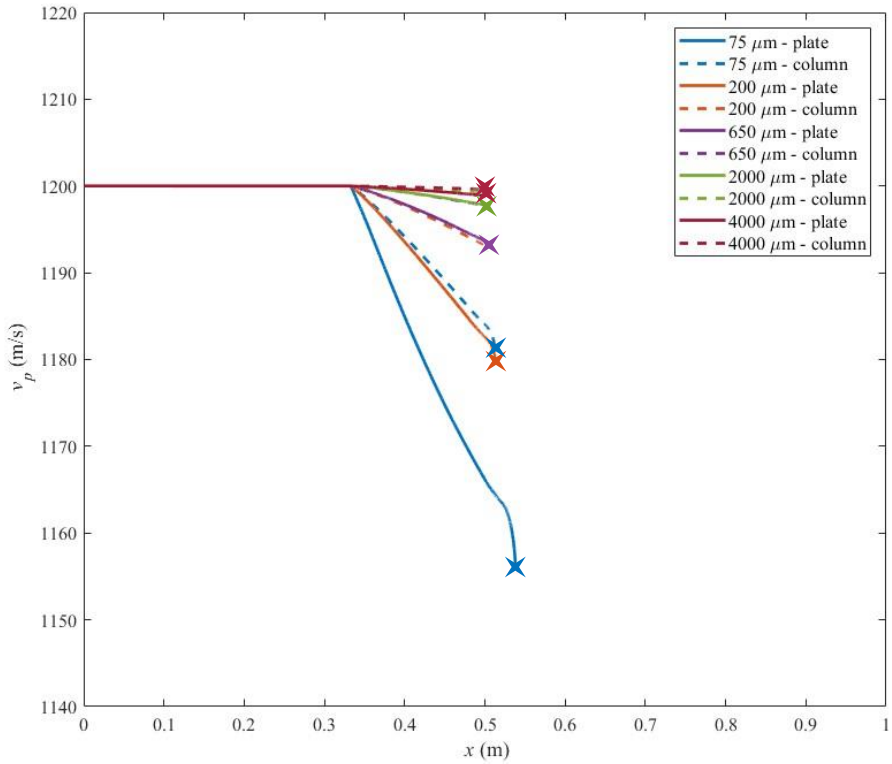

Fig. 5.7 Single particle-track velocities for various plate and column ice particle diameters where the cross marker denotes location of particle impact with the surface.

Where u_0 is the fluid velocity and is assumed to be the flight velocity of 1,200 m/s, and l_0 is the characteristic length and assumed to be the length of the vehicle (1 m).

This trend shows that for a given plate ice diameter, it is possible to find a similar column ice diameter that will impact at the same velocity and vice versa. The Stokes number is a dimensionless constant that characterizes the physics governing the change in particle behavior in a given fluid domain. In general, for $St >> 1$, particles will tend to not follow the flow streamlines, and vice versa for $St << 1$. The main difference between the two ice shapes in regards to the calculation of Stokes number is the C_D value. Another key point reflected in this image is the fact that the calculated Stokes number, which is a function of the aerodynamic response time, for all the ice particles are much greater than 1. This further supports the particle tracks plotted in Fig. 5.6 in which there is largely no change in the pathlines downstream of the shock, albeit those derived from the smallest analyzed particles at the furthest radial extent of the cone.

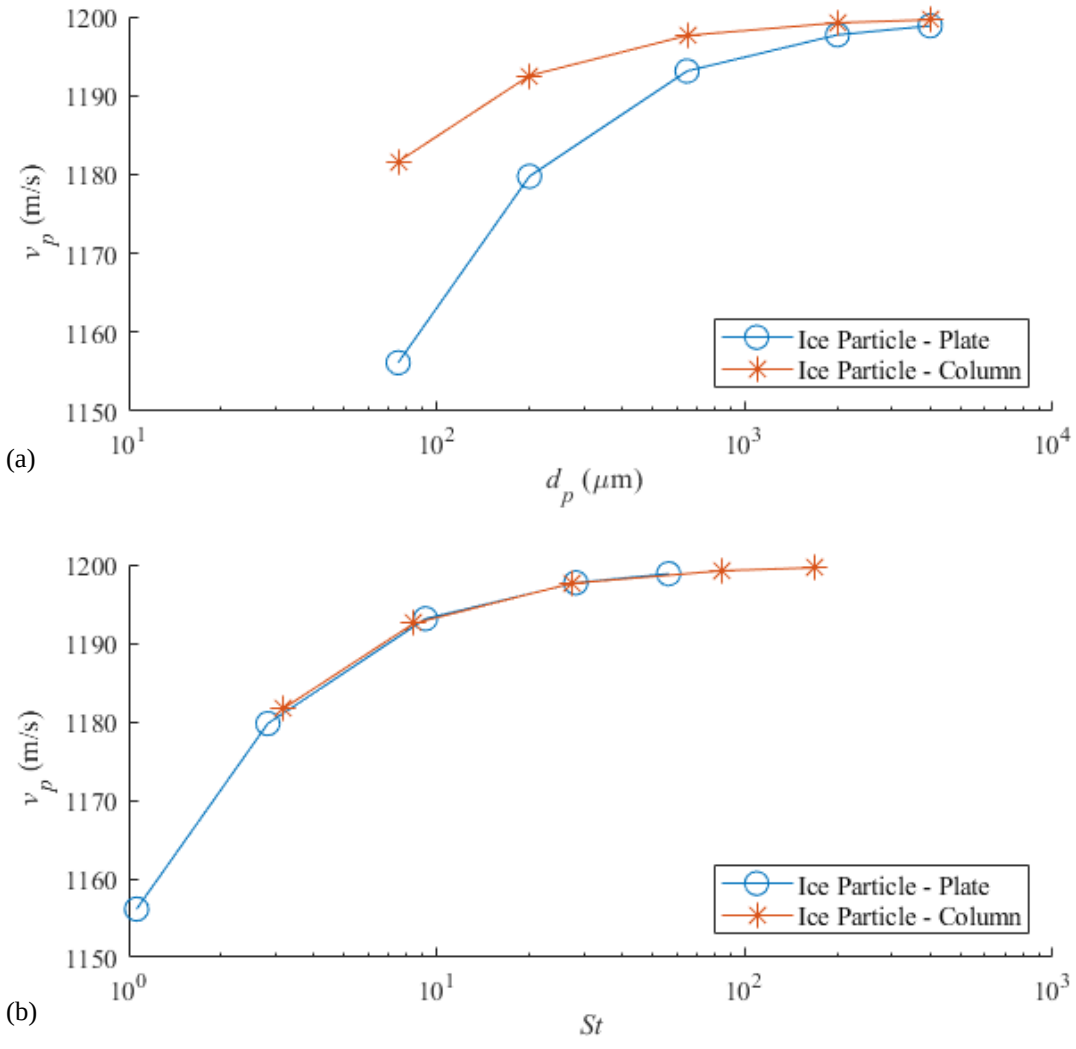

Fig. 5.8 Comparison of impact velocity for Connolly's meteorological particles (ARD) [9], plate-shaped ice particles, and column-shaped ice particles as a function of: a) diameter and b) Stokes number

One of the various unknowns associated with ice particle impact on a hypersonic body is if the particle will undergo a phase change from ice to water before impact. If a phase change occurs, then not only will this modify key particle characteristics such as shape (which effects drag), but will also subsequently alter the physics of the particle impact and erosion of the vehicle body. However, as seen in Fig. 5.9, the change in temperature (ΔT_p) of the particles over the trajectory is minimal and the 75 μm particle experiences the greatest a $\Delta T_p < 4$ ˚C. This highlights that in the scope of this study, there is no concern for phase change of the particles as the particle temperature remains below freezing, and an assumption can be made that the ice particles will largely remain solid as they impact the vehicle body. However, as seen in the study by Connolly *et al.* [9], as the particle size decreases, the period of time of the particle trajectory before impact increases and results in an increase in duration in which the particle's temperature can raise (e.g., a 10 μm ARD particle experienced a ΔT_p ~65 ˚C). Thus, future studies that analyze smaller ice particles should be cognizant of this behavior and be diligent and tracking particle temperature versus time before impact.

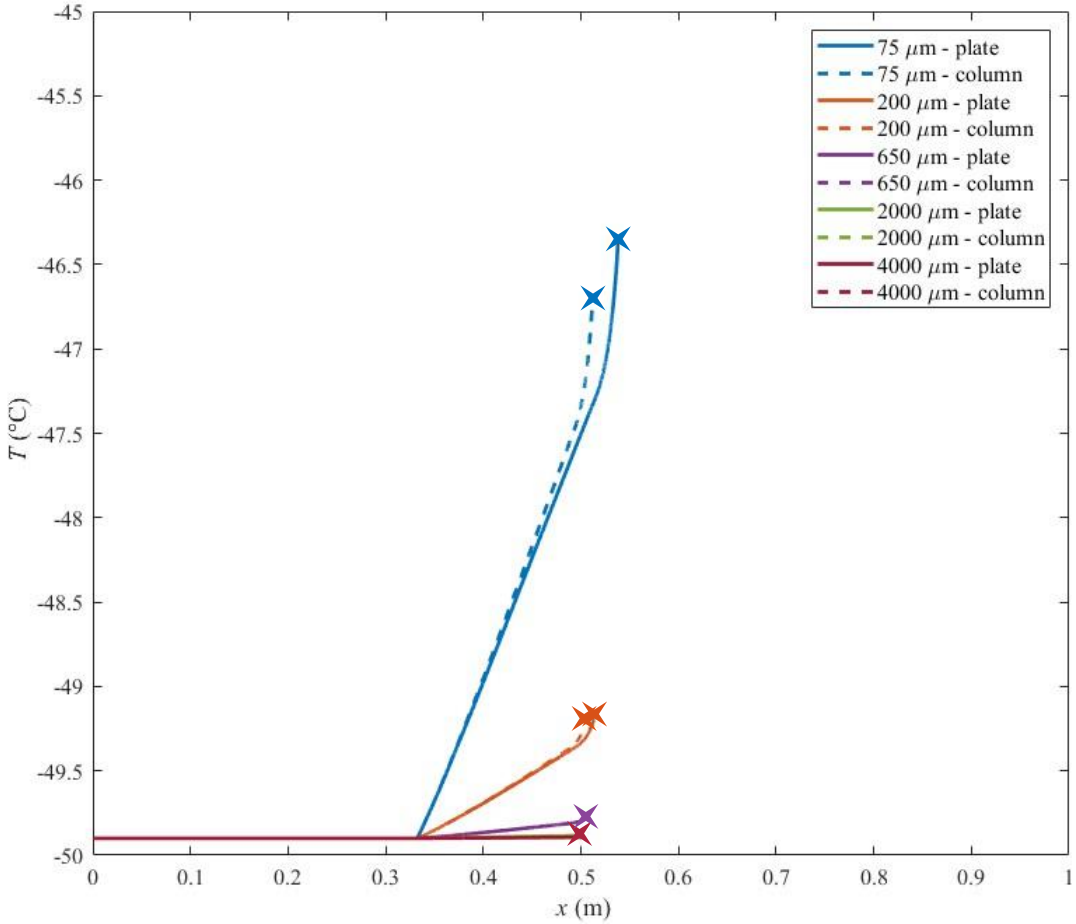

Fig. 5.9 Single particle-track temperatures for various plate and column ice particle diameters, where the cross marker denotes location of particle impact with the surface.

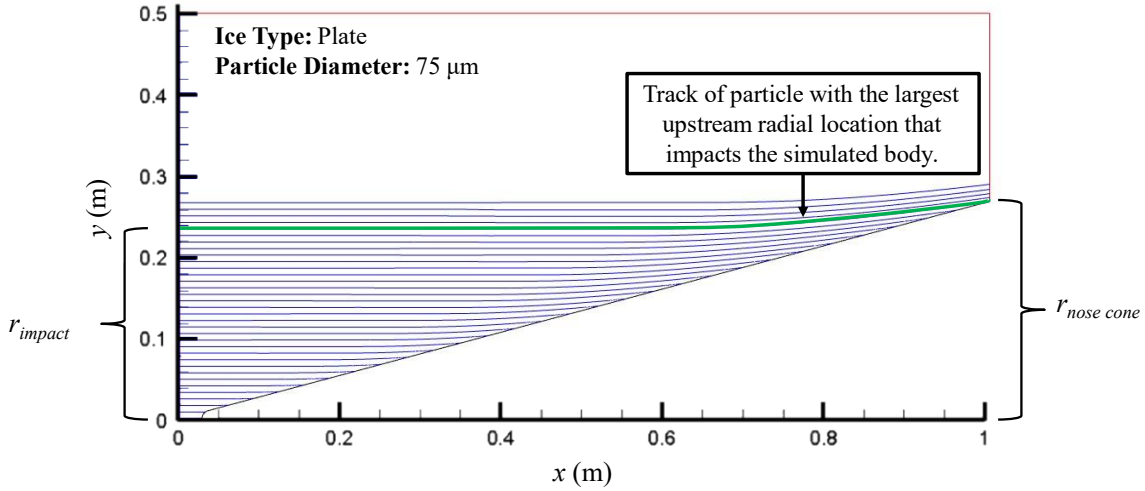

Fig. 5.10 Schematic outlining the definition of r_{impact} and r_{nose} cone using the particle tracks for plate ice particles with a diameter of 75 μm.

3.3 – Particle Impact Physics

Surface erosion is a result of the number of particles impacting the surface and the material properties defining the particle and surface material. To analyze the impact of the particles across the radial extent of the vehicle body, 10,000 particles were released at equidistant spacing along the inlet boundary condition for each different ice shape and particle bin size. The probability of particle impact was calculated by using a particle-impact fraction, which was defined by Connolly *et al.* [9] as the ratio of the number of particles that impact the nose cone to the total number of particles that are in the projected upstream cross-sectional area based on the nose cone radius ($A_{nose\ cone}$). As diagramed in Fig. 5.10, due to a fixed cross-sectional area upstream (A_{impact}), the impact fraction can be determined by the ratio of the largest upstream radial location of particles that impacted the vehicle (r_{impact}) relative to the radius of the nose cone ($r_{nose\ cone}$):

$$\eta = \frac{A_{impact}}{A_{nose\ cone}} = \frac{r_{impact}^2}{r_{nose\ cone}^2} \tag{5.15}$$

The particle impact fraction for various particles and diameters is shown in Fig. 5.10. In contrast to the ice particles, ARD analyzed by Connolly *et al.* [9] particles can be found as small as 1 μm at the same altitude and almost all the smaller particles were seen to be carried by the flow away from the vehicle body and do not make an impact. As the particle diameter increases, there were considerably more particle impacts for ARD. At the minimum particle diameter for plate and column ice, their impact fractions respectively are 0.76 and 0.92. For all other diameters of ice particles analyzed, the impact fraction is greater than 0.9.

To understand the influence of the particle impact physics on the vehicle, it is necessary to consider various erosion models. As noted previously, studies completed by Lorenz and Palmer *et al.* [6,8] have also sought to examine the mechanisms that control surface erosion due to particle impact and have done so for materials more likely to be found on a hypersonic vehicle. The studies selected are not comprehensive of all erosion models present in the field. Lorenz found that total erosion is a function of both cutting wear and impact wear. Cutting wear is the result of the particle "cutting" away at the surface material and is the driving erosion mechanism

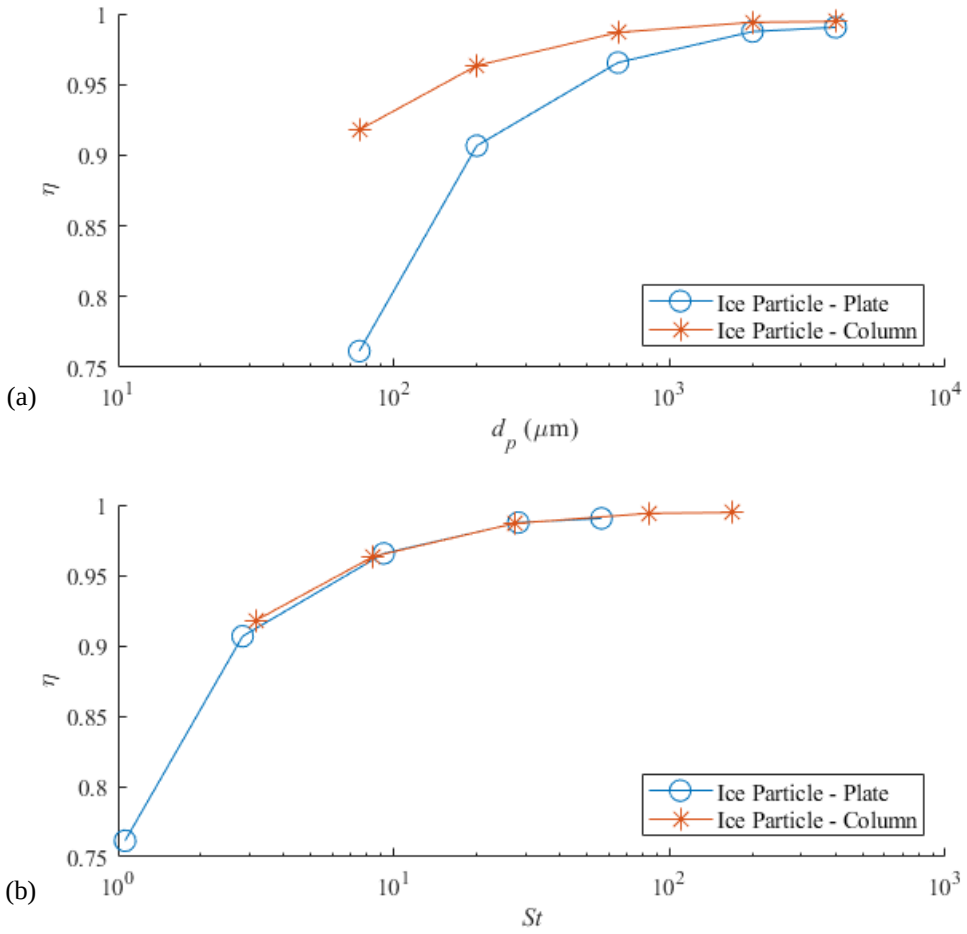

Fig. 5.11 Particle-impact fraction, with respect to a) particle diameter and b) Stokes number, on a hypersonic cone for various particles: Connolly's meteorological particles (ARD) [9], plate shaped ice particles, and column shaped ice particles.

at low incident angles. Impact wear is a result of the velocity component of the particle that is normal to the surface of the vehicle and is the driving erosion mechanism at high incident angles. Palmer *et al.* [6], in contrast, developed experimentally derived erosion models for various materials that found the total amount eroded as a function of the crater diameter and depth resultant of a particle impact. While both are different methods to model erosion, each model presented thus far, including the one defined by Cai *et al.* [2], can be rearranged into a non-dimensional equation, Γ, defined as the following:

$$\Gamma = \frac{mass\ eroded}{mass\ impacted} \tag{5.16}$$

All models were adjusted in order to make the resulting units kg/kg for mass eroded per mass impacted. The model presented by Cai *et al.* [2] is rewritten as the following:

$$\Gamma = \frac{E_m}{q} = \left[4.92\cos(90-\beta)\left(\frac{v_p}{100}\right)^{2.35} d_p^{1.26}\,\rho_p\rho_c K_c^{-1.64} H^{-1.08}\right]\cdot\frac{1}{10^6} \tag{5.17}$$

Lorenz's model, as presented in Eq. (5.2), is rewritten as the following with an adjustment to the right-hand side in order to convert the units of the cutting resistance, φ, into SI [8]:

$$\Gamma = \frac{WR_t}{m_{p,total}} = \frac{v_p^2 cos^2\beta}{2\phi} \cdot \frac{1}{1.3558 \cdot 10^3} \tag{5.18}$$

The last set of models for various materials considered (Fused Silica, AVCOAT, and Cork) were selected from those presented by Palmer *et al.* [6]. As seen in Eq. (5.3), the models predict that the total amount of erosion depth is mainly a function of crater diameter, crater depth, and number of particles impacted. To determine the amount of mass eroded, the erosion depth was assumed to be constant across the surface of the vehicle:

$$mass\ eroded = (\sum p) A_{v,surf} \rho_c \tag{5.19}$$

The number of particles impacting the surface (N_p) is equal to the mass of all the particles impacting divided by mass per particle, which is assumed to be proportional to the mass of the particles per unit time (q) and the characteristic time scale of the flow domain:

$$q = (IWC \cdot A_{v,surf} \cdot v_f \cdot \eta \cdot m\%) \tag{5.20}$$

$$N_p = \frac{q}{m_p A_{v,surf}} \cdot \frac{l_0}{u_0} \tag{5.21}$$

Where η (impact fraction) and $m\%$ (mass percentage) are functions of the ice particle shape and size, m_p is the mass of the particle, and $A_{v,surf}$ is the surface area of the vehicle forebody assuming an axisymmetric geometry. It is worth noting that while this study utilizes the characteristic time scale of the flow domain to determine N_p, the amount of time that the vehicle spends at the given flight condition, based on the vehicle's trajectory, can also be used to determine N_p. Combining Eq. (5.3), (5.19), (5.20), and (5.21) results in the following general definition of mass eroded per mass impacted for the models presented by Palmer [6]:

$$\Gamma = \frac{(\sum p) A_{v,surf} \rho_c}{q} \cdot \frac{u_0}{l_0} = \frac{D_c^2 p\, \rho_c \cos\theta}{\rho_p \left(\frac{1}{6}\pi d_p^3\right)} \tag{5.22}$$

Table 5.3 compiles information regarding the aforementioned studies and highlights key aspects: study type (experimental vs. theoretical), surface material particles are impinging on, particle material, particle shape, particle speed, particle impact angle, and particle size. Of the information presented, there is a range of materials tested to determine the amount of erosion expected for particles that are sand-like in nature. It is necessary to note that these particles do vary in material characteristics compared to ice particles (e.g., particle hardness and fracture mechanics). While further work would need to be explored to look at how ice particles differ, the studies listed help provide an overview of some of the high-level impact physics expected to occur upon particle contact with the surface of vehicle forebody.

Using the defined non-dimensionalized equation for mass eroded per mass impacted, the above defined models and equations are largely functions of velocity, impact angle, particle diameter, particle density, and surface material properties. The following equation simplifies Γ in order to focus on those parameters:

$$\Gamma = \Xi v_p^{e1} (cos^{e2}\beta) d_p^{e3} \rho_p^{e4} \tag{5.23}$$

Where the additional term, Ξ, is a compilation of the components of each model related to the material properties of the surface/target material. The values for each exponent are listed in Table

5.4. For particle velocity, the results are similar to findings discussed by Ruff *et al.* [29] where the erosion of materials tend to be a function of the velocity raised to an exponent in the 2 to 3 range. In contrast, for particle diameter and density, the simplified equations show that there is no clear association with mass eroded per mass impacted for various models as they can range from being independent of both parameters (*e3* and/or *e4* = 0) to having a small influence on the final results (*e3* and/or *e4* > 0).

Table 5.3 List of studies with key characteristics and particle parameters

Study	Study Type	Surface/Target Material	Particle Material	Particle Shape	v_p [m/s]	β [deg.]	d_p [μm]
Cai *et al.* [2]	experimental	boronized coating	quartz sand	angular	200 - 350	0 - 90	65, 226, 336
Lorenz [8]	experimental/ theoretical	cork, silicone rubber, carborazole	glass beads	spherical	1210	0 - 90	50
Lorenz [8]	experimental/ theoretical	cork, silicone rubber, carborazole	olivine sand	angular	1210	0 - 90	125
Lorenz [8]	experimental/ theoretical	cork, silicone rubber, carborazole	silica sand	angular	1210	0 - 90	210
Palmer *et al.* [6]	theoretical	fused silica	silica sand*	spherical	variable	variable	1 - 14
Palmer *et al.* [6]	theoretical	AVCOAT - uncharred	silica sand*	spherical	variable	variable	1 - 14
Palmer *et al.* [6]	theoretical	AVCOAT - charred	silica sand*	spherical	variable	variable	1 - 14
Palmer *et al.* [6]	theoretical	cork	silica sand*	spherical	variable	variable	1 - 14
Palmer *et al.* [6]	theoretical	norcoat liege	silica sand*	spherical	variable	variable	1 - 14

***Note:** Particle material from Palmer *et al.* [6] is 70% SiO_2, 15–20% Al_2O_3, and other trace compounds.

Table 5.4 Comparison of exponents for different normalized erosion models, Γ

Study	Surface/Target Material	*e1*	*e2*	*e3*	*e4*
Cai *et al.* [2]	boronized coating	2.35	1.00	1.26	1.00
Lorenz [8]	cork, silicone rubber, carborazole	2.00	2.00	0.00	0.00
Palmer *et al.* [6]	fused silica	2.00	1.00	0.40	0.17
Palmer *et al.* [6]	AVCOAT - uncharred	2.00	1.00	0.18	0.50
Palmer *et al.* [6]	AVCOAT - charred	2.00	1.00	0.00	0.50
Palmer *et al.* [6]	cork	2.00	1.00	0.00	0.00
Palmer *et al.* [6]	norcoat liege	2.00	1.00	0.15	0.86

Leveraging the impact fraction in combination with the expected IWC and defined mass fraction at the simulated altitude, it is possible to utilize the prior discussed empirical formulas to examine the amount of erosion the ice particles can cause to specific materials. Fig. 5.12 was generated using Eq. (5.1) and (5.20) with values defined by Cai *et al.* [2] based on their experimental study and subsequent empirical formula for a boronized coating. Figure 5.12 highlights both the particle shape and sizes that will cause the most theoretical erosion per unit time to the hypersonic vehicle body. In regards to particle shape, column ice is expected to be the largest contributor to surface erosion in comparison to plate ice. For particle size, both ice shapes have similar trends and show that the peak theoretical erosion per unit time is caused by particles that have a diameter of 2,000 μm. Overall, this is expected since the bin associated with this particle size and geometry contains the most mass by far (Table 5.2). However, the total overall erosion per unit time does show that there will be significant erosion of the surface on the order of tens of kilograms if a hypersonic vehicle with a boronized coating flies through meteorological ice particles.

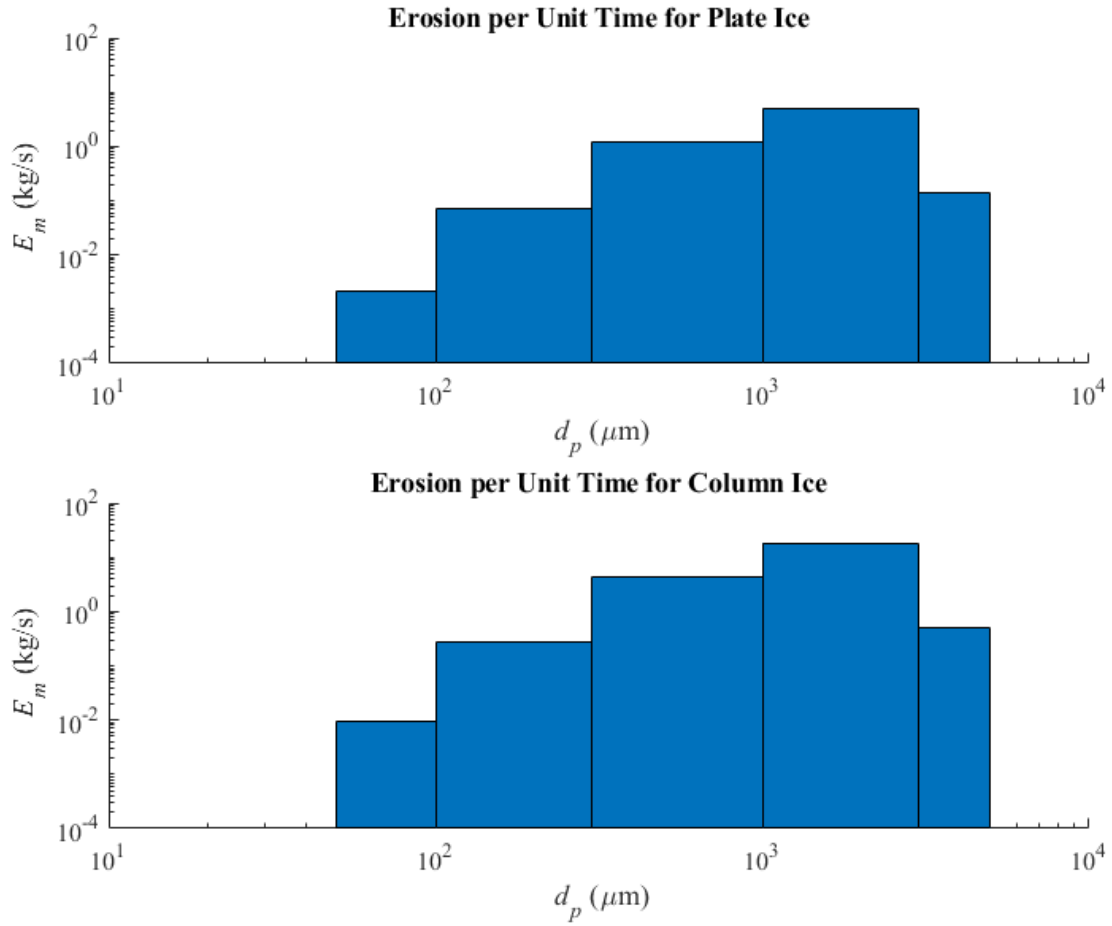

Fig. 5.12 Mass erosion per unit time for a boronized coating for each bin of particle sizes defined in Table 5.2 for a) plate ice and b) column ice.

4 – Conclusion

Impact with ice particles and other meteorological particles is necessary to consider when designing and developing hypersonic vehicles. These particles can have a damaging effect on the surface of the vehicle and can ultimately harm critical components like the engine, optical radomes, and vehicle forebody. This study analyzed a range of ice particle diameters and shapes at a flight condition of Mach 4 at an altitude of 10 km. This flight condition was chosen to remain consistent with work completed by Connolly *et al.* [9] to analyze volcanic ash/sand (ARD) particles at a point along theoretical flight trajectories where the hypersonic vehicle will likely encounter significant concentrations of particles.

The range of ice particle diameters in this study shows that even at the smallest expected diameter, the particles are largely not influenced by the change in the flow direction post-shock. Between the two particle shapes examined, plate and column, column ice impacts the vehicle body at a higher speed, is subjected to a smaller change in temperature over the trajectory and has a higher impact fraction when compared to plate ice. While both particles have a >0.70 impact fraction at 75 μm and larger diameters, the slope of the impact fraction as the particle size decreases indicates that plate ice is more sensitive to particle size than column ice. This is a result of the higher C_D for plate ice and should be taken into consideration for future studies that may analyze smaller particle sizes.

Various erosion models were reviewed and utilized to determine the relative amount of erosion due to particle shape and size. It is necessary to note that the models discussed and applied used sand-like particles for their analysis and have considered erosion as a function of material characteristics. There is a lack of studies that have defined erosion models based on particle material characteristics such as hardness and response to temperature rises in the fluid domain. As such, this study leverages the current information available in literature to analyze particle impact with the understanding that higher order studies are necessary to fully understand the complete physics and interaction of ice particles with shockwaves and varying materials.

The mass erosion model developed by Cai *et al.* [2] is highlighted with taking into account the mass distribution of various ice particles with regards to shape and size. This results in highlighting the bin of particles represented by the 2,000 μm column ice as the greatest theoretical contributor to surface material erosion. Majority of the other erosion models examined in this study highlight that the mass of material eroded per mass of particle impacted is largely independent to the particle size. However, a full analysis of material erosion with regards to its dependence on the surface material of the hypersonic body should still be considered in the future.

The combination of studies completed to understand the impact of ash, sand, and ice particles has shown that there is a high chance of impact with a hypersonic vehicle. The next step in determining the full effect of these particles on the vehicle body is pursuing a set of studies that look to derive a generic formula that captures the erosion of the vehicle body as a function of both the particle material properties and the vehicle body's surface material. Previous studies have been limited and focused on deriving empirical formulas from experimental data that used specific particles and surface materials (e.g., sand particle impact on boronized coatings, silica aggregate particles on graphite, etc.). Further work needs to be conducted both experimentally and computationally to specifically analyze ice particles at high supersonic and hypersonic velocities. Additionally, the creation of a generic erosion model that encompasses the present findings and

future studies can support the creation of a computational model to determine erosion rate of the surface of hypersonic vehicle for any particle and material.

Chapter 5 References

[1] Waxman, R., Poisl, W. H., and Guven, I., "Small Particle Erosion of Coated and Uncoated Electro-Optical Materials," *Proceedings of SPIE 10985, Window and Dome Technologies and Materials XVI*, 109850A, Soc. of Photo-Optical Instrumentation Engineers (SPIE), Bellingham, Washington, May 2019.

[2] Cai, L. X., Li, Y., Wang, S. Sen, He, Y., Li, F., and Liu, Z. K. "Investigation of the Erosion Damage Mechanism and Erosion Prediction of Boronized Coatings at Elevated Temperatures." *Materials*, Vol. 14, No. 1, 2021. https://doi.org/10.3390/ma14010123.

[3] Hong, Y. K., Park, C., and Baek, S. W. "High-Velocity Impact of Ice Particles on a Composite Material." *Journal of Composite Materials*, Vol. 43, No. 17, 2009. https://doi.org/10.1177/0021998309340059.

[4] Mehta, N. A., and Levin, D. A. "Multiscale Modeling of Damaged Surface Topology in a Hypersonic Boundary." *Journal of Chemical Physics*, Vol. 151, No. 12, 2019. https://doi.org/10.1063/1.5117834.

[5] Veysset, D., Lee, J. H., Hassani, M., Kooi, S. E., Thomas, E. L., and Nelson, K. A. "High-Velocity Micro-Projectile Impact Testing." *Applied Physics Reviews*, Vol. 8, No. 1, 2021. https://doi.org/10.1063/5.0040772

[6] Palmer, G., Ching, E., Ihme, M., Allofs, D., and Gülhan, A. "Modeling Heat-Shield Erosion Due to Dust Particle Impacts for Martian Entries." *Journal of Spacecraft and Rockets*, Vol. 57, No. 5, 2020. https://doi.org/10.2514/1.A34744.

[7] Finnie, I. "Erosion of Surfaces by Solid Particles." *Wear*, Vol. 3, No. 2, 1960. https://doi.org/10.1016/0043-1648(60)90055-7.

[8] Lorenz, G. C. "Simulation of the Erosive Effects of Multiple Particle Impacts in Hypersonic Flow." *Journal of Spacecraft and Rockets*, Vol. 7, No. 2, 1970. https://doi.org/10.2514/3.29885.

[9] Connolly, B., and Loth, E. "Simulations of Ash and Sand Impact on a Hypersonic Forebody." *AIAA Journal*, Vol. 59, No. 6, 2021. https://doi.org/10.2514/1.j059552.

[10] Peddieson, J., and Lyu, C. H. "Dusty Hypersonic Wedge Flow." *AIAA Journal*, Vol. 11, No. 1, 1973. https://doi.org/10.2514/3.6680.

[11] Probstein, R. F., and Fassio, F. "Dusty Hypersonic Flows." *AIAA Journal*, Vol. 8, No. 4, 1970. https://doi.org/10.2514/3.5755.

[12] Papadopoulos, P., Tauber, M., and Chang, I-D. "Heat Shield Erosion in a Dusty Martian

Atmosphere." *Journal of Spacecraft and Rockets*, Vol. 30, No. 2, 1993. https://doi.org/10.2514/3.11522

[13] Connolly, B. J., Loth, E., and Smith, C. F. "Shape and Drag of Irregular Angular Particles and Test Dust." *Powder Technology*, Vol. 363, 2020. https://doi.org/10.1016/j.powtec.2019.12.045.

[14] Potts, R. J. "Satellite Observations of Mt Pinatubo Ash Clouds." *Australian Meteorological Magazine*, Vol. 42, No. 2, 1993.

[15] Grindle, T. J., and Burcham, F. W. "Engine Damage to a NASA DC-8-72 Airplane From a High-Altitude Encounter With a Diffuse Volcanic Ash Cloud." 2003.

[16] Barbagallo, J. "Advisory Circular 00-6B: Aviation Weather." *Federal Aviation Administration Advisory Circular*, 2016.

[17] Ekelund, R., Eriksson, P., and Pfreundschuh, S. "Using Passive and Active Observations at Microwave and Sub-Millimetre Wavelengths to Constrain Ice Particle Models." *Atmospheric Measurement Techniques*, Vol. 13, No. 2, 2020. https://doi.org/10.5194/amt-13-501-2020.

[18] Gundlach, B., Schmidt, K. P., Kreuzig, C., Bischoff, D., Rezaei, F., Kothe, S., Blum, J., Grzesik, B., and Stoll, E. "The Tensile Strength of Ice and Dust Aggregates and Its Dependence on Particle Properties." *Monthly Notices of the Royal Astronomical Society*, Vol. 479, No. 1, 2018. https://doi.org/10.1093/MNRAS/STY1550.

[19] Jeck, R. K. "Snow and Ice Particle Sizes and Mass Concentrations at Altitudes Up to 9 Km (30,000 Ft)." Federal Aviation Administration, 1998.

[20] Spek, A. L. J., Moisseev, D. N., Russchenberg, H. W. J., Unal, C. M. H., and Chandrasekar, V. "Retrieval of Microphysical Properties of Snow Using Spectral Dual Polarization Analysis." 2005.

[21] Heymsfield, A. J., and Kajikawa, M. "Improved Approach to Calculating Terminal Velocities of Plate-Like Crystals and Graupel." *Journal of the Atmospheric Sciences*, Vol. 44, No. 7, 1987. https://doi.org/10.1175/1520-0469(1987)044<1088:AIATCT>2.0.CO;2.

[22] Mitchell, D. L. "Use of Mass- and Area-Dimensional Power Laws for Determining Precipitation Particle Terminal Velocities." *Journal of the Atmospheric Sciences*, Vol. 53, No. 12, 1996. https://doi.org/10.1175/1520-0469(1996)053<1710:UOMAAD>2.0.CO;2.

[23] "Ansys Fluent Theory Guide - Release 15.0." ANSYS Inc., No. November, 2013.

[24] Loth, E. "Drag of Non-Spherical Solid Particles of Regular and Irregular Shape." *Powder Technology*, Vol. 182, No. 3, 2008. https://doi.org/10.1016/j.powtec.2007.06.001.

[25] Um, J., McFarquhar, G. M., Hong, Y. P., Lee, S. S., Jung, C. H., Lawson, R. P., and Mo, Q. “Dimensions and Aspect Ratios of Natural Ice Crystals.” *Atmospheric Chemistry and Physics*, Vol. 15, No. 7, 2015. https://doi.org/10.5194/acp-15-3933-2015.

[26] Barone, D., Loth, E., and Snyder, P. “Influence of Particle Size on Inertial Particle Separator Efficiency.” *Powder Technology*, Vol. 318, 2017. https://doi.org/10.1016/j.powtec.2017.04.044.

[27] Noel, V., Chepfer, H., Haeffelin, M., and Morille, Y. “Classification of Ice Crystal Shapes in Midlatitude Ice Clouds from Three Years of Lidar Observations over the SIRTA Observatory.” *Journal of the Atmospheric Sciences*, Vol. 63, No. 11, 2006. https://doi.org/10.1175/JAS3767.1.

[28] Bailey, M. P., and Hallett, J. “A Comprehensive Habit Diagram for Atmospheric Ice Crystals: Confirmation from the Laboratory, AIRS II, and Other Field Studies.” *Journal of the Atmospheric Sciences*, Vol. 66, No. 9, 2009. https://doi.org/10.1175/2009JAS2883.1.

[29] Ruff, A., and Wiederhorn, S. “Erosion by Solid Particle Impact.” *Treatise On Materials Science and Technology*, Vol. 16, 1979, pp. 69–126.

Chapter 6

Conclusions

The first objective of this research was to employ computational models to complement experimental research that focused on understanding an 8.9% scaled CRM65 wing with and without an ice shape on the leading edge at moderate angles of attack. This research sought to complete this objective through understanding three components:

1) Evaluate RANS k-ω SST to capture both the flow physics for a swept wing without an ice shape and the generated wake downstream

2) Assess the ability of the RANS k-ω SST to predict the three-dimensional complex flow over a swept wing with and without an ice shape via steady state simulations

3) Compare the ability of RANS against solutions derived from Hybrid RANS-LES methods (i.e., DES and IDDES)

Results from the first set of studies shows that the RANS k-ω SST model was able to replicate the structure of the wake as compared to the experimental data and produce wake derived aerodynamic coefficients that were within 6% of the experimentally derived coefficients of lift and drag. However, while proper grid refinement allows the simulation to accurately capture the wake downstream of the wing, capturing this phenomenon is shown to not be crucial in accurately predicting the integrated aerodynamic coefficients derived from the surface pressures of the wing. This allows for reduction in meshing complexity for the second and third set of studies to complete the first objective of this research.

The second and third set of studies highlighted that the flow over a swept-wing is highly unsteady and three-dimensional (as can be seen in the Q-criterion visualizations). As the angle of attack increases, the size of the turbulent structures present in the flow domain increases as well as the flow progressing becomes more separated above the swept-wing. Leveraging the experimental data collected, the mini-tufts, oil flow visualization, and computationally derived wall share stress show that there is a large component of spanwise flow with increasing angle of attack. However, it was clear that RANS outperformed both DES and IDDES in the prediction of the flow physics over the wing. The Hybrid RANS-LES methods predicted early onset of flow reattachment, especially towards the outboard sections of the wing. This mis-prediction in separation was also highlighted in both the pressure distributions and the integrated aerodynamic coefficients. This issue can linked to the presence of a complex spanwise component of flow over the upper surface that is affecting the ability of the turbulence models to predict the fluid dynamics in the transition zone, or “grey area”. In this region, the model switches between URANS and LES.

Further work should be completed to understand the turbulent mixing in this transition area, explore improvements to DES and IDDES to capture three-dimensional flow separation, as well as continue investigating the impact of ice shape resolution (e.g., smooth vs. high fidelity 3D geometry) on the flow physics.

The second objective of this research was to focus on hypersonic vehicle interaction with ice particles and understand particle trajectories, changes in characteristic particles properties, and subsequent impact and erosion for a range of ice particle diameters and shapes. Results highlighted that the range of ice particle sizes analyzed were largely not influenced by the change in flow direction post-shock and resulted in St >> 1. Over the course of their trajectories, the particles did not have a large change in velocity prior to impact and did not experience a large enough delta in temperature prior to impact in which phase change would need to be considered. Overall, the impact fraction for all particle sizes and shapes were above 0.70, thus highlighting it is reasonable to expect ice particles to consistently impact a hypersonic vehicle flying through a cloud at an altitude of 10 km. Utilizing various erosion models for different surface materials, results show that at this speed, erosion is a function of both particle diameter and surface materials. Further work is recommended to develop a generic erosion model that can encompass the variety of materials that will be used for a hypersonic body in order to continue analyzing erosion rates of the surface across any particle and material.